


2015

True linearized intensity modulation for photonic analog to digital conversion using an injection-locked mode-locked laser

Edris Sarailou
University of Central Florida

 Part of the [Electromagnetics and Photonics Commons](#), and the [Optics Commons](#)
Find similar works at: <https://stars.library.ucf.edu/etd>
University of Central Florida Libraries <http://library.ucf.edu>

This Doctoral Dissertation (Open Access) is brought to you for free and open access by STARS. It has been accepted for inclusion in Electronic Theses and Dissertations, 2004-2019 by an authorized administrator of STARS. For more information, please contact STARS@ucf.edu.

STARS Citation

Sarailou, Edris, "True linearized intensity modulation for photonic analog to digital conversion using an injection-locked mode-locked laser" (2015). *Electronic Theses and Dissertations, 2004-2019*. 1175.
<https://stars.library.ucf.edu/etd/1175>

**TRUE LINEARIZED INTENSITY MODULATION FOR PHOTONIC
ANALOG TO DIGITAL CONVERSION USING AN INJECTION-LOCKED
MODE-LOCKED LASER**

by

EDRIS SARAILOU

B.S. Semnan University, Iran, 2004

M.S. Shiraz University, Iran, 2007

A dissertation submitted in partial fulfillment of the requirements
for the degree of Doctor of Philosophy
in the College of Optics and Photonics, CREOL
at the University of Central Florida
Orlando, Florida

Spring Term
2015

Major Professor: Peter J. Delfyett

© 2015 Edris Sarailou

ABSTRACT

A true linearized interferometric intensity modulator for pulsed light has been proposed and experimentally presented in this thesis. This has been achieved by introducing a mode-locked laser into one of the arms of a Mach-Zehnder interferometer and injection-locking it to the input light (which is pulsed and periodic). By modulating the injection-locked laser, and combining its output light with the light from the other arm of interferometer in quadrature, one can achieve true linearized intensity modulator. This linearity comes from the arcsine phase response of the injection-locked mode-locked laser (as suggested by steady-state solution of Adler's equation) when it is being modulated.

Mode-locked lasers are fabricated using a novel AlGaInAs-InP material system. By using the BCB for planarization and minimizing the metal pad size and directly modulating the laser, we have achieved very effective fundamental hybrid mode-locking at the repetition rate of ~ 23 GHz. This laser also provided the short pulses of 860 fs and 280 fs timing jitter integrated from 1 Hz-100 MHz.

The linearized intensity modulator has been built by using two identical two-section mode-locked lasers with the same length, one as the slave laser in one of the arms of the Mach-Zehnder interferometer injection-locked to the other one as the master which is the input light to the modulator. A low V_π of 8.5 mV is achieved from this modulator. Also the current of the gain section or the voltage of the saturable absorber section of the slave laser has been used to apply the modulation signal. A spur free dynamic range of $70 \text{ dB.Hz}^{2/3}$ is achieved when modulating the modulator through the saturable absorber. Modulating the saturable absorber provides a reduced

third-order intermodulation tone with respect to modulating the gain. This is simply because of the unwanted amplitude modulation created when modulating the gain section current.

Finally an improved design is proposed and demonstrated to improve the modulator performance. This is achieved by introducing a third section to the laser. Using the impurity free vacancy disordering technique the photoluminescence peak of this section is blue-shifted selectively and therefore there would not be any absorption in that passive section. By applying the modulation signal to this passive section rather than applying it to the gain section or saturable absorber section, the amplitude and phase modulation could be decoupled. The experimental results have presented here and an almost six-fold reduction in V_π and 5 dB improvement in spur free dynamic range have been achieved. The proposed and demonstrated configuration as an analog optical link has the potential to increase the performance and resolution of photonic analog-to-digital converters.

For my wife, Somayeh

ACKNOWLEDGMENTS

I am very grateful to my advisor, Dr. Peter Delfyett, for original ideas, his positive support and thoughtful guidance during my PhD program. I owe him many thanks for believing in me and keeping me motivated all the time.

I would like to thank my dissertation committee, Prof. Sasan Fathpour, Prof. Patrick LiKamWa and Prof. Donald C. Malocha for their insightful comments and questions.

I want to specifically thank Dr. Fathpour for his great advice and thoughtful discussion during my thesis work. I also want to thank Dr. LiKamWa who I learned a great deal over the years. Without his continuous help and timeless effort on our cleanroom facility none of this work would have been possible.

I am thankful to the CREOL staff in particular Rachel Agerton-Franzetta, Amy Perry, Gail Drabczuk, for their help in navigating the administrative requirement of the University and having great conversations through these years. I also want to thank James D. Ross for keeping the CREOL Nanophotonics fabrication facility up and running. Also my appreciation to my fellow group members over the years, including Dr. Nishant Bhatambrekar, Dr. Ibrahim Ozdur, Dr. Jimyung Kim, Dr. Dimitrios Mandridis, Dr. Sharad Bhooplapur, Dr. Marcus Bagnell, Dr. Charles Williams, Dr. Mohammad Umar Piracha, Dr. Dat Nguyen, Dr. Abhijeet Ardey, Dr. Nazanin Hoghooghi, Dr. Josue Davilla-Rodriguez, Anthony Klee, Kristina Bagnell, Roman Grigorev, Mina Bayat, and Abdullah Zaman for their help and support.

I am grateful to have such a wonderful friends in Orlando (Seyfollah, Hooman, and Viyan) who were as a family to me here. I also will always appreciate my uncle-in-law Ghasem Khavanin

and my aunt-in-law Soudabeh Ketabchi who provided help in one way or another during all of these years.

To my mother and my grandmother, Leila and Halimeh-Khatoon, who supported and encouraged me from the time I opened my eyes, I am forever thankful. Without their endless love and sacrifices none of this would have been possible.

This work is dedicated to my sweetheart, Somayeh, who was with me through thick and thin. I would like to thank her for her love, constant support and for all the late nights. Thank you for being my best friend. I owe you everything.

TABLE OF CONTENTS

LIST OF FIGURES	x
LIST OF TABLES	xxi
LIST OF ACRONYMS	xxiii
1. INTRODUCTION	1
1.1. Photonic analog to digital conversion.....	1
1.2. Photonic sampled analog to digital conversion	2
1.3. External intensity modulation	4
1.4. Linearized Modulators	12
1.5. Injection-locking of lasers.....	13
1.6. Linearized interferometric intensity modulator for CW light using an injection-locked VCSEL.....	16
1.7. This Thesis	23
2. ALGAINAS MULTIPLE QUANTUM WELL MODE-LOCKED LASER FABRICATION	26
2.1. AlGaInAs multiple quantum well wafer.....	26
2.2. Waveguide analysis for single mode operation	28
2.3. Mask design	32
2.4. Fabrication procedure	33
3. DIRECT RF MODULATION OF ALGAINAS MODE-LOCKED LASER.....	50
3.1. Introduction.....	50
3.2. Device structure and fabrication	52

3.3. Experimental results.....	54
3.4. Noise performance comparison	61
3.5. Conclusion	64
4. TRUE LINEARIZED INTENSITY MODULATOR FOR PULSED LIGHT	65
4.1. Introduction.....	65
4.2. Injection-locking of a passively MLL (slave) by a hybridly MLL (master).....	71
4.3. Experimental setup of the linearized intensity modulator for pulsed light.....	76
4.4. Two-tone intermodulation experiment	80
4.5. Discussion and conclusion.....	84
5. HIGHLY LINEAR INTENSITY MODULATOR FOR PULSED LIGHT USING THREE- SECTION MLLS	86
5.1. Introduction.....	86
5.2. Three-section MLL principle of operation	87
5.3. Impurity free vacancy disordering.....	89
5.4. Mask design and fabrication	106
5.5. Device Characteristics	113
5.6. Experimental setup of the ultra linear intensity modulator.....	118
5.7. Experimental Results	120
5.8. Conclusion	125
APPENDIX A: THERMAL ANNEALING PROFILES	126
REFERENCES	129

LIST OF FIGURES

Figure 1-1: Typical analog optical link [2]	2
Figure 1-2: Photonic sampled and electronically quantized ADC [2]	3
Figure 1-3: Integrated DFB laser with Electro-absorption modulator	5
Figure 1-4: An electro-optic intensity modulator. It uses the induced retardation between the two orthogonal polarizations of the light to control the light transmission through the output polarizer.	6
Figure 1-5: Modulated output light versus input modulating voltage for an electro-optic modulator	8
Figure 1-6: Lithium-Niobate Mach-Zehnder Intensity modulator schematic	9
Figure 1-7: Fundamental and third-order distortion photo-detected powers versus input RF power. SFDR is calculated by extrapolating the two fitted linear curves to the noise floor.	11
Figure 1-8: Injection locking of lasers	14
Figure 1-9: Response of the slave laser to the injection seed when it is tuned to inside or outside of the locking range [30]	16
Figure 1-10: Schematic diagram of the true linear interferometric intensity modulator [31]	17
Figure 1-11: Numerical results of the performance of the typical LiNbO_3 electro-optic modulator (red) and the true linear interferometric modulator (blue), a) SFDR versus depth of modulation, b) SFDR versus bias point of the modulator for the 10% depth of modulation [32] 18	

Figure 1-12: Schematic diagram of the true linear interferometric intensity modulator using and injection-locked VCSEL as a resonant cavity. VCSEL: Vertical cavity surface emitting laser, TEC: Thermo-electric cooler, VOA: Variable optical attenuator, PS: Phase shifter, PC: Polarization controller, Iso: Isolator, CIR: Circulator, RFSA: Radio frequency spectrum analyzer, OSA: Optical spectrum analyzer [34].....	20
Figure 1-13: Static phase shift of the injection-locked VCSEL and the arcsine fitted curve [34].....	21
Figure 1-14: The frequency response of the true linear intensity modulator [34].....	22
Figure 1-15: SFDR measurement, a) shows the power spectrum of the RF photo-detected signal consists of two equal power tones at 300 MHz and 400 MHz, b) shows the third order distortion at 500 MHz at the resolution bandwidth of 1 Hz [34].....	23
Figure 2-1. Photoluminescence spectrum of the as grown wafer at the room temperature.	28
Figure 2-2. InP wet etching profiles (a) Vertical mesa with the vertical walls (b) Mesa with the walls at an angle of ~ 45 degrees and (c) Reverse mesa with the walls at angle of ~ -45 degrees. (d) Real image of the fabricated alignment marks on quantum well wafer (top view). The sidewalls of the vertical features could be seen easily (dark area) as a proof of mesa profile. However the horizontal features sidewalls are not observable from the top view suggesting that they are either vertical mesa or reverse mesa.	30
Figure 2-3. Four possible simulated transverse modes from a mesa waveguide with the width of $3.6\ \mu\text{m}$ and the height of $1.85\ \mu\text{m}$	31

Figure 2-4. Two possible transverse mode obtained from simulating a vertical mesa waveguide with 2.5 μm width and 1.85 μm height. The second mode is very unlikely to exist since it doesn't see the carrier injection outside the waveguide walls.....	32
Figure 2-5. Image of the simple Fabry-Perot laser design from L-Edit software showing waveguide and alignment marks in blue and metal pads, alignment marks and cleaving marks in green.....	33
Figure 2-6. Sample containing two waveguides which they are formed using hydrochloric and lactic acid mixture. The waveguide are 1.6 μm deep and 2.5 μm wide. The micron size features next to the waveguides are produced because of the microbubbling.....	41
Figure 2-7. (a) Top view image from the fabricated vertical mesa waveguides, (b) the zoomed-in version of the fabricated waveguide 2.5 μm waveguide. Different color of the images coming from the different filters used when working with the microscope and does not show any information.....	43
Figure 2-8. Top view image of the fabricated 2 mm Fabry-Perot laser device after p-contact annealing	47
Figure 2-9. Scanning electron microscopy (SEM) image from a cleaved facet of the laser	48
Figure 3-1. (a) Sub-harmonic hybrid mode-locking scheme, (b) fundamental hybrid mode-locking (FHML) using semi-insulating substrate and (c) optical synchronous mode-locking [55]	51

Figure 3-2. Image of the two-section mode-locked laser design from L-Edit software showing waveguides and alignment marks in blue and metal pads, alignment marks and cleaving marks in green.....	52
Figure 3-3. Top view image of the fabricated 2 mm two-section mode-locked laser	53
Figure 3-4. Device schematic showing the waveguide structure and contact layout.	53
Figure 3-5. Contacts layout schematic and electrical connections of the hybridly mode-locked two-section laser.....	55
Figure 3-6. (a) Current vs voltage characteristics of the two-section MLL, and (b) output power-current characterization of the two-section MLL at 20°C for different reverse bias voltages	56
Figure 3-7. Far field mode pattern of the mode-locked laser measured using DataRay Inc. beam profilometer	56
Figure 3-8. Experimental setup used for hybrid mode-locking and diagnostics. Iso: isolator; SOA: semiconductor optical amplifier; PD: photodetector; PC: polarization controller; RFSA: radio frequency spectrum analyzer; OSA: optical spectrum analyzer; L: aspheric lens; FC: fiber coupler.....	57
Figure 3-9. (a) Optical spectrum of the mode-locked laser for shortest pulse at $I_{\text{gain}} = 123$ mA and $V_{\text{abs}} = -3.9$ V, (b) the corresponding RF spectrum.....	58
Figure 3-10. Autocorrelation trace of the isolated pulse under passive mode-locking	59
Figure 3-11. Double side band noise spectrum for passive, FHML at different RF power and SHML ($n = 2$). Inset shows the sampling scope trace for the FHML at RF power of 15 dBm.	60

Figure 3-12. Residual phase noise power spectral density of the FHML laser (black) under $I_{\text{gain}} = 80 \text{ mA}$ and $V_{\text{abs}} = -3.1 \text{ V}$ and the RF power of 15 dBm and noise floor of the measurement (Grey)..... 61

Figure 3-13. Single side band noise measured by RFSA for the device running under passive ML (green), SHML (blue) and FHML (red). Residual phase for the FHML (black) is also shown for reference (measured using the carrier noise test set) 63

Figure 4-1. (a) Schematic showing the slave laser resonances (black), the corresponding phase response (red), injected comb lines from the MLL (blue) and the instantaneous imparted phase on each of the injected comb lines (green), (b) Schematic of the linear interferometric intensity modulator for pulsed light. f_{master} and f_{slave} denote the mode spacing of the master and slave laser, respectively. 67

Figure 4-2. (a) Optical spectra of the passively MLL (black) and FPL as the resonant cavity before (red) and after (blue) injection-locking. Both the lasers are biased with different dc currents to match the frequency spacing between the modes which results in different spectrum widths. The injection-locked FPL spectrum is much narrower than the spectrum of the master MLL since the well-spaced modes of the MLL match at one end of the spectrum with the modes of the FPL as shown in (b) and start to walk off from each other on moving to the other side of the spectrum (c). 69

Figure 4-3. (a) RF spectrum of the hybridly MLL running at temperature of 17 °C, biased with 145 mA and $V_{\text{SA}} = -2.8\text{V}$, (b) RF spectra of the FPL running at temperature of 23 °C and biased with 58 mA before (red) and after (blue) injection-locking and (c) autocorrelation trace of an isolated pulse from the FPL after injection-locking..... 70

Figure 4-4. Typical output power-current (blue) and voltage-current (black) characteristics of the MLL operating at 20 °C. No voltage is applied to the SA. The device characteristics are: $I_{\text{threshold}}=51$ mA, $R=3.7$ Ω and slope efficiency of 0.077 W/A. Inset shows the top view of the actual fabricated MLL. 73

Figure 4-5. (a) Optical spectrum of the master laser (black) with $I_{\text{gain}}=65$ mA, $V_{\text{SA}}=-1.8$ V, $T=20$ °C and 6 dBm of RF power at 22.998 GHz (b) and (c) optical spectra of the slave laser before (red) and after (blue) injection-locking with $I_{\text{gain}}=65$ mA, $V_{\text{SA}}=-1.9$ V, $T=19.100$ °C and injection ratio of -27.8 dB. (d) Normalized RF spectra of the master laser and slave laser before and after injection-locking. (e) Autocorrelation trace of the master laser (slave laser trace is not shown since it is same as that of the master laser with similar pulse width)..... 75

Figure 4-6. Experimental setup. ISO: Isolator; BS: Beam splitter; $\lambda/2$: Half-wave plate; NDF: Neutral density filter; BT: Bias-Tee; PM: Power meter; SOA: Semiconductor optical amplifier; PD: Photo-detector; RFA: Radio frequency amplifier; OSA: Optical spectrum analyzer; RFSA: Radio frequency spectrum analyzer..... 77

Figure 4-7. Normalized change of the output power of the MZI (static phase change) as a function of DC current deviation of the slave laser. Master laser is running with $I_{\text{gain}}=65$ mA, $V_{\text{SA}}=-1.8$ V, $T=20$ °C and 6 dBm of RF power at 22.998 GHz. Slave laser is running with $I_{\text{gain}}=65$ mA, $V_{\text{SA}}=-1.9$ V and $T=19.100$ °C. Here the power injection ratio was -27.8 dB, (b) Static phase response as a function of DC current deviation for different power injection ratios. The locking bandwidth increases as the injection ratio increases, however by further increasing it, the relaxation oscillations dominate and the injection-locking becomes unstable (-16 dB). 78

Figure 4-8. High resolution optical spectra of the slave laser for different bias currents. The slave remains locked for the bias currents between 64 mA to 66 mA and unlocks for currents outside of the locking range. The 1 μ W injection signal (-27.8 dB of injection ratio when slave is biased at 65 mA) from the master laser is coupled into the slave laser from the gain section facet. Master laser bias current is kept constant at 65 mA. The injection seed from the master laser is at 1556.3688 nm and shown with the vertical solid black line. 79

Figure 4-9. (a) Photo-detected RF power spectrum of fundamental frequencies for the input RF power of -16 dBm when modulating the gain and -24 dBm when modulating the SA (the input powers are adjusted to achieve the same fundamental powers for comparison), (b) detected RF power spectra of the third-order intermodulation tones at 200 MHz, (c) detected RF power spectra of the third-order intermodulation tones at 500 MHz. Intermodulation tone shown in black when modulating the gain section and shown in red when modulating the SA section..... 82

Figure 4-10. Fundamental and third-order intermodulation powers as a function of the input RF power to the modulator. 83

Figure 5-1. Schematic of the proposed three-section device including: gain section, saturable absorber section and the new passive (phase) section. The modulation signal can be now applied through the passive section. 87

Figure 5-2. Visual representation of the frequency shift of the MLL when it is modulated through its passive section. Black and red shows the optical modes and their absolute location when the passive section is unbiased and biased, respectively..... 89

Figure 5-3. Schematic diagram of the energy levels and energy bandgap for intermixed and non-intermixed regions. 91

Figure 5-4. Measured PL shifts as a function of anneal temperature for InGaAsP with 200 nm sputtered (●) and PECVD (○) SiO₂ caps and AlInGaAs capped with 200 nm sputtered SiO₂ (◆) [87]..... 93

Figure 5-5. Compositions analysis of the AlGaInAs multiple quantum wells and barriers measured by SIMS for (a) In and (b) Ga atoms in the intermixed sample and for (c) In and (d) Ga atoms in the non-intermixed sample. Samples were annealed at 720 °C for 2 min and only the intermixed one was with a Si₃N₄ dielectric film capping layer. The data are compared to a reference (no annealing) sample [90]. 94

Figure 5-6. Optical spectra of 500-μm-long edge emitter lasers from the area that intermixing is promoted and inhibited [89] 96

Figure 5-7. (a) Profile analysis of Zn concentration measured by SIMS in intermixed AlGaInAs multiple quantum wells and barriers as well as in top AlGaInAs SCH guiding layer. The data are compared to a reference (no annealing) sample [90]. 96

Figure 5-8. Experimental setup for photoluminescence measurements at room temperature. 97

Figure 5-9. Schematic of dielectrics deposited selectively on quantum well sample to be able to define the regions that intermixing is needed to be promoted (SiN_x capped) and inhibited (SiO₂ capped). 98

Figure 5-10. The cracks occurred on the sample upon annealing because of the different thermal expansion between the dielectrics. The SiO₂ layers is deposited first and then half of the sample is covered and the uncovered SiO₂ is etched away. Finally the whole sample is covered with SiN_x. 99

Figure 5-11. PECVD deposited SiN _x stress control by the He dilution method. Films are deposited at the temperature of 250 °C with different RF powers [93].	100
Figure 5-12. Photoluminescence spectra of different samples capped with 70 nm SiN _x layers deposited with different recipes annealed at 800 °C for 2 min.	104
Figure 5-13. Photoluminescence blue shift of the sample capped with 70 nm SiN _x and capped with 190 nm of SiO ₂ for different annealing temperature (annealing time was kept 2 min for all of the samples).	105
Figure 5-14. Variation of measured photoluminescence blue shift versus annealing time for SiO ₂ and SiN _x dielectric capping layers (Annealing temperature remained unchanged at 800 °C).	106
Figure 5-15. Image of the three-section mode-locked laser design from L-Edit software showing waveguides and alignment marks in blue and metal pads, alignment marks and cleaving marks in green. The red region (passive section) shows the area that needed to be intermixed.	107
Figure 5-16. Measured photoluminescence spectra of the area capped with SiN _x (passive section) and the area capped with SiO ₂ (gain and SA sections) annealed at 800 °C for 30 seconds.	109
Figure 5-17. Top view image of the fabricated 1.9 mm three-section mode-locked laser	111
Figure 5-18. Typical current vs output power characteristics of the two 360 μm-long Fabry-Perot lasers, (a) device is cleaved from the area that intermixing inhibited and (b) is cleaved from the area that intermixing promoted.	112

Figure 5-19. Optical spectra of the two different 360 μm -long Fabry-Perot lasers, (a) device is cleaved from the area that intermixing inhibited and (b) is cleaved from the area that intermixing promoted. (Both the laser are biased with 80 mA of current and operating at 20 °C)..... 113

Figure 5-20. Typical voltage-current (left) and output power-current (right) characteristics of the MLL operating at 20 °C. No voltage is applied to the SA or passive section. The device characteristics are: $I_{\text{threshold}}=44$ mA, $R=3.3$ Ω and slope efficiency of 0.06 W/A. 114

Figure 5-21. Optical spectrum of the three-section mode-locked laser with at $I_{\text{gain}} = 70$ mA, $V_{\text{abs}} = -1.5$ V, and unbiased passive section, (b) autocorrelation trace of an isolated pulse with deconvolved width of 3.2 ps (2.86 times transform-limited), (c) the corresponding RF spectrum, and (d) full span RF spectrum..... 115

Figure 5-22. High resolution optical spectrum of the three optical modes. Black is when the passive section is unbiased and red is when the passive section is biased with 5.9 mA. 117

Figure 5-23. Output power change of the mode-locked laser as a function of passive section bias current..... 118

Figure 5-24. Experimental setup. ISO: Isolator; BS: Beam splitter; $\lambda/2$: Half-wave plate; NDF: Neutral density filter; BT: Bias-Tee; PM: Power meter; SOA: Semiconductor optical amplifier; PD: Photo-detector; RFA: Radio frequency amplifier; OSA: Optical spectrum analyzer; RFSA: Radio frequency spectrum analyzer..... 119

Figure 5-25. Optical spectrum of the two-section hybridly mode-locked master laser (black) with $I_{\text{gain}}=75$ mA, $V_{\text{SA}}=-1.4$ V, $T=17.35$ °C and 6 dBm of RF power at 22.712 GHz and optical spectra of the three-section passively mode-locked slave laser before (blue) and after (red) injection-locking with $I_{\text{gain}}=55$ mA, $V_{\text{SA}}=-1.2$ V, $T=20$ °C..... 121

Figure 5-26. (a) Normalized radio frequency spectrum of the master laser (black) and also the slave laser before (red) and after injection-locking and (b) their corresponding autocorrelation traces. It is clear that the slave laser follows the master after injection-locking. 122

Figure 5-27. (a) Photo-detected RF power spectrum of fundamental frequencies (1 GHz and 1.1 GHz) (the input powers are adjusted to achieve the same fundamental powers), (b) detected RF power spectra of the third-order intermodulation tones at 900 MHz, (c) detected RF power spectra of the third-order intermodulation tones at 1200 MHz..... 123

Figure 5-28. Fundamental and third-order intermodulation powers as a function of the input RF power to the modulator. 124

LIST OF TABLES

Table 1. AlGaInAs multiple quantum well wafer layer structure.....	27
Table 2. Deposition parameters of the recipe “SIN-DIFF” for Si ₃ N ₄ deposition. The silane gas (SiH ₄) used is 2% silane diluted in N ₂	36
Table 3. Reactive Ion Etching (RIE) parameters for photoresist and Si ₃ N ₄ etching. Etching has been done in the room temperature.	38
Table 4. Wet etching rate of the H ₂ SO ₄ and H ₃ PO ₄ acids solution for the InGaAs and InGaAsP layers [44, 45].....	39
Table 5. InP etching rate of different acid solutions [41, 46, 47]	40
Table 6. The temperature profile used for BCB hard-curing.....	44
Table 7. Reactive Ion Etching (RIE) parameters for BCB etching.....	45
Table 8. Integrated single sideband noise from 4 MHz to 100 MHz of the device running under different mode-locking scheme	63
Table 9. Deposition parameters of the recipes used for SiN _x deposition. The flow unit for all of the gases is standard cubic centimeters per minute (sccm). The samples are annealed at the annealing temperature of 800 °C for 2 min. For the sake of consistency, SiN _x and SiO ₂ dielectric layer thicknesses are kept the same (70nm±5nm and 185nm±10nm for SiN _x and SiO ₂ , respectively).....	102
Table 10. Deposition parameters of the recipe “depsio2” for SiO ₂ deposition. The silane gas (SiH ₄) used with this PECVD machine is 2% silane diluted in N ₂	103

Table 11. Reactive Ion Etching (RIE) parameters for SiO ₂ etching. Etching has been done in the room temperature.	111
---	-----

Table 12. Thermal annealing recipe used for annealing contact at the temperature of 430 °C for 30 seconds	127
---	-----

Table 13. Thermal annealing recipe used for intermixing at the temperature of 800 °C for 30 seconds	128
---	-----

LIST OF ACRONYMS

ADC	Analog to Digital Converter
ASE	Amplified Spontaneous Emission
BCB	Benzocyclobutene
BPM	Beam Propagation Method
BS	Beam Splitter
CIR	Circulator
DFB	Distributed Feedback Laser
DUT	Device under Test
CNR	Carrier to Noise Ratio
DI	Deionized
EAM	Electro Absorption Modulator
ENOB	Effective Number of Bits
FCC	Face Centered Cubic
FC	Fiber Coupler
FPL	Fabry-Perot Laser
FSR	Free spectral Range
FHML	Fundamental Hybrid Mode-Locking
GS	Ground-Signal
HSQ	Hydrogen Silsesquioxane
ISO	Isolator

IFVD	Impurity Free Vacancy Disordering
MQW	Multiple Quantum Well
MLL	Mode-Locked Laser
MZI	Mach-Zehnder Interferometer
MOVPE	Metal Organic Vapor Phase Epitaxy
NDF	Neutral Density Filter
OSA	Optical Spectrum Analyzer
PD	Photodetector
PL	Photoluminescence
PECVD	Plasma Enhanced Chemical Vapor Deposition
PC	Polarization Controller
PID	Proportional-Integral-Derivative
QCSE	Quantum Confined Stark Effect
QW	Quantum Well
QWI	Quantum Well Intermixing
RF	Radio Frequency
RIN	Relative Intensity Noise
RTA	Rapid Thermal Annealing
RIE	Reactive Ion Etching
SFDR	Spur Free Dynamic Range
SEM	Scanning Electron Microscopy
SOA	Semiconductor Optical Amplifier
SHML	Sub-harmonic Hybrid Mode-Locking

SCH	Separate Confinement Heterostructure
SA	Saturable Absorber
TEC	Thermo-Electric Cooler
VCSEL	Vertical Cavity Surface Emitting Laser
VOA	Variable Optical Attenuator
WDM	Wavelength Division Multiplexing

1. INTRODUCTION

1.1. Photonic analog to digital conversion

Photonic ADCs are desirable for high speed and high performance sampling and digitization of microwave signals. They could potentially eliminate the required mixing and filtering stages of the radio frequency (RF) carriers (down-conversion) used in low speed conventional electrical ADCs and could provide a smaller size and weight, lower cost, wider instantaneous bandwidth, and increased reliability [1, 2].

Most of the suggested photonic ADCs configuration contain an analog optical link between their RF input and the digital output [3, 4]. An analog optical link consists of an optical source, a modulator, and a photodiode as shown in Figure 1-1. Usually a semiconductor laser or a fiber mode-locked laser is used as the source and an external LiNbO_3 Mach-Zehnder interferometer is used to impress the RF input signal on the optical signal. In some configuration the laser source itself is modulated with the RF signal directly. In more general analog optical links, there is a long optical fiber between the photodiode and the electronics part. The performance of the analog optical link is limited by noise and nonlinearities. The carrier-to-noise ratio, CNR, of analog optical link is expressed as [5]

$$CNR = \frac{(mRP)^2/2}{(\sigma_s^2 + \sigma_{th}^2 + \sigma_{RIN}^2)} \quad (1-1)$$

where σ_s , σ_{th} , and σ_{RIN} are standard deviations of the photodiode noise current associated with shot, thermal and relative intensity noise (RIN), m is the modulation depth of the electro-optic modulator, R is the responsivity of the photodiode and P is the average optical power on the photodiode.

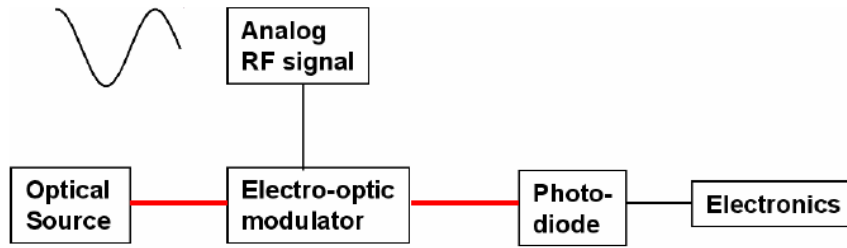


Figure 1-1: Typical analog optical link [2]

1.2. Photonic sampled analog to digital conversion

The use of a mode-locked laser for photonic sampling of RF signals first introduced by Taylor et al. [6]. The short pulse width and low pulse-to-pulse jitter of a mode-locked laser make them a very attractive tool for photonic sampling of RF signals. A photonic sampled ADC consists of a stable-mode locked laser, an electro-optic modulator (generally Mach-Zehnder LiNbO₃ modulator), and a high speed photodiode to deliver the electrical signal for the electronic ADC (Figure 1-2). This photonic sampled ADC incorporates an analog optical link to be able to sample the RF signal to a sampling time equal to the pulse width of the mode-locked laser and sampling

jitter equal to pulse to pulse jitter of the mode-locked laser. However the performance of this photonic sampled ADC is characterized by its SFDR, SNR, modulator bandwidth, and photodiode saturation current bandwidth.

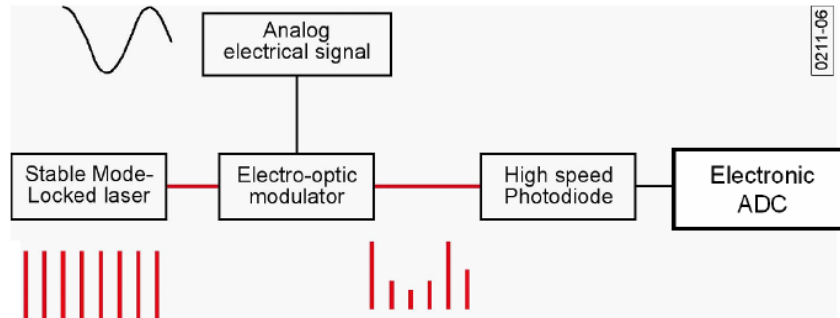


Figure 1-2: Photonic sampled and electronically quantized ADC [2]

LiNbO₃ electro-optic modulators are by far the most developed technologies used as optical modulator in analog optical links. The ability to handle high optical powers, low dependency on wavelength and temperature and high modulation bandwidth make the LiNbO₃ modulator a very attractive candidate [7]. However being used for photonic ADCs limits the overall resolution because of the following two main reasons: (1) The required voltage to get the maximum extinction (V_{π}) is much higher than the voltage of the RF signal and thus RF amplifier with a high linear response is needed; (2) MZI has an inherent nonlinear transfer function. Among these, the associated nonlinear transfer function affects the resolution the most. To give an example, the created intermodulation tones (because of the nonlinearities) when driving the modulator with 25% depth of modulation limits the effective number of bits (ENOB) of the ADC to less than 4. Operating at a very low depth of modulation also decreases the dynamic range of the modulator significantly and for any significant number of bits, the least significant bit falls

below the thermal noise of the photodetector. There have been numerous reports on pre- or post-distortion linearization techniques [8, 9] to increase the SFDR of these modulators, showing 7-8 bits of resolution [10]. An ENOB of 9.8 has been shown in [11] using a very non-uniform quantization technique which incorporates additional components. These techniques make the photonic ADCs more complex and costly and do not achieve the required performance (more than 10 effective bits) for many applications such as radar and surveillance.

1.3. External intensity modulation

The external intensity modulators are categorized in two types based on the material and the effect incorporated; Electro-absorption modulators and electro-optics modulators. When discussing the external intensity modulators there are multiple parameters to be considered such as the voltage needed for the π phase shift (V_π), the linearity of the transfer function, optical power handling capabilities and environmental stability.

1.3.1. Electro-absorption modulators

Electro-absorption modulators (EAM) as an external modulator have been used in optical fiber communication because of their low chirp and the ability to integrate them with the other semiconductor devices. Basically they are reverse biased p-i-n diodes which the absorption layer could be a bulk active region [12] or multiple quantum wells (MQWs) [13]. By applying an electric field perpendicular to the active region, the absorption edge in semiconductor shifts to the longer wavelength (red shift). For bulk active region case the effect is called Franz-Keldysh and for the

MQWs, it is called quantum-confined Stark effect (QCSE) [14]. MQWs electro-absorption modulators are much sharper (absorption band) and faster (when applying the electric field) compared to the bulk active region [13].

The main advantage of these modulators is the low driving voltage (V_π). The V_π as low as 0.36 V at DC to > 20 GHz has been reported [15, 16]. However this modulator can handle only 2 mW of optical power and for higher optical power, the V_π also increases (1.1 V is required to handle 60 mW of optical power). Despite having low driving voltage, large bandwidth and monolithic integration capability, these modulators are sensitive to wavelength, temperature and optical power and also they exhibit large fiber coupled insertion loss (10-20 dB).

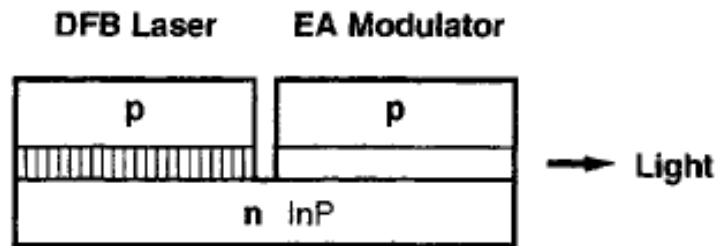


Figure 1-3: Integrated DFB laser with Electro-absorption modulator

1.3.2. Electro-optic modulators

Electro-optic modulators are based on the Pockels effect [17] which is the linear change in the refractive index of material by applying an electric field. This effect has been observed in non-centrosymmetric materials (mostly crystals and organic polymers).

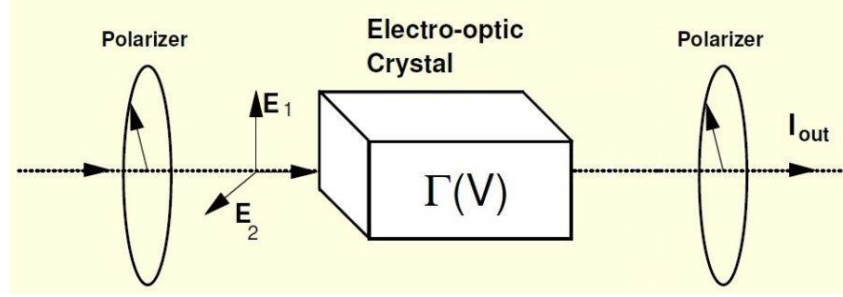


Figure 1-4: An electro-optic intensity modulator. It uses the induced retardation between the two orthogonal polarizations of the light to control the light transmission through the output polarizer.

This modulator consists of one input and one output polarizers and Pockels cell in between (Figure 1-4). The light passing through the input polarizer has two orthogonal components inside the crystal. Since the crystal is a birefringent material, these orthogonal components experience different refractive indices and create a fixed retardation. Also by applying an electric field, we will induce extra retardation as well. By adjusting the length of the crystal and with the electric field off, the crossed output polarizer blocks off the beam and by applying the voltage needed to have the π phase shift, the beam will pass through.

$$\Delta\Gamma(V) = \Gamma_{natural} + \Delta\Gamma_{induced}(V) \quad (1-2)$$

$$\Delta\Gamma_{induced}(V) = k_0 L [\Delta n_1(V) - \Delta n_2(V)] \quad (1-3)$$

The voltage required to change the induced retardation by a π is called half wave voltage,

$$\Delta\Gamma(V_\pi) = \pi \quad (1-4)$$

And so

$$\Delta\Gamma(V) = \pi \frac{V}{V_\pi} \quad (1-5)$$

After passing the output cross polarizer the output intensity as the function voltage is:

$$I_{out} = I_{in} \sin^2 \left(\frac{\Gamma(V)}{2} \right) = I_{in} \sin^2 \left(\frac{\pi}{2} \frac{V}{V_\pi} \right) \quad (1-6)$$

And if we have a driving voltage in the form of the $V(t) = V_m \sin(f_m t)$, where V_m is the peak to peak voltage and f_m is the frequency rate that we want to modulate the light with, then

$$I_{out} = \frac{I_{in}}{2} \left\{ 1 + \sin \left[\pi \frac{V_m}{V_\pi} \sin(f_m t) \right] \right\} \quad (1-7)$$

In the case of small signal modulation which $V_m \ll V_\pi$, the equation can be written as

$$I_{out} = \frac{I_{in}}{2} \left\{ 1 + \pi \frac{V_m}{V_\pi} \sin(f_m t) \right\} \quad (1-8)$$

As can be seen for the small signal modulation the relation between the output light and the input voltage is linear as shown in Figure 1-5.

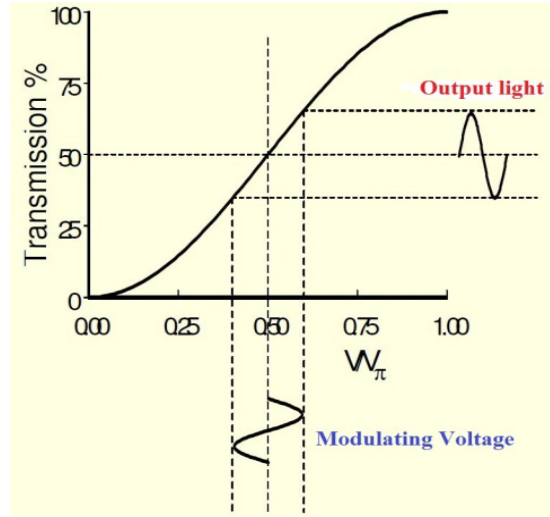


Figure 1-5: Modulated output light versus input modulating voltage for an electro-optic modulator

Among all of the electro-optic modulators, the lithium niobate (LiNbO_3) Mach-Zehnder modulator is the most developed one. This modulator has been commercialized over the past decade. As it is shown in Figure 1-6, the LiNbO_3 crystal is placed in arms with the applied voltage. The waveguides are defined by Ti-indiffusion providing low loss and stable waveguides that could couple the light to the optical fiber with a very low loss. The insertion loss of the commercialized LiNbO_3 modulators are about 4-7 dB. These modulators in comparison with electro-absorption modulators can handle higher optical powers, they are less dependent to temperature and wavelength and they respond to the frequencies as high as 100 GHz. However the driving voltage V_π increases as we want to modulate with higher frequencies, for example it increases from about

1 V to 5.1 V in order to modulate with the frequency of 500 MHz to 70 GHz [18]. However driving voltages as low as 0.18 V has been demonstrated at 30 MHz [19].

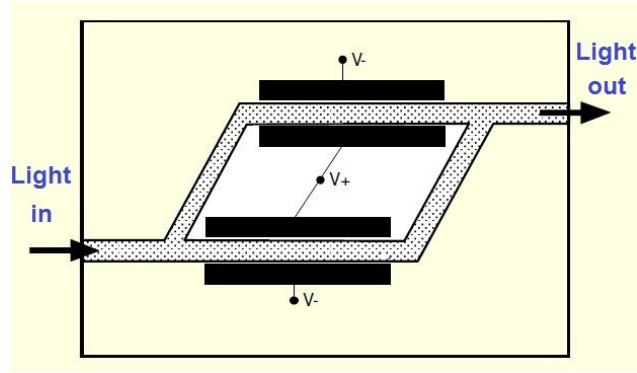


Figure 1-6: Lithium-Niobate Mach-Zehnder Intensity modulator schematic

In the Mach-Zehnder interferometer shown below with no voltage applied the beams on the two arms will be combined with no phase difference resulting unmodulated input light. Usually push-pull design has been used to introduce more efficiency. By applying voltage, there will be equal phase retardation but with different signs in each arm. So the phase difference between the arms is:

$$\Delta\phi(V) = 2 \frac{2\pi}{\lambda_0} \Delta n(V) L \quad (1-9)$$

which L is the length of the each arm. By applying this phase difference to the Mach-Zehnder transfer function

$$I_{out} = I_{in}(1 + \cos(\Delta\phi)) \quad (1-10)$$

We will have the transfer function of the intensity modulator:

$$I_{out} = I_{in} \left\{ 1 + \cos \left(2 \frac{2\pi}{\lambda_0} \Delta n(V) L \right) \right\} \quad (1-11)$$

By applying the required voltage for π phase shift difference between the arms the output intensity will be zero. So by applying a modulating voltage we can modulate the output light.

The nonlinear transfer function of the Lithium-Niobate modulator limits the spur free dynamic range of the modulator (SFDR). The SFDR which is expressed in dBc is the ratio of the power of the carrier frequency to the power of the next largest noise or spurious harmonics of the carrier. In order to measure the SFDR of the modulator usually a combination of two RF frequencies with the same power is applied (f_1 and f_2) and the SFDR is the signal to noise ratio (SNR) without observing any noise or spurious harmonics above the noise floor of the system [20]. The spurious harmonics that could fall in the bandwidth of the system are the second ($f_1 \pm f_2$) and the third order distortion ($2f_1 \pm f_2$, $2f_2 \pm f_1$). Depending on working with octave system or sub-octave system the second or third order distortion is measured, respectively. For example for a sub-octave system the $f_1 \pm f_2$ falls out of the bandwidth of the system and the third order distortion $2f_1 \pm f_2$ is measured. However the SFDR is not measured directly and it is measured from a plot which shows the photo-detected RF power of the fundamental and the third order distortion signal versus the input RF power (Figure 1-7). By fitting linear curves to these two data sets and extrapolating them to the noise floor, the SFDR will be calculated.

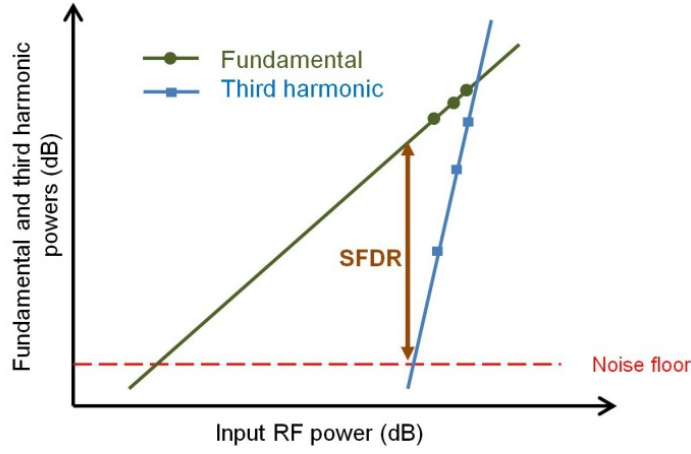


Figure 1-7: Fundamental and third-order distortion photo-detected powers versus input RF power. SFDR is calculated by extrapolating the two fitted linear curves to the noise floor.

The limited SFDR of the LiNbO₃ modulator (because of owing a nonlinear transfer function) limits the dynamic range of the analog optical link. Other modulators have been reported using semiconductor materials with a broadband response however these modulators have a high V_{π} because of a low electro-optic coefficient (compared to LiNbO₃). Also they exhibit a huge loss when coupling to the fiber because of the large refractive index difference. Organic polymers have been used to build electro-optic modulators with a large electro-optic coefficient resulting a low V_{π} and a very broadband response (113 GHz). However compared to LiNbO₃ they are sensitive to the temperature, wavelength and they cannot handle high powers.

The limited SFDR of the LiNbO₃ modulator can be improved by utilizing other techniques providing linearization scheme rather than traditional Mach-Zehnder LiNbO₃ modulators.

1.4. Linearized Modulators

The nonlinear transfer function of the conventional electro-optic LiNbO_3 modulator limits the performance of the analog data transmission links. The modern analog data transmission system tends to use more-spectral efficient techniques which could create more number of channels and less channel bandwidth and channel separations; however the inherent nonlinearity of the electro-optic modulator is the main limiting factor. Furthermore the peak to the average ratio of the broadband signal is very high and that necessitates a high dynamic range modulator (transmitter). To achieve such performances the linearization and compensation techniques (for the LiNbO_3) becomes very crucial and attractive.

Several linearization techniques such as Pre-distortion [21, 22], Post-distortion [9, 23], and feedforward [24, 25] has been proposed. All of these techniques require an additional electrical or optical component in addition to electro-optic modulator. The Post-distortion and feedforward techniques require additional optical element which makes them less cost effective. However they exhibit a good third order distortion cancelation. The Pre-distortion technique uses the electronic circuits to manipulate the RF signal applied to the device to reduce the nonlinearity at the output. This technique could be cost effective however the transfer function of the modulator used should be known accurately (this makes it difficult for the internal modulators) and also the performance is poor at high frequencies. The description of the design and performance of each of the above techniques are described in the following sections.

In this past chapter, different types of modulators (internal and external) are described and discussed. It has been seen that both of the modulators have a nonlinear transfer function and

because of that harmonic distortions show up as an unwanted signal at the output and they limit the dynamic range of the modulator and the whole optical communication system. Several linearization and compensation techniques have been described in order to reduce the third order distortion and increase the SFDR of the modulator. Some of them such as Post-distortion and feedforward methods introduce another optical element in addition to optical modulator which increase the complexity and insertion loss and makes it even less cost effective. Also reducing the SFDR requires a tight control of the applied voltages, length and coupling ratios between the devices which makes fabrication less possible. Pre-distortion technique uses an electronic circuit to compensate for the nonlinearity by manipulating the applied RF to the device. It has been shown that this technique is challenging for electro-absorption modulator since the transfer function of the modulators is very complicated. However it has been applied to the LiNbO₃ modulator with a known transfer function. This technique has improved the dynamic range for the low frequencies however the performance for the broad bandwidth system is questionable.

1.5. Injection-locking of lasers

Injection locking has been explored and studied for centuries. In 1675, Huygens observed this phenomenon between two swinging pendulum which after certain period of time the pendulum would synchronize to each other even with different initial conditions [26]. This phenomenon did not have an explanation till the development of the nonlinear dynamics by Poincare and Van der Pol. In 1966, this phenomenon was demonstrated optically for the first time [27]. Later in 1973,

Adler showed that this locking synchronization between mechanical oscillators is also applicable to electronic circuits oscillators [28].

Optical injection locking of the lasers is the process of locking the frequency and the phase of a laser which is called slave laser, to the frequency and the phase of a more stable laser which is called master laser. Experimental observation of the semiconductor laser injection locking was reported in 1980 [29]. Figure 1-8 shows the master and slave lasers with the free running oscillation frequencies of ω_1 and ω_0 , respectively. Injection locking is achieved by coupling the output light of the master laser into the slave laser. This power is usually a lot lower than the power of the free running slave laser. If the frequency of the master laser falls into a frequency range which is called locking range, then the frequency and the phase of the slave laser is locked to the master laser [30].

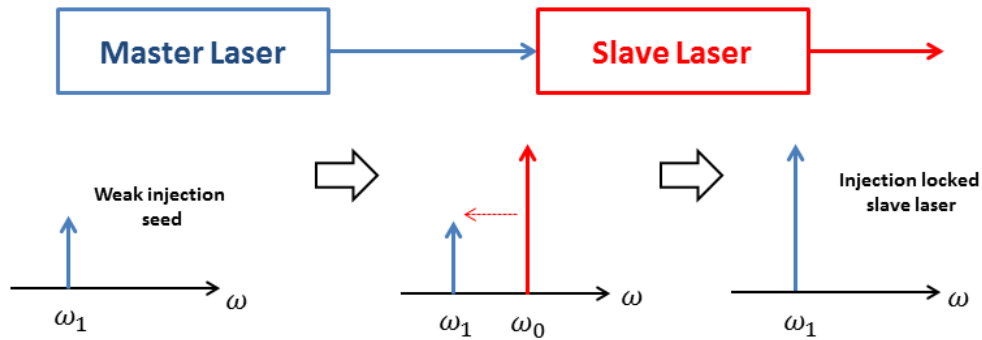


Figure 1-8: Injection locking of lasers

Figure 1-9 shows the behavior of the slave laser whether the injection seed frequency is tuned inside or outside of the locking range. Depending on the frequency detuning and the injected power ratio (the ratio between injected light and the free running slave laser powers), the injection locking could be unstable, stable or exhibit chaotic behavior. Performance of the slave laser is

improved in the stable injection locking regime. When the frequency of the master laser is outside of the locking range of the slave laser, the injection seed will be amplified and it exists with the master laser frequency. In this case the power components of each frequency exist in the slave laser and those creates a beat tone after photo-detection. Chaotic behavior of the injection-locked laser is always observed at the edge of the locking range. However when the frequency of the master laser is within the frequency locking range of the slave laser, the slave laser phase and frequency follows the phase and frequency of the master laser. The output power of the injection locked slave laser is clamped after injection locking when the seed frequency is in the locking range however this is not the case for the semiconductor laser since there is always a coupling between the refractive index and gain.

As Adler [28] showed, the phase response of the injection locked slave laser for the weak injection signals is an arcsine function of the detuning between the frequency of the master and slave lasers. In the case of not a weak injection the phase response is of the form of arctan function. Also for the weak injection locking of the semiconductor lasers, the phase response deviates from the arcsine because of the carrier density dependent refractive index.

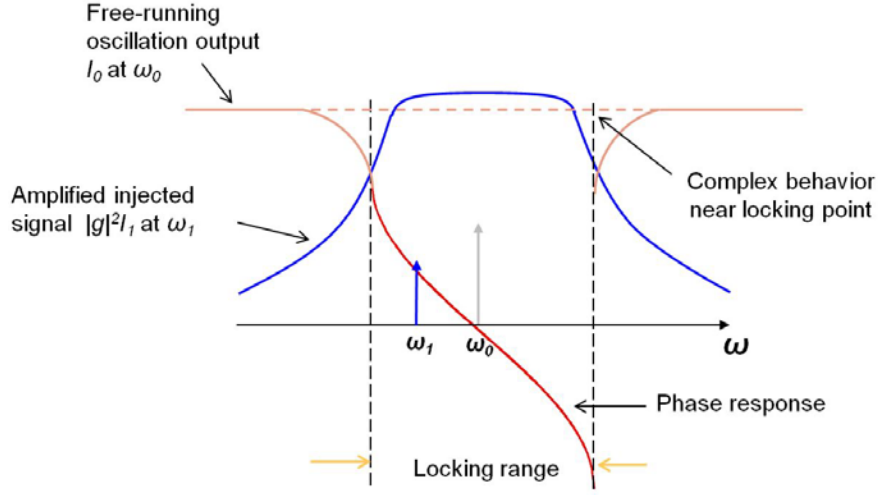


Figure 1-9: Response of the slave laser to the injection seed when it is tuned to inside or outside of the locking range [30]

1.6. Linearized interferometric intensity modulator for CW light using an injection-locked VCSEL

This modulator provides linear intensity modulation which is an ideal modulator for high dynamic range modulation without using any compensation or linearization techniques. The key to the modulator is the injection-locked resonant cavity as the arcsine phase modulator which is placed in one of the arms of the conventional Mach-Zehnder interferometer. This resonant cavity is a laser which is injection locked to the input light of the modulator. Based on the steady state solution of the Adler's equation, an injection locked laser produces an arcsine phase response when it is modulated within the frequency range called locking range. This phase imparted by the injection locked laser is the function the detuning of the resonant frequency from the injection seed frequency and it is

$$\varphi(\omega_1) = \sin^{-1} \left(\frac{\omega_0 - \omega_1}{\omega_m} \right) \quad (1-12)$$

where ω_0 is the cavity resonance frequency, ω_1 is the injected seed frequency which is the input light to the modulator and ω_m is the half of the locking range. By modulating the frequency of the injection-locked laser (by modulating the current of the resonant cavity), one can impart an arcsine phase modulation on the injection-locked resonant cavity and by interfering the modulated signal with its unmodulated counterpart at the other arm in quadrature, the output will be directly proportional to the function used to modulate the resonant cavity (Equation (1-13)). The schematic diagram of this true linearized modulator is shown in Figure 1-10.

$$I_{out} = I_{in} \left\{ 1 + \cos \left(\sin^{-1}(f(t)) - \frac{\pi}{2} \right) \right\} = \frac{I_{in}}{2} (1 + f(t)) \quad (1-13)$$

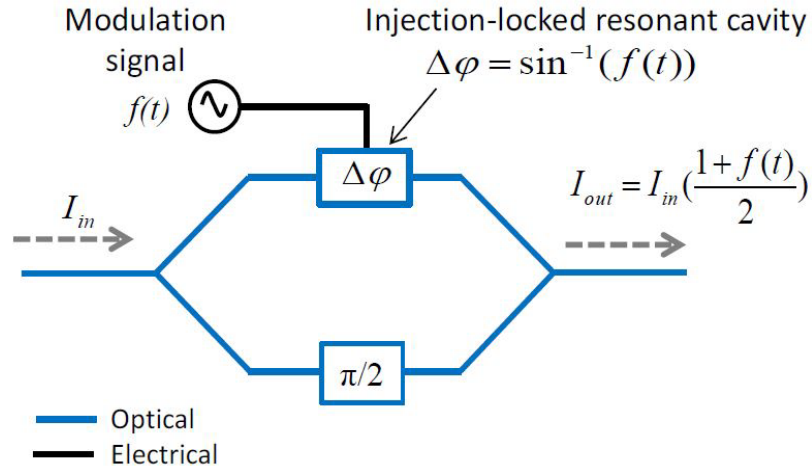


Figure 1-10: Schematic diagram of the true linear interferometric intensity modulator [31]

Numerical simulations has been demonstrated in [32] comparing the conventional LiNbO₃ Mach-Zehnder modulator and the true linear interferometric intensity modulator assuming a perfect arcsine phase modulator. As it is shown in Figure 1-12, the SFDR of the linear modulator when it is biased at quadrature is noise limited. However a typical LiNbO₃ electro-optic modulator biased at quadrature shows almost 70 dB for SFDR at 10% depth of modulation, and it decreases for the higher depth of modulations. However linear modulator gives more than 100 dB at this depth of modulation and it doesn't decrease for the higher depth of modulation.

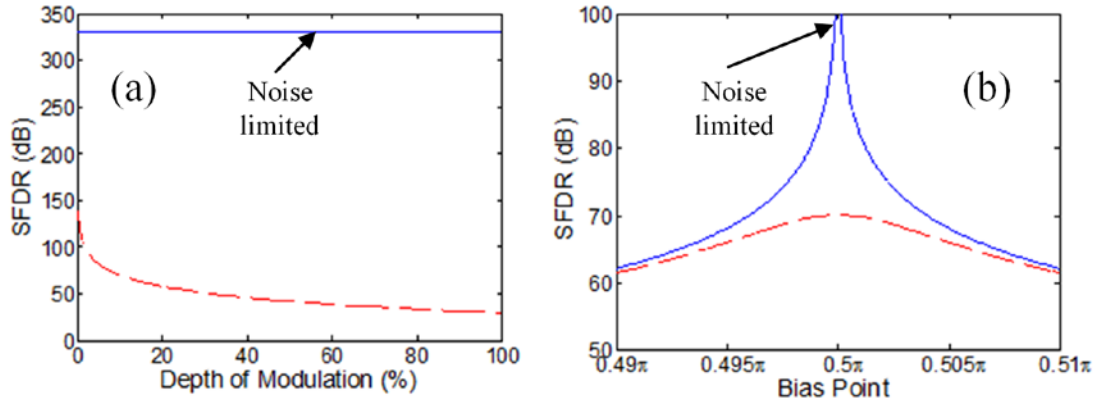


Figure 1-11: Numerical results of the performance of the typical LiNbO₃ electro-optic modulator (red) and the true linear interferometric modulator (blue), a) SFDR versus depth of modulation, b) SFDR versus bias point of the modulator for the 10% depth of modulation [32]

However it should be mentioned here that the simulation results shown for the linear interferometric setup are for the perfect arcsine phase modulator. However in practice the induced

phase modulation of the injection-locked laser deviates from the ideal case (perfect arcsine) due to the carrier density dependent refractive index and that limits the SFDR of this modulator.

The concept of the arcsine phase modulation using an injection locked laser has been demonstrated by Kobayashi and Kimura [33] for the first time. This has been done by injection locking of a single longitudinal mode Fabry-Perot laser by another same laser inside the Mach-Zehnder interferometer. A static π phase shift has been observed from the arcsine phase modulator and the correspondent phase modulation also observed at the output.

The first demonstration of the true linear interferometric intensity modulator has been reported by Hoghooghi et. al. [34] using a single mode Vertical Cavity Surface Emitting Laser (VCSEL) as the resonant cavity (arcsine phase modulator). The schematic diagram of this modulator is shown in Figure 1-12. The VCSEL used in the experiment is a commercially fiberized device operating at 1550 nm which can be tuned by ~ 3.3 nm. Device length is ~ 6 μm and has a threshold current of ~ 2 mA and maximum output power of 1.025 mW.

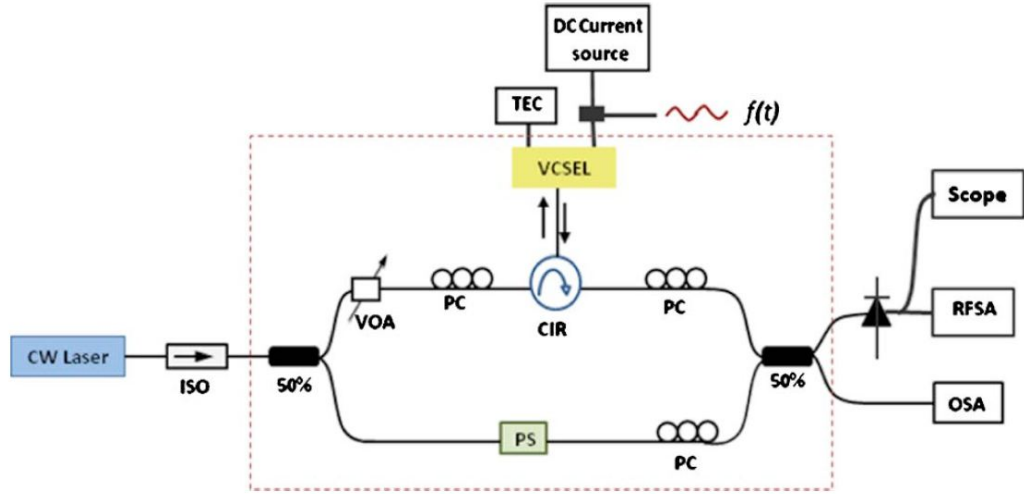


Figure 1-12: Schematic diagram of the true linear interferometric intensity modulator using and injection-locked VCSEL as a resonant cavity. VCSEL: Vertical cavity surface emitting laser, TEC: Thermo-electric cooler, VOA: Variable optical attenuator, PS: Phase shifter, PC: Polarization controller, Iso: Isolator, CIR: Circulator, RFSA: Radio frequency spectrum analyzer, OSA: Optical spectrum analyzer [34]

All of the components shown in Figure 1-12 are fiberized components. A CW laser input source to the modulator with 150 KHz short-term stability and narrow linewidth (<1 KHz) has been used because of the stability needed for the injection locking. A variable optical attenuator and a polarization controller have been used to control the intensity and polarization of the light going into the VCSEL. The ratio between the injected power and the VCSEL power defines the locking range of the VCSEL in the reflection mode. A phase shifter has been used to keep the interferometer always in quadrature. By modulating the current of the VCSEL with the function of $f(t)$ one can modulate the carrier density modulation which consequently modulates the

refractive index and finally we obtain frequency modulation of the resonant cavity according to the $f = c/2nl$. According to the Adler's equation an arcsine phase response is imparted on the output of the injection-locked laser. Then the arcsine phase modulated signal is interfered with its unmodulated counterpart from the other arm at quadrature and the result will be a true linear intensity modulator.

Figure 1-13 shows the static phase shift induced by injection-locked VCSEL. This has been done by changing the DC bias current of the VCSEL around the bias point. The total phase shift of 0.7π observed for 52 μA change in the DC current. The arcsine fit to this data is also shown in Figure 1-13. Using the known impedance of the VCSEL, the required voltage to achieve the π phase shift is calculated to be 2.6 mV.

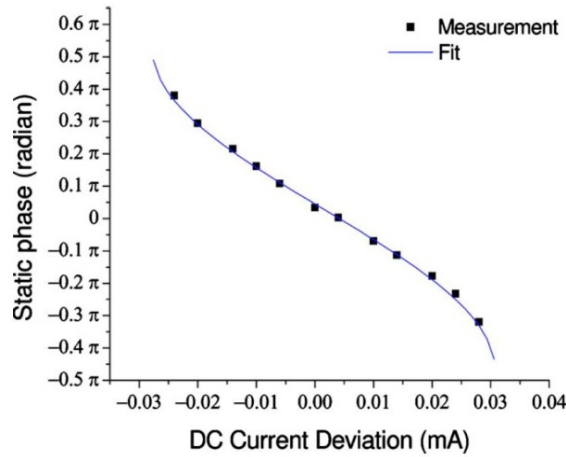


Figure 1-13: Static phase shift of the injection-locked VCSEL and the arcsine fitted curve [34]

Figure 1-14 shows the frequency response of the linear modulator which provides 5 GHz bandwidth on 10 dB below the maximum value. However this is limited by using of a commercialized VCSEL and could be increased by using a better designed and packaged VCSEL.

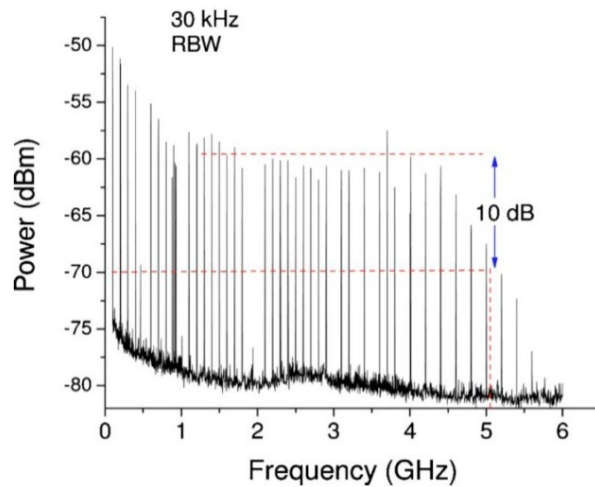


Figure 1-14: The frequency response of the true linear intensity modulator [34]

The two-tone intermodulation has been done to calculate the SFDR of this modulator. This has been performed by applying two equal power RF tones at 300 MHz and 400 MHz and by looking for the third order distortion which is expected to be at 500 MHz at a very low resolution. The SFDR is measured to be 95 dB, however it is claimed to be limited by the noise floor and the instability of the fiberized system. This instability caused by the fluctuation of the fiberized system causes instability in the path length and finally makes the interferometer out of quadrature.

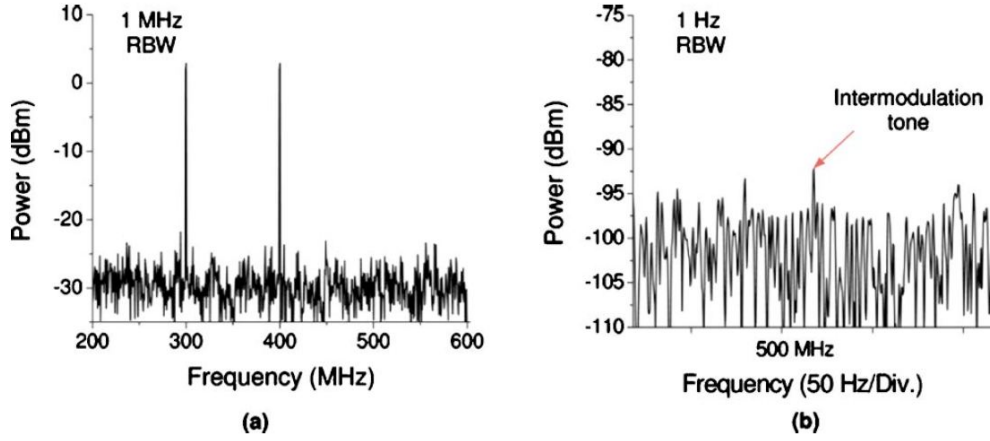


Figure 1-15: SFDR measurement, a) shows the power spectrum of the RF photo-detected signal consists of two equal power tones at 300 MHz and 400 MHz, b) shows the third order distortion at 500 MHz at the resolution bandwidth of 1 Hz [34]

1.7. This Thesis

In this thesis, we propose and experimentally demonstrate a true linearized intensity modulator for pulsed with a very low V_π and a high SFDR. This modulator can be used inside an analog optical link and can potentially improve the performance and resolution of the photonic analog to digital conversion.

In Chapter 2, we discuss in the details the fabrication steps needed to fabricate vertical mesa profile edge emitter lasers using a novel multiple quantum well AlGaInAs material system. This material system provides uncooled operation over a larger dc bias range and also a large range of reverse bias voltages. The fabrication steps involves standard UV lithography and wet etching techniques. BCB has been used for planarization and contacts have been deposited using a thermal

evaporator. The substrate has been thinned down to about 100 μm and devices are cleaved into individual bar and mounted p-side up on the copper stud. The temperature of the device is controlled using a thermo-electric cooler and a PID controller.

In Chapter 3, we show the first time demonstration of directly modulating a mode-locked laser at high frequencies. This has been achieved by carefully minimizing the metal pad size and using the BCB for passivation. Also high speed probe is used to apply the signal to the saturable absorber and the gain section in such a way that the gain section serves as a floating ground and thus reverse biasing the saturable absorber section. This has provided an effective fundamental hybrid mode-locking at 23 GHz with superior advantages compared to sub-harmonic mode-locking.

In Chapter 4, we experimentally demonstrate a true linearized intensity modulator for pulsed light for photonic ADCs application. This is made possible by introducing a two-section mode-locked laser (slave) into one of the arms of the Mach-Zehnder interferometer and injection-locking it to the input light to the interferometer (which is an identical laser to the slave laser). By modulating the slave laser one can introduce an arcsine phase response on all of the injected combs lines (according to Adler's equation) and by combining it with its unmodulated counterpart (other arm) at quadrature, one can realize a true linearized intensity modulator. The experimental results such as static phase response, optical and RF spectra have been presented. The current of the gain section or the voltage of the saturable absorber section has been used for modulation. However modulating the saturable absorber produces a smaller third-order nonlinearity when compared to modulating the gain. This is simply because of the carrier density modulation created when

modulating the current of the gain section which ultimately leads to an unwanted amplitude modulation. Finally, the results for the two-tone intermodulation experiment (as a measure of the linearity of the modulator) has been presented for the two above cases.

In Chapter 5, we propose a new three-section laser to address the issue of the unwanted amplitude modulation when modulating the slave laser. We propose the addition of a new passive-section (which is transparent at the operating wavelength of the laser) to the previous two-section design. The amplitude modulation would be suppressed when modulating this phase section since there won't be any absorption. By doing that we are able to decouple the phase and amplitude responses. Impurity free vacancy disordering (IFVD) technique has been used to blue shift the photoluminescence of the passive section. The experimental results for the ultra linear modulator has been presented. This results shows an almost six-fold reduction in V_π (to about 1mV) and the two-tone intermodulation experiment also shows 5-dB SFDR improvement for this modulator.

2. ALGAINAS MULTIPLE QUANTUM WELL MODE-LOCKED LASER FABRICATION

2.1. AlGaInAs multiple quantum well wafer

A new and promising AlGaInAs-InP strained quantum well material at 1.55- μm has been used for fabricating Fabry-Perot and mode-locked lasers. This material system is going to replace the conventional InGaAsP-InP material because of a larger conduction band discontinuity ($\Delta E_c = 0.72 \Delta E_g$) and a smaller valence band discontinuity [35]. The former enables uncooled operation over a large dc bias range and the latter enables a large range of bias voltage, which in fact makes the pulses from the mode-locked lasers shorter. The wafer is grown by Metal Organic Vapour Phase Epitaxy (MOVPE) on a 625 μm thick sulfur doped InP substrate by IQE (Europe) Ltd. in Cardiff, Wales, UK. As it is shown in Table 1, wafer growth began by forming 0.8 μm of n-type silicon doped InP as the buffer and cladding. The active layers consist of five compressively strained wells (6 nm) and six slightly tensile strained barriers (10 nm). Figure 2-1 shows the photoluminescence (PL) spectrum of the wafer taken at room temperature using an in-house PL measurement setup explained in chapter 5. The peak of the emission is at 1524 nm with the 3-dB bandwidth of 80 nm. Active layers growth are followed by a 50 nm InGaAsP as the wet etch stop. The entire structure is capped with 1.6 μm zinc doped InP as the p-cladding followed by two highly p-doped contacts layers of InGaAsP (50 nm) and InGaAs (200nm) with doping concentration of $3 \times 10^{18} \text{ cm}^{-3}$ and $1.5 \times 10^{19} \text{ cm}^{-3}$, respectively.

Table 1. AlGaInAs multiple quantum well wafer layer structure

Layer	Repeat	Description	Material Type	Thickness (μm)	C-V level (Cm^{-3})	Type	Dopant
13		CAP	InGaAs	0.2	$>1.5\text{e}+19$	p	Zn
12		p-Transition	InGaAsP	0.05	$>3\text{e}+18$	p	Zn
11			InP	0.1	$>1\text{e}+18$	p	Zn
10		p-Cladding	InP	1.5	$1\text{e}+18$	p	Zn
9		Wet etch stop	InGaAsP	0.05	$1\text{e}+18$	p	Zn
8		p-Cladding	InP	0.05	$7\text{e}+17$	p	Zn
7			AlGaInAs	0.1	-	U/D	Undoped
6	5	Well	AlGaInAs	0.006	-	U/D	Undoped
5	5	Barrier	AlGaInAs	0.01	-	U/D	Undoped
4			AlGaInAs	0.1	-	U/D	Undoped
3		n-Cladding	InP	0.5	$1\text{e}+18$	n	Si/S
2		n-Buffer	InP	0.3	$3\text{e}+18$	n	Si/S
1		Substrate	InP	625	$3.8\text{e}18$	n	S

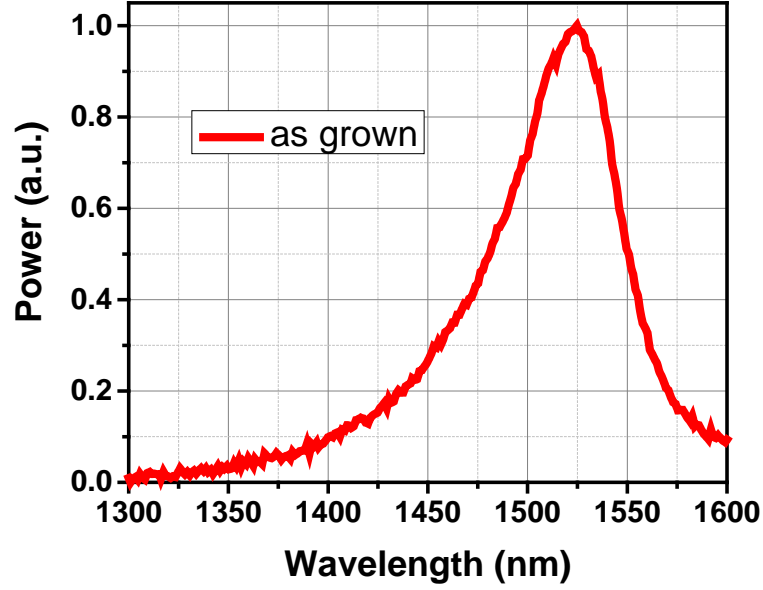


Figure 2-1. Photoluminescence spectrum of the as grown wafer at the room temperature.

2.2. Waveguide analysis for single mode operation

The waveguide analysis has been done using the commercialized simulation software BeamPROP™ [36]. The software is based on the Beam Propagation Method (BPM) and it is well suited for design and simulation of integrated waveguide devices.

Here the goal is to have an edge emitter laser than can only support one single transverse mode. This is important since a waveguide than can support more than one mode could provide a multimode laser with complex characteristics. Based on the wafer structure available and fabrication methods that can be utilized, simulation has been done to determine the dimensions

and the shape of the waveguides needed for single mode operation. There are three waveguide profiles (Figure 2-2) that can be achieved depending on acids used for wet etching and also the waveguides orientation with respect to major axis of the wafer. It is known that InP compound crystalizes in the zinc-blende structure, producing two interpenetrating face centered cubic (FCC) sub-lattices with each sub-lattice containing one kind of atom. This makes the InP wet etching to be an anisotropic and orientation dependent wet etching process [37-39].

Here in this thesis since the wet etching has been used as the primary method to make the waveguides, the height of the waveguides is dictated by the wet etch stop layer depth and that is about 1.85 μm . This has been a constant parameter when studying the waveguides using the BeamPROPTM software. The only two remaining parameters are the width of the waveguide and the profile of the waveguide which here is limited to the vertical mesa and mesa (since the reverse mesa is not of the interest here because of mode profile and wafer structure).

Figure 2-3 shows the results of the simulation of a mesa waveguide with a height of 1.85 μm and a width of 3.6 μm . It can be seen that there could be four transverse mode supported by this mesa waveguide which at least the first two should exist at the same time. Here it needs to be mentioned that only the area beneath the mesa region will experience the carrier injection thus making any existing part of the mode outside of this region impossible. The width of the waveguide is decreased here to obtain a single mode waveguide however the needed width would be impractical to fabricate. This leads us to only vertical mesa with vertical wall profile and with only parameter to play with when doing the simulation.

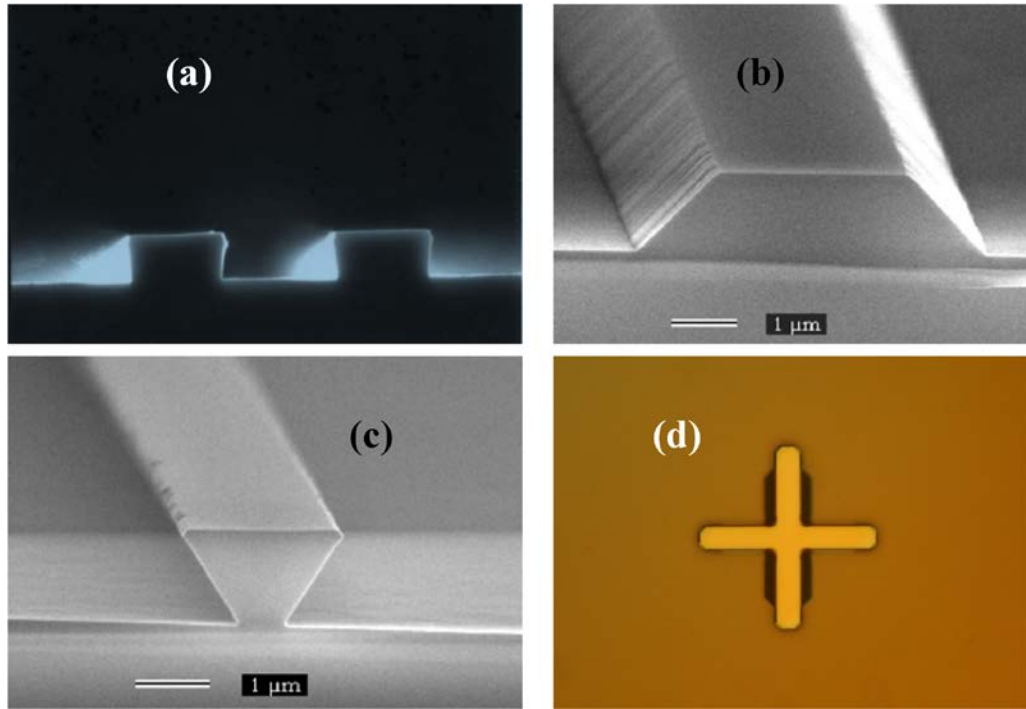


Figure 2-2. InP wet etching profiles (a) Vertical mesa with the vertical walls (b) Mesa with the walls at an angle of ~ 45 degrees and (c) Reverse mesa with the walls at angle of ~ -45 degrees.

(d) Real image of the fabricated alignment marks on quantum well wafer (top view). The sidewalls of the vertical features could be seen easily (dark area) as a proof of mesa profile. However the horizontal features sidewalls are not observable from the top view suggesting that they are either vertical mesa or reverse mesa.

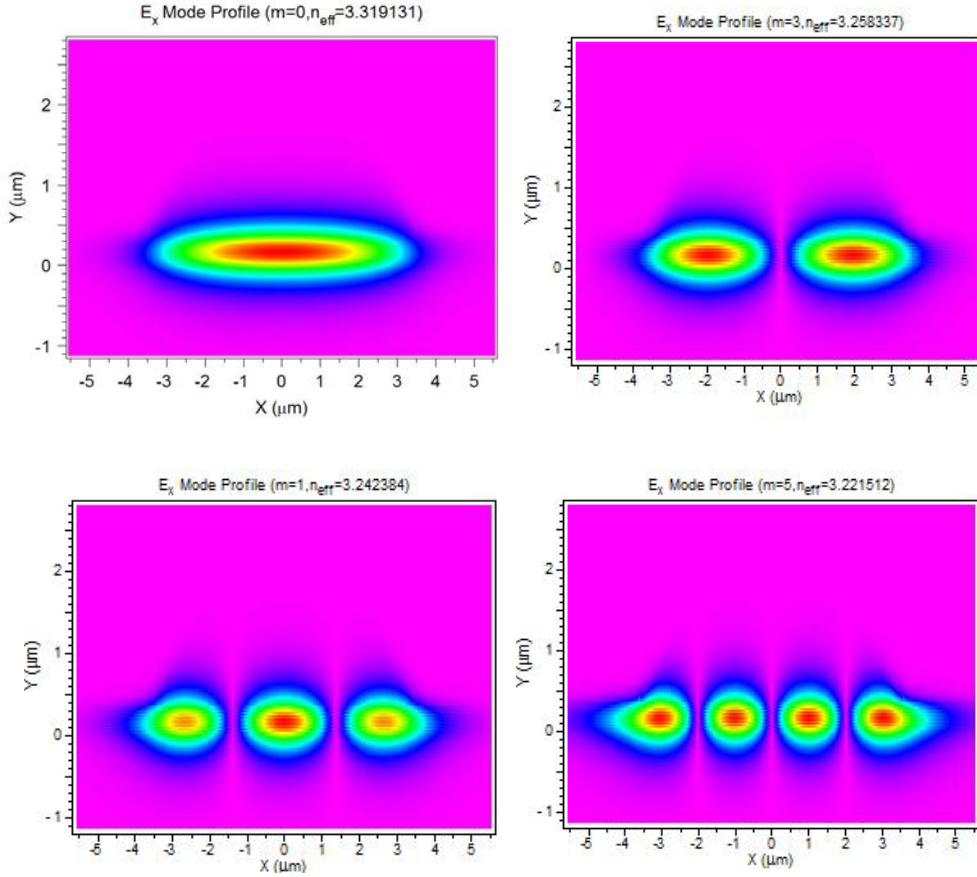


Figure 2-3. Four possible simulated transverse modes from a mesa waveguide with the width of $3.6\ \mu\text{m}$ and the height of $1.85\ \mu\text{m}$.

Figure 2-4 shows two possible transverse mode obtained from the simulation of $2.5\ \mu\text{m}$ wide and $1.85\ \mu\text{m}$ tall vertical mesa waveguide. As can be seen the second mode (Figure 2-4 (b)) is unlikely to exist since a considerable amount of mode is outside of the walls of the waveguide. So this waveguide with the dimension of $2.5\ \mu\text{m}$ by $1.85\ \mu\text{m}$ with the vertical mesa profile could operate in the single transverse mode regime.

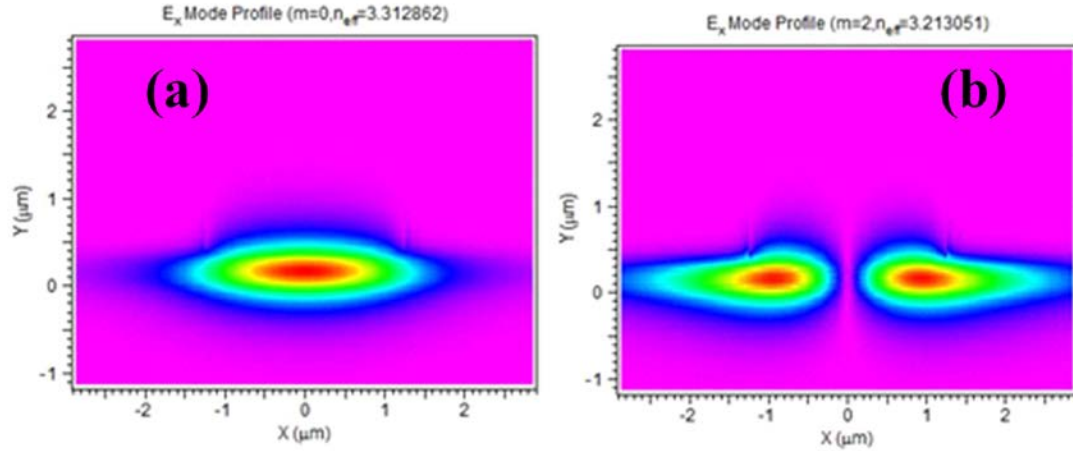


Figure 2-4. Two possible transverse mode obtained from simulating a vertical mesa waveguide with $2.5\ \mu\text{m}$ width and $1.85\ \mu\text{m}$ height. The second mode is very unlikely to exist since it doesn't see the carrier injection outside the waveguide walls.

2.3. Mask design

L-Edit of Tanner Research Co. [40] has been used to draw features such as waveguides, metal pads, alignment and cleaving marks. This has been used to export the features to GDSII file format for mask production. The mask has been produced by Photo sciences Inc. using an electron beam lithography system with a resolution of $150\ \text{nm}$. The features are made of chrome on a 4 inch by 4 inches quartz glass.

Figure 2-5 shows a captured image from the L-Edit software of the simple $2\ \text{mm}$ Fabry-Perot laser design. The $2.5\ \mu\text{m}$ waveguide is shown in blue and it is overlapped intentionally with metal pads (in green). Other features are serving as alignments and cleaving marks.

A simple C program has been developed to be able create these features and ultimately be able to create a laser bar. This is useful since it enable us to have as many as laser possible in the sample that being processed.

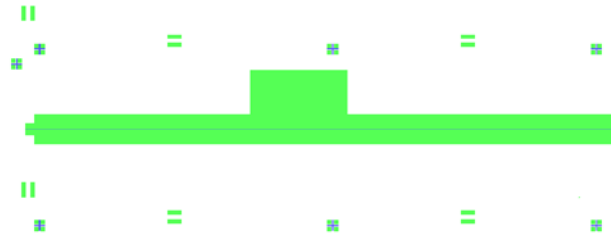


Figure 2-5. Image of the simple Fabry-Perot laser design from L-Edit software showing waveguide and alignment marks in blue and metal pads, alignment marks and cleaving marks in green.

2.4. Fabrication procedure

2.4.1. Wafer cleaving

Before cleaving the wafer the major and minor axis of the wafer has to be identified. This is critical since the wet etching of the InP based materials are anisotropic and it is not the same in the two planes of the wafer [41]. So as the first step the major axis is identified and the back side of the wafer is slightly scratched with diamond-tipped scriber with lines parallel to the major axis of the wafer. This ensures that the major axis won't be missed when cleaving the wafer in to small pieces.

2.4.2. Sample cleaning

After cleaving the sample is blown by N_2 gas as the primary step to remove big particles created when cleaving. The sample then soaked in a DI water-filled soft plastic container and placed in ultrasonic bath for 2 min. The sample then thoroughly rinsed with DI water and dried with N_2 gas and baked for 2 min at 120°C to remove any residual volatiles. Additional one minute intervals of ultrasonic bath is used if the sample was not clean after the first two minutes. Then the sample is thoroughly rinsed with acetone and methanol and isopropanol subsequently and dried with N_2 to remove any organic residue. If more cleaning is required the sample could be soaked subsequently into acetone, methanol and isopropanol bath at 100°C for 5 min.

The cleaning is followed by Si_3N_4 deposition to cover the sample and avoid any surface oxidization.

2.4.3. Si_3N_4 deposition

Because of harsh acidic nature of InP wet etchant, photoresists and oxide dielectric masking layers cannot resist the time needed to be able to etch $1.6\text{ }\mu\text{m}$ of InP. However Si_3N_4 is totally resistant to those acids and can be used as a mask when etching the first two layers (InGaAs and InGaAsP). After removing the first two layers, since the InGaAs layer is resistant to InP etchant acids, it can be used as an additional mask for InP wet etching.

Plasma Enhanced Chemical vapor deposition (PECVD) method has been used to deposit dielectric layers [42]. This has been done using a dual chamber Plasma Therm 790 series system. One chamber is dedicated to deposition and the other one is used for etching. The plasma created

by applying an RF signal at 13.56 MHz between the shower head plate and the ground plate. Depending on the gases used, interaction with the sample surface could provide deposition or etching. Table 2 shows the parameters for the “SIN-DIFF” recipe which have been used for Si_3N_4 deposition. The deposition rate can be changed by changing the gases amount, temperature, chamber pressure and also the RF power. It is also dependent to the substrate properties such as doping and also substrate thickness. It is very important to characterize the deposition rates of the machine frequently.

200 nm of Si_3N_4 is deposited on a cleaned sample using the “SIN-DIFF” recipe. This could protect the selected areas and gives us the ability to etch InGaAs and InGaAsP selectively from InP.

Table 2. Deposition parameters of the recipe “SIN-DIFF” for Si₃N₄ deposition. The silane gas (SiH₄) used is 2% silane diluted in N₂.

Parameters	Si ₃ N ₄
SiH ₄ (sccm)	120
NH ₃ (sccm)	4.56
N ₂ (sccm)	400
Temperature (°C)	246
Pressure (mTorr)	900
RF power (W)	20
Deposition rate (nm/min)	8-10

2.4.4. UV photolithography and Si₃N₄ etching

Positive resist PR1805 is used for photolithography. This photoresist is about 500 nm thick and can provide the resolution needed for 2.5 μ m waveguide fabrication. Exposure has been done using a Karl Suss MJB3 machine. Here the waveguides are perpendicular to the major axis in order to obtain 2.5 μ m vertical mesa waveguide needed for single mode operation. The steps needed for photoresist spin-coating, photolithography and finally transferring the features to the Si₃N₄ dielectric layers are summarized below:

1. Spin-coat the PR1805 @ 3500 rpm for 40 seconds

2. Pre-bake @ 120 °C for 4 min
3. UV Exposure @ 12 mW for 5.5 seconds
4. Develop in AZ351 and DI water (ratio of 1:7) for ~ 25 seconds
5. Post-bake @ 120 °C for 4 min
6. Run recipe “Descum” on PECVD for 2 min
7. Run recipe “etchsin1” on PECVD for 4 min
8. Photoresist removal. Dip the sample in acetone @ 80 °C for 5 min then rinse with acetone, methanol and isopropanol and dry with N₂
9. Run recipe “prremove” on PECVD for 30 seconds.

The recipe “Descum” on the PECVD machine has been used to remove any remaining photoresist in the developed area. The parameters for the “Descum” are listed in Table 3. This recipe is very mild etching recipe using oxygen and helium gases at a low power of 60 W and a low pressure of 40 mTorr. A mixture of Oxygen and tetrafluoromethane (CF₄) has been used to etch Si₃N₄ layer (“etchsin1” recipe shown in Table 3). It is needed to be mentioned that the etching rate of 75 nm/min is obtained using the Si₃N₄ layer deposited using the “SIN-DIFF” recipe. After completely removing the photoresist by dipping the sample into the acetone bath, the remaining thin layer of photoresist is removed by using the PECVD with a much harsher etching recipe (prremove.prc) for the photoresist removal. The “prremove.prc” uses the same ratio of oxygen and helium at the higher processing pressure of 300 mTorr and RF power of 100 W.

Table 3. Reactive Ion Etching (RIE) parameters for photoresist and Si₃N₄ etching. Etching has been done in the room temperature.

Parameters	Descum.prc	prremove.prc	etchsin1.prc
O ₂ (sccm)	20	50	1.0
He (sccm)	10	50	-
CF ₄ (sccm)	-	-	12
Pressure (mTorr)	40	300	75
RF power (W)	60	100	100
Etching rate (nm/min)	-	-	75

2.4.5. Wet etching

There are three layers to be etched away by acids here to be able to form the single mode ridge waveguide. The first layer is 200 nm of highly doped InGaAs. The second layer is 50 nm of InGaAsP and the third layer is 1.6 μ m of InP. The first two layers could be etched away by using sulfuric acid (H₂SO₄) or phosphoric acid solution (H₃PO₄) and the 200 nm thick Si₃N₄ layer would be a very good mask for this step. Table 4 shows the etching rates of the solutions based on H₂SO₄ and H₃PO₄ acids for the two first layers. Hydrogen peroxide (H₂O₂) and Deionized water (H₂O) are added as oxidizer and diluting agents, respectively [43].

Table 4. Wet etching rate of the H_2SO_4 and H_3PO_4 acids solution for the InGaAs and InGaAsP layers [44, 45].

Acid solution				Etching rate (nm/min)	
H_2SO_4	H_3PO_4	H_2O_2	H_2O	InGaAs	InGaAsP
1	-	1	10	400	100
-	1	1	30	125	15

The InGaAs could be etched easily using a solution of phosphoric acid: hydrogen peroxide: deionized water with the etching rate 125 nm/min. However this etchant is not suitable for InGaAsP etching since the etching rate is too slow (15 nm/min). This could be addressed by using the sulfuric acid-based solution. This etchant provides etching rates of 400 and 100 nm/min for InGaAs and InGaAsP, respectively. Despite the higher etching rates, this acid still provides a good etch selectivity with InP.

The first two layers are etched in one step using the $\text{H}_2\text{SO}_4:\text{H}_2\text{O}_2:\text{H}_2\text{O}$ (1:1:10) solution. The etching time required is about 75 seconds. The sample is dipped in DI water and then rinsed thoroughly with DI water for 1 min and dried with N_2 gas. At this point the total height of the features (measured using α -stepper profilometer) is about 450 nm.

At this point the prremove.prc recipe from PECVD has to be used for almost 17 min to remove all the remaining photoresist. This is important since there are still some areas at the edges of the sample that the photoresist is not completely removed from top of the Si_3N_4 . The remaining

photoresist could be possibly dissolved by the harsh etchant used to etch InP and form a mask in the middle of the sample.

There are many acid combination that can be used to selectively etch InP and not InGaAs and InGaAsP such as such as hydrochloric acid (HCl), hydrobromic acid (HBr), and Nitric acid (HNO₃). Table 5 shows the etching rate of some of the acid solutions. Hydrobromic acid solution provides a very controllable etching rate of 400 nm (when mixed with DI water with the ratio of 2:1) and a good selectivity however it can only create mesa and reverse mesa profiles.

InP etching solutions based on HCl are extremely fast and usually are accompanied by producing of microbubbles [46]. These microbubbles could results to not a smooth surface if the whole InP layer is not removed. Etching rate could be easily reduced by diluting the acid by the DI water. Also lactic acid (CH₃CHOHCO₂H) and acetic acid (CH₃CO₂H) could be used to reduce the amount of micro-bubbling [47]. Table 5 shows some of the suggested solutions with good balance between the etching rate and microbubbling formation.

Table 5. InP etching rate of different acid solutions [41, 46, 47]

Acid solution						Etching rate (nm/min)
HCl	HBr	CH ₃ CO ₂ H	H ₃ PO ₄	CH ₃ CHOHCO ₂ H	H ₂ O	InP
-	2	-	-	-	1	400
1	-	6	-	-	-	825
2	-	-	5	2	-	240
1	-	-	1	-	-	2000

The acid solutions suggested here based on hydrochloric acid, lactic acid and acetic acid provide a controllable etching rate and a decent surface smoothness. However they are good when etching thin layers of InP and not thick layers because of the following reason. When etching thick layers of InP (more than a micron) it is very challenging to maintain a uniform etching on the sample. The etching rate is always is higher in the middle of the sample compared to other area. To address this the sample is moved and rotated inside the solution however still challenging to achieve the same etching rate for everywhere in the sample. Also because of the microbubble formation, the surface always contains some micron size features (as shown in Figure 2-6). This happens when the InP layer is etched partially and the whole layer of InP is not removed.

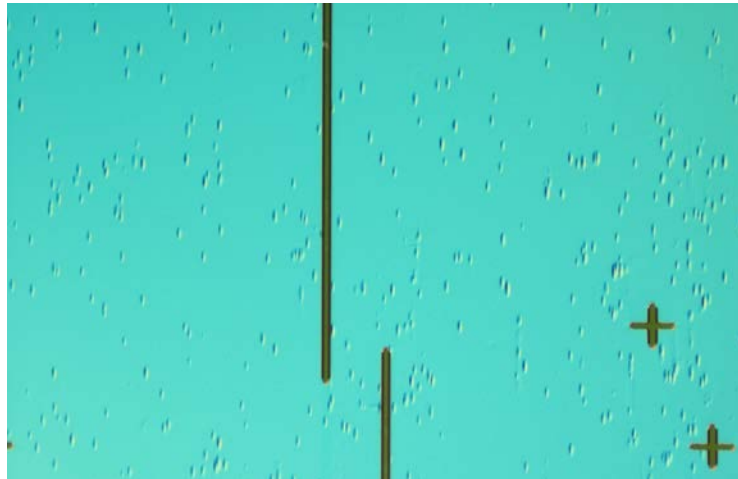


Figure 2-6. Sample containing two waveguides which they are formed using hydrochloric and lactic acid mixture. The waveguide are $1.6\text{ }\mu\text{m}$ deep and $2.5\text{ }\mu\text{m}$ wide. The micron size features next to the waveguides are produced because of the microbubbling.

Another acid solution is suggested by adding the phosphoric acid to the hydrochloric acid with the ratio of 1:1 [48, 49]. This acid solution provides a fast etching rate of $\sim 2 \mu\text{m}/\text{min}$. This is very suitable for the application here since we want to remove the whole $1.6 \mu\text{m}$ thick InP layer. The InGaAsP layer after beneath the InP layer acts as a reliable etch stop layer for this acid mixture. This solution also provide a very good uniformity.

As expected the etching is accompanied with the formation of microbubbles and it means that the first two layers are being successfully removed. The sample has to be removed from the solution shortly after the microbubbling stops. This is to ensure that the whole $1.6 \mu\text{m}$ layer of InP etched away. The sample is then dipped in DI water and also thoroughly rinsed with DI water for 1 min as to remove any loose InP particle from the surface of the sample. Figure 2-7 shows the top view images of the waveguides fabricated taken using a microscope.

Finally, the Si_3N_4 masking layer on top of the waveguides are removed by running the etchsin1.prc recipe for 5 min. At this point the total height of the waveguides measured with the profilometer should be $1.85 \mu\text{m}$ since InP etching is stopped above the etch stop layer.

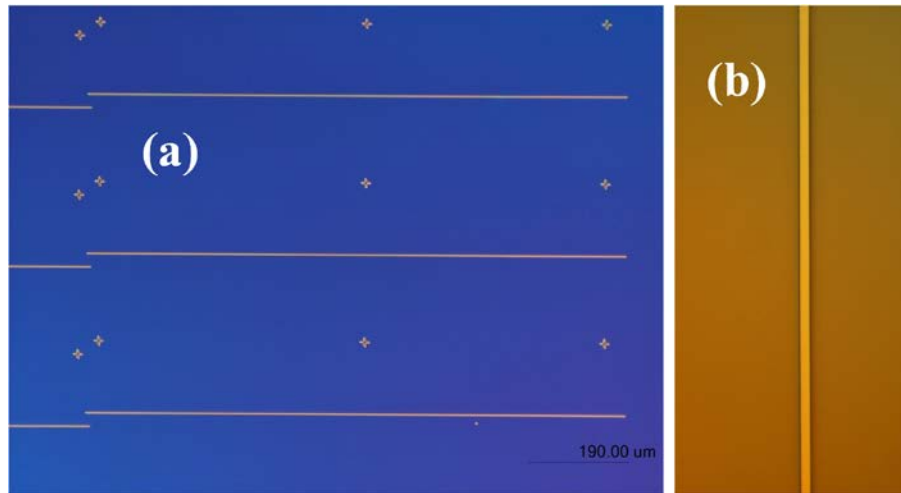


Figure 2-7. (a) Top view image from the fabricated vertical mesa waveguides, (b) the zoomed-in version of the fabricated waveguide 2.5 μm waveguide. Different color of the images coming from the different filters used when working with the microscope and does not show any information.

2.4.6. BCB planarization

Planarization has to be done on the waveguide in order to facilitate passivation and be able to put contacts for current injection. This can be done using dielectric layers such as SiO_2 or Si_3N_4 or resists such as Hydrogen silsesquioxane (HSQ) or polymers such as Benzocyclobutene (BCB). Among these BCB are the hardest to process however it provides an excellent planarization, a low dielectric constant and a small leakage current. Additionally it has a very good thermal stability and superior chemical resistance when it is cured. The steps that are needed for planarization and passivation are summarized below:

1. Spin-coat the adhesion promoter AP3000 @ 4000 rpm for 40 seconds
2. Spin-coat the cyclotene 3022-46 @ 4000 rpm for 40 seconds
3. Hard-cure the BCB @ 250 °C for 60 min using the convention oven under nitrogen ambient (the oven cure profile is shown in Table 6).
4. Dry etch the BCB using the cyclotene.prc recipe (Table 7) of the PECVD machine. Continue the dry etching until the BCB is removed from the top of the waveguide. At this point the height measured using α -stepper should be about 250 nm and not more than 300 nm. The total time could be between 9 to 11 min.
5. Soak the sample into the Ash residue remover Rezi-Baker 28 @ 50 °C for 5min and then thoroughly rinse with DI water and dry with N₂.

Table 6. The temperature profile used for BCB hard-curing

Step	Full Cure
1	15 minute ramp to 100 °C
2	15 minute soak at 100°C
3	15 minute ramp to 150°C
4	15 minute soak at 150°C
5	60 minute ramp to 250°C
6	60 minute soak at 250°C
7	Cool to <150°C

Table 7. Reactive Ion Etching (RIE) parameters for BCB etching.

Parameters	cyclotene.pre
O ₂ (sccm)	10
He (sccm)	-
CF ₄ (sccm)	5
Pressure (mTorr)	50
RF power (W)	100
Etching rate (nm/min)	150

2.4.7. Negative lithography for p-side contact

The negative lithography has to be done to open windows required for metal deposition.

Figure 2-5 shows the features for negative lithography in green. The step are summarized below:

1. Spin-coat the NR7-1000PY @ 4000 rpm for 40 seconds
2. Pre-bake @ 150 °C for 1 min
3. UV Exposure @ 12 mW for 14 seconds
4. Post-bake @ 100 °C for 1 min
5. Develop in RD6 for ~ 20 seconds

6. Run recipe “Descum.prc” on PECVD for 2 min. This is to remove any remaining thin layer of photoresists.
7. Deoxidize the waveguide by dipping the sample into $\text{H}_3\text{PO}_4\text{:H}_2\text{O}$ (1:30) acid solution for 7-8 seconds. The sample dipped in DI water and rinsed for 1 min and dried with N_2 .

2.4.8. Contact metallization, liftoff and contact annealing

The sample is loaded into an Edwards’s thermal evaporation machine right after the deoxidization step to avoid any excessive surface oxide formation. The machine would be ready for deposition when the chamber pressure reaches to 2×10^{-6} mTorr. Deposition started with 5 nm of Titanium (Ti) which provides excellent adhesion between the sample and the gold layer. This is very critical as without doing this the gold layer would peel off easily from the surface of the sample. Ti deposition is followed by deposition of 300 nm of gold which provides the device contact.

After metallization the sample is soaked into the RR2 @ 60°C for liftoff. RR2 is a specific stripper for the NR7-1000PY photoresist. The metals from unwanted area starts to peeling off from the sample and the total time is about 20 minutes. The sample then rinsed with acetone, methanol, isopropanol and DI water and then dried with N_2 .

The sample is annealed using a RTP-600 Modular Process Technology thermal annealer in a N_2 ambient. The recipe profile used is shown in Table 9 in appendix A. The contacts are annealed at the temperature of 430 °C for 30 seconds.

Figure 2-8 shows an image taken using a microscope from a 2 mm Fabry-Perot laser after annealing contacts.



Figure 2-8. Top view image of the fabricated 2 mm Fabry-Perot laser device after p-contact annealing

2.4.9. Substrate lapping and polishing

The 630 μm thick InP substrate has to be thinned down to about 100 μm . This is to improve the heat conductivity and be able to maintain the temperature of the junction using thermo-electric cooler (TEC). The thinner the substrate the closer the junction would be to the TEC. Also in order to cleave the laser bar with the accuracy of about $\sim 5 \mu\text{m}$ the substrate has to be polished to about a 100 μm . The sample attached to a thin glass slide using wax and then transferred to the polishing chuck. First the sample thinned down to about 100 μm using a slurry of 5 μm size aluminum oxide grit and water. Lapping followed by polishing the sample using 0.3 μm size aluminum oxide powder. After this the substrate should look shiny. The sample then dipped in acetone solution for hours to remove the wax and then rinsed with acetone, methanol, and isopropanol and finally dried with N_2 .

2.4.10. N-contact metallization

Before metallization, deoxidization has been done by dipping the sample into $\text{H}_3\text{PO}_4:\text{H}_2\text{O}$ (1:30) acid solution for 7-8 seconds. The sample dipped in DI water and rinsed for 1 min and dried with N_2 .

2 nm of Nickel (Ni), 20 nm of germanium (Ge) and 200 nm of gold (Au) are deposited respectively. The first deposited layer, Ni, provides adhesion to the surface. Ge will diffuse to the substrate during the annealing and would create a degenerately doped n-type region. The sampled then annealed at 430 °C for 30 seconds.

2.4.11. Device image

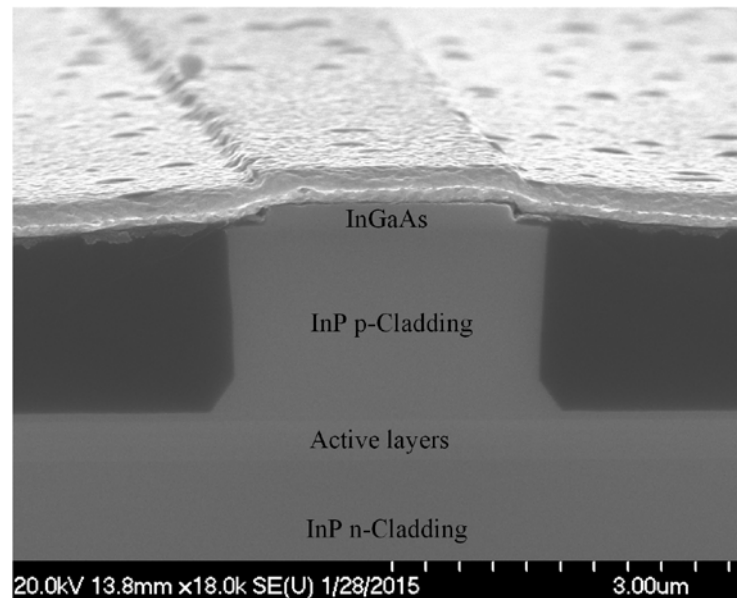


Figure 2-9. Scanning electron microscopy (SEM) image from a cleaved facet of the laser

2.4.12. Cleaving, mounting and temperature controlling

The sample cleaved into individual chips using diamond tip scriber mounted with 45°degrees of angle on a precise XYZ micrometer. This gives us the ability to be able to cleave with the accuracy of 5 μm . A special cleaving tape is used to hold the sample and then it is pushed against a surgery knife to cleave the sample.

The individual laser chips are mounted p-side up on the gold-coated copper studs with the same length as of the chip (here was $\sim 2\text{ mm}$) using standard Pb-In solders. In order to connect the laser to external drive circuitry for carrier injection, the laser p-contact is connected to a ceramic standoff (soldered to the copper stud) using a fine gold wire.

In order prevent overheating and also promoting the stability of the gain medium, working temperature of the diode is controlled. This has been done using a 10 k Ω thermistor which is mounted on the copper stud close to the chip for temperature sensing and a closed loop circuit controlling the amount of the current going to the TEC cooling pad (which is in direct contact with the copper stud). Here a precision PID controller has been used to maintain the working temperature of the device with the accuracy of 0.001 °C. In most cases this temperature is chosen to be 20 °C which is just below the room temperature and this is to avoid any condensation of the device facets.

3. DIRECT RF MODULATION OF ALGAINAS MODE-LOCKED LASER

3.1. Introduction

Monolithic high-repetition-rate lasers have drawn considerable attention for applications in photonic analog-to-digital conversion, clock recovery and arbitrary waveform generation [50-52]. These compact and monolithic sources generate sub-picosecond pulses at high repetition rates but exhibit large timing jitter due to amplified spontaneous emission (ASE) and lack of external stabilization. In order to realize a low noise mode-locked laser (MLL) by synchronizing to an external clock at high frequencies (> 20 GHz), several methods such as sub-harmonic hybrid mode-locking (SHML) [53], fundamental hybrid mode-locking (FHML) using semi-insulating substrate [54] and optical synchronous mode-locking [55] have been presented. The first of the above methods overcomes the shallow radio frequency (RF) modulation issue at high frequencies but introduces unwanted amplitude modulation and excess timing jitter (Figure 3-1 (a)). The second requires a semi-insulating wafer and lengthy fabrication process (Figure 3-1 (b)) while the third typically involves injection of a low noise mode-locked laser into the laser cavity, requiring an additional laser (Figure 3-1 (c)).

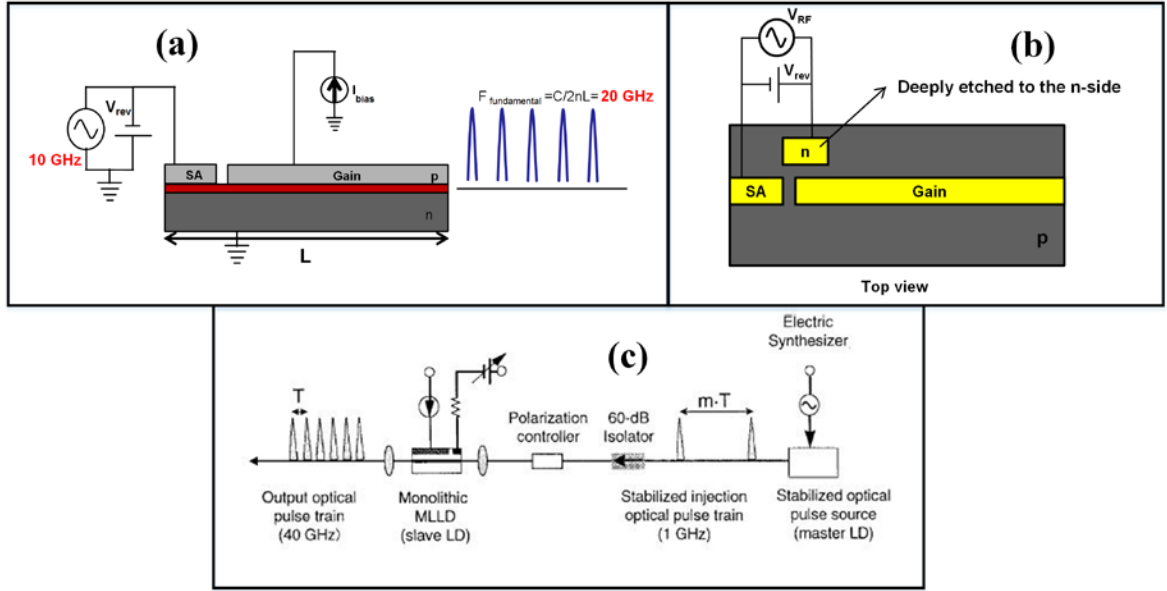


Figure 3-1. (a) Sub-harmonic hybrid mode-locking scheme, (b) fundamental hybrid mode-locking (FHML) using semi-insulating substrate and (c) optical synchronous mode-locking [55]

A promising new AlGaInAs-InP strained quantum well material at 1.55- μm described in chapter 2 used here to fabricate MLLs [56]. This material system is beginning to replace conventional InGaAsP-InP materials owing to a larger conduction band discontinuity ($\Delta E_c = 0.72 \Delta E_g$) and a smaller valence band discontinuity. The former enables uncooled operation over a large dc bias range and the latter enables a large range of reverse bias voltage, allowing for shorter pulses durations [35, 56].

In this chapter, we present 860 fs pulses from a monolithic AlGaInAs multiple quantum well two-section MLL fabricated by employing a very simple self-aligned wet etching technique that described in chapter 2. By using Benzocyclobutene (BCB) as the isolation layer (1.3- μm -thick) and minimizing the metal pad size, we were able to modulate the SA at 22 GHz and

synchronize the laser to an external source. By doing so we achieved very effective FHML (280 fs timing jitter) which shows distinct advantages over other methods.

3.2. Device structure and fabrication

Figure 3-2 shows the design layout of a 2 mm two-section mode-locked laser. The 2.5 μm waveguide is shown in blue and it is overlapped intentionally with metal pads (in green). Cleaving marks are put in the design to be able to cleave the saturable absorber with desired length. Different cleaving marks are introduced in the design to achieve different length ratios between the gain and SA section (1% to 6%). Other features are serving as alignments and cleaving marks.

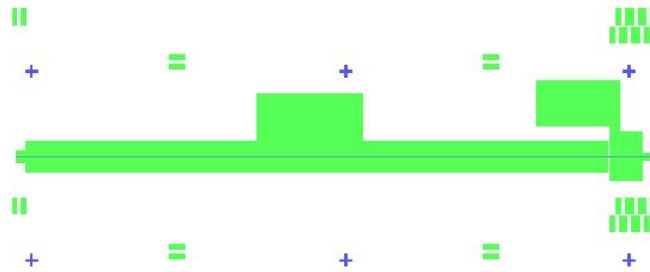


Figure 3-2. Image of the two-section mode-locked laser design from L-Edit software showing waveguides and alignment marks in blue and metal pads, alignment marks and cleaving marks in green.

The electrical isolation between the gain section and SA section is achieved by removing the first two heavily-doped layers (InGaAs and InGaAsP) by $\text{H}_2\text{SO}_4:\text{H}_2\text{O}_2:\text{H}_2\text{O}$ wet etchant. This

provides us with a 3 k Ω resistance for the 10- μ m gap. Figure 3-3 shows the actual image of the fabricated 2 mm device before cleaving.



Figure 3-3. Top view image of the fabricated 2 mm two-section mode-locked laser

The laser bar is cleaved to a total length of 1912 μ m with a 56 μ m SA. Figure 3-4 shows the waveguide structure and the contact layout. The facets are left uncoated and the laser is mounted with the epi layer up on a copper stud connected to a thermo-electric cooler (TEC) to maintain the temperature at 20°C.

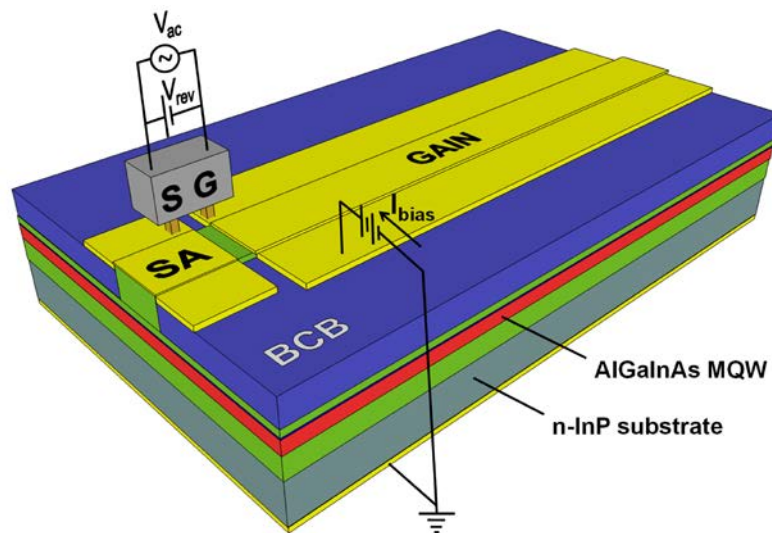


Figure 3-4. Device schematic showing the waveguide structure and contact layout.

3.3. Experimental results

Passive mode-locking is achieved by forward biasing the gain section using a simple dc probe and by reverse biasing the SA. With the help of an 18 GHz bias tee and a 40 GHz ground-signal (GS) microwave coplanar probe, the reverse bias voltage and the RF signal are mixed and applied to the device. Here the signal and ground probes were connected to the SA and the gain section, respectively as shown in Figure 3-4. Figure 3-5 shows the contacts layout schematic and electrical connections to provide a better understanding of how each section are biased and how the dc reverse bias and ac signals are mixed and applied to SA section. As shown in the schematic, the bias current on the gain section is applied between the p-electrode (top) and the n-electrode (bottom). Also the negative port of the reverse bias DC signal and the positive port of the AC signal (RF) is applied to the SA p-section (top) and the positive port of the reverse bias DC signal and the negative port of the AC signal (RF) is applied to the Gain p-section (top) using a bias tee. By doing that the p-section of the gain section is acting as a floating ground for the SA. Of course the SA is forward biased until the amount of voltage on the reverse bias voltage supply is less or equal to the forward biasing voltages on the gain section. However, by increasing the voltage beyond that point, the SA will be reverse biased and the dropped voltage (which is negative) on the SA will be the difference between the SA supply voltage and the forward bias voltage of the gain section.

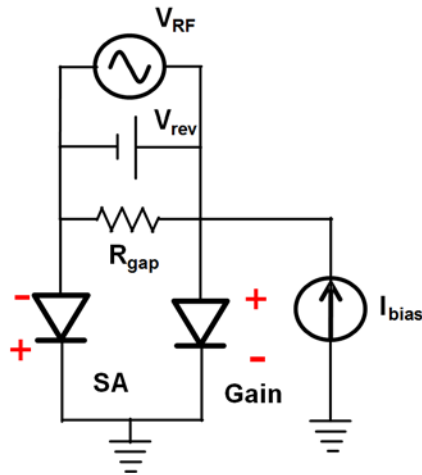


Figure 3-5. Contacts layout schematic and electrical connections of the hybridly mode-locked two-section laser

Figure 3-6 (a) shows a typical I-V curve of this mode-locked laser. From this graph a device impedance of 2.7Ω has been obtained. Figure 3-6 (b) shows the typical output power-current (L-I) characteristics for different reverse bias SA voltages. From this data a threshold current of 57 mA is obtained for the unbiased SA, and it increases as the reverse bias voltage is increases. Also a slop efficiency of 0.08 W/A is measured when SA in unbiased.

Figure 3-7 shows the far field mode pattern of the mode-locked laser in two directions when the gain section is biased with 70 mA of current and when the SA is unbiased. From this data an ellipticity of 0.89 is achieved. This suggest a good coupling ratio when trying to couple the light to a SMA fiber as it is easier to match the laser mode (almost circular) to a circular mode of the fiber.

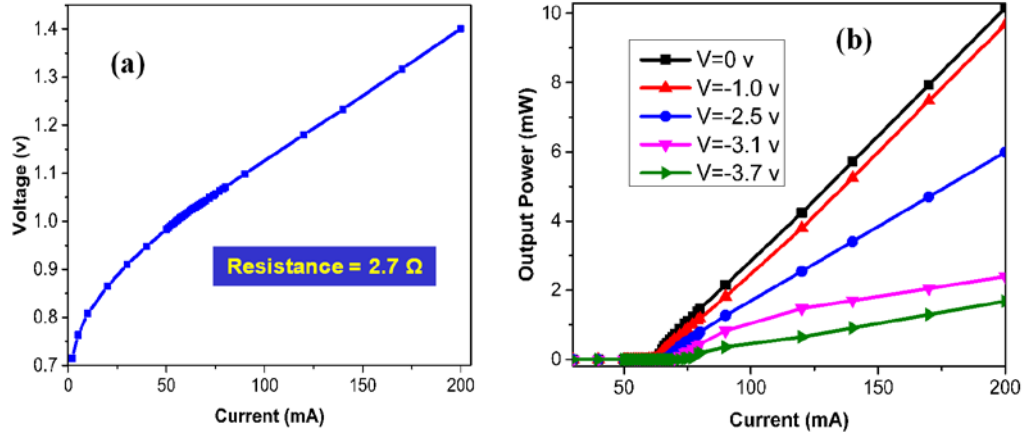


Figure 3-6. (a) Current vs voltage characteristics of the two-section MLL, and (b) output power-current characterization of the two-section MLL at 20°C for different reverse bias voltages

Figure 3-8 shows the experimental setup that has been used for hybrid mode-locking and diagnostics. Output light is coupled to a single mode fiber using an aspheric lens and a free space isolator is used to avoid any back reflection. A fiberized optical semiconductor amplifier is also used to amplify the output light.

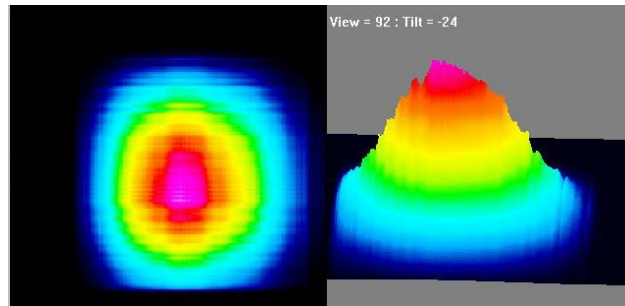


Figure 3-7. Far field mode pattern of the mode-locked laser measured using DataRay Inc. beam profilometer

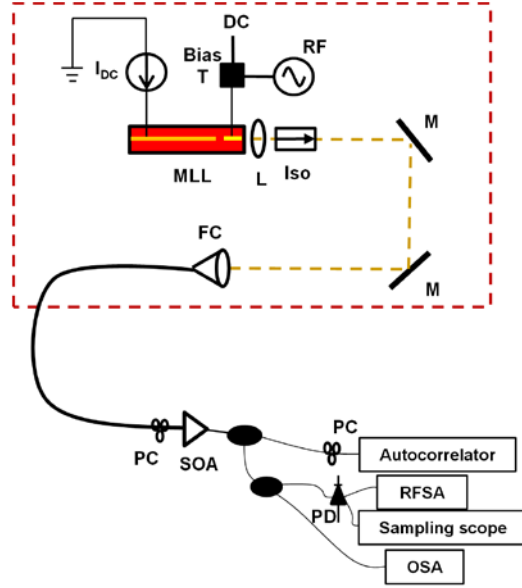


Figure 3-8. Experimental setup used for hybrid mode-locking and diagnostics. Iso: isolator; SOA: semiconductor optical amplifier; PD: photodetector; PC: polarization controller; RFSA: radio frequency spectrum analyzer; OSA: optical spectrum analyzer; L: aspheric lens; FC: fiber coupler.

Stable passive mode-locking is observed for bias current values of 75 mA to 140 mA with reverse bias voltages of -2 V to -3.9 V. Figure 3-9 (a) shows the optical spectrum of the passively MLL running at 123 mA and reverse bias voltage of -3.9 V which gave us the shortest optical pulse. The optical spectrum centered at 1548 nm has a 3-dB bandwidth of 9.8 nm. Figure 3-9 (b) shows the corresponding RF spectrum at 22.14 GHz and its harmonic detected by a 33 GHz fast InGaAs PIN photodetector and observed by a 50 GHz RF spectrum analyzer. Maintaining a constant temperature, the pulse repetition rate can be tuned by about 400 MHz by changing the

biasing current and the reverse bias voltage. Figure 3-10 shows the optical intensity autocorrelation of the isolated pulse obtained by the second-harmonic autocorrelator. The autocorrelation signal of the pulse is equal to 1.31 ps which deconvolves to 860 fs by using 0.656 as the deconvolving factor obtained from simulation. The simulation is done using the measured optical power spectrum and assuming flat spectral phase. The results imply a time-bandwidth product of 1.05 which is 2.6 times transform-limited [57].

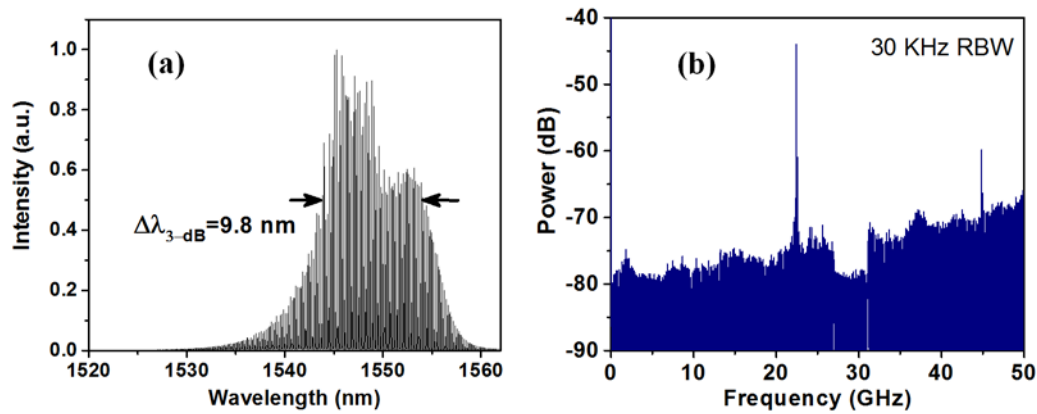


Figure 3-9. (a) Optical spectrum of the mode-locked laser for shortest pulse at $I_{\text{gain}} = 123 \text{ mA}$ and $V_{\text{abs}} = -3.9 \text{ V}$, (b) the corresponding RF spectrum

We minimized the capacitance by reducing the size of the SA metal pad to $56 \mu\text{m} \times 100 \mu\text{m}$. By having the $1.3\text{-}\mu\text{m}$ -thick BCB layer as an insulating layer further helped to reduce the capacitance of SA pad. Careful design of these parameters enabled us to drive the SA at very high frequencies ($>20 \text{ GHz}$) very effectively without the need for semi-insulating substrate wafers that require more fabrication processes [54].

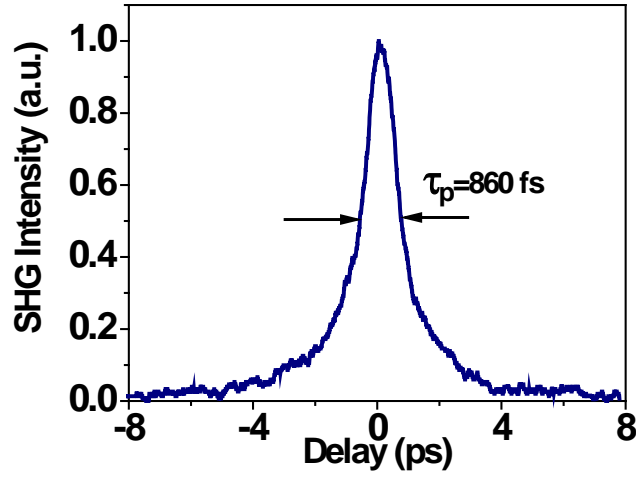


Figure 3-10. Autocorrelation trace of the isolated pulse under passive mode-locking

Hybrid mode-locking is achieved by using a low noise RF synthesizer (Agilent E8254A) to drive the two-section MLL. SMA cables are used to transmit the RF signal and a 20-dB RF amplifier is used to compensate the huge loss of these cables and the losses introduced by the 18 GHz bandwidth bias tee and other connectors. Figure 3-11 shows the double side band noise spectrum for the device running in the passive and fundamental hybrid and sub-harmonic hybrid mode-locked ($n=2$) regimes respectively. The bias current and the reverse bias voltage are 80 mA and -3.1 V respectively. The applied RF is tuned to 22.417783 GHz to minimize the pedestal. On applying the RF signal, the RF tone linewidth is seen to decrease from 1.5 MHz to sub Hz. As seen in Figure 3-11, by increasing the RF power, the RF noise is drastically reduced (more than 20 dB decrease is observed by applying 15 dBm RF signal). Figure 3-11 (inset) shows the amplified laser output time domain traces with 44.6 ps period using a 50 GHz Agilent sampling scope triggered

by 1.868148583 GHz signal using another RF synthesizer. The RF synthesizers and RF spectrum analyzer used are synchronized to each other. Because of the frequency response of the photodetector and cables, only the first harmonic is observed. For comparison SHML was also performed on the device with 15 dBm RF power and by small tuning of the modulation frequency to have the minimum pedestal. As can be seen in Figure 3-11, SHML has much higher RF noise validating the effectiveness of our approach.

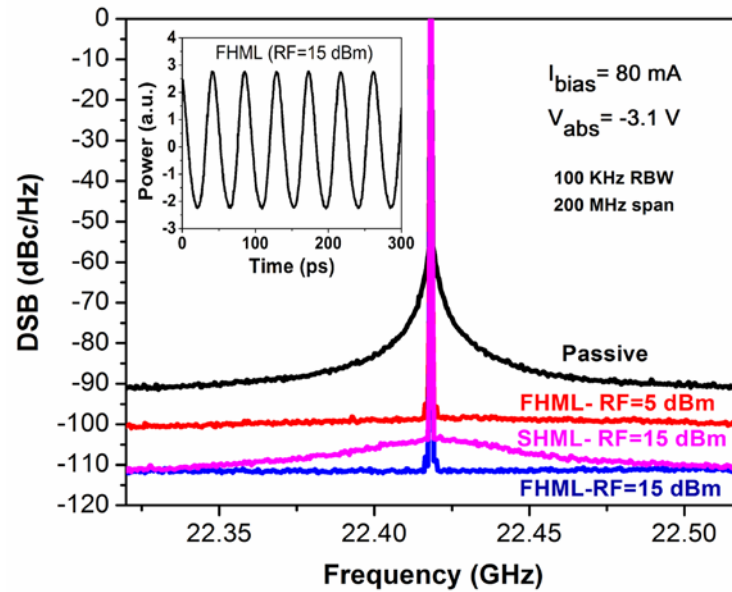


Figure 3-11. Double side band noise spectrum for passive, FHML at different RF power and SHML ($n = 2$). Inset shows the sampling scope trace for the FHML at RF power of 15 dBm.

Figure 3-12 shows the residual phase noise power spectral density of the mode-locked laser under 15 dBm RF power, along with the noise floor of the measurement system, measured by a HP 70420A carrier noise test set and normalized to a 1 Hz Resolution bandwidth. From this data the timing jitter for the 1 Hz- 100 MHz range is calculated to be 280 fs.

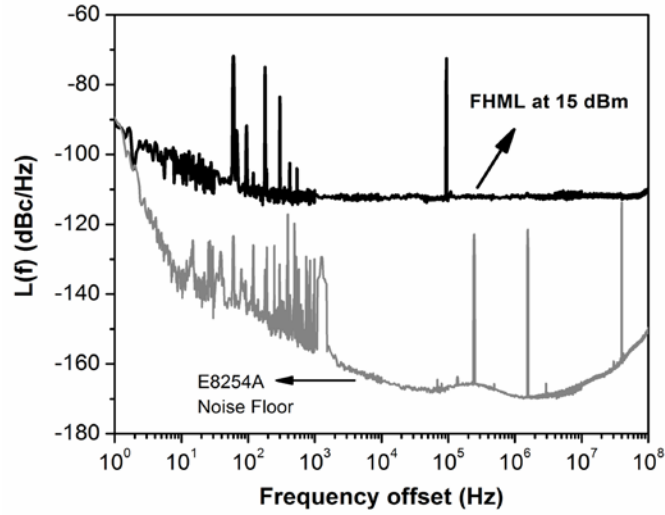


Figure 3-12. Residual phase noise power spectral density of the FHML laser (black) under $I_{\text{gain}} = 80 \text{ mA}$ and $V_{\text{abs}} = -3.1 \text{ V}$ and the RF power of 15 dBm and noise floor of the measurement (Grey).

3.4. Noise performance comparison

The timing jitter for the device under FHML is calculated by integrating the residual phase noise data obtained from the carrier noise test set which takes advantage of the fact that the device and the RF reference are phase-locked for phase noise measurement. However this phase noise measurement requires an appropriate RF source to be used as the reference. Key features of this source are that; 1) it has the same nominal frequency as the device under test (DUT), 2) it has lower phase noise than the DUT, and 3) additionally this reference signal should be phase-locked to the DUT such that it remains in quadrature with the DUT during the measurement.

For the FHML case, the laser is at the same frequency of the reference so keeping them in quadrature is easy to achieve and the phase noise could be measured. However for passive MLL this requirement of being in quadrature is hard to achieve because the passively mode-locked laser is free-running. Also for SHML, since the reference and the laser are at different frequencies, this method would require adding a frequency divider or multiplier which adds extra phase noise to the measurement and makes the phase noise measurement difficult.

The RF spectrum of the photo-detected mode-locked laser pulse train can be used for noise comparison but this side band noise is composed of both AM and PM noise components and thus we cannot quote this integrated noise as “jitter”. So just for comparison and to show an improvement with the novel design, instead of giving any jitter values (not accurately measured in case of passive MLL), we have shown 20 dB improvement in the RF noise of the passive MLL by looking just at the RF spectrum after hybrid mode-locking it.

The single side band noise measured by RFSA for the device running under passive ML, SHML and FHML are shown on Figure 3-13 as well as the residual phase noise for the FHML as measured by the carrier noise test set. By using the SSB noise as the residual phase noise plot and by integrating, the below values are obtained for the “Integrated noise” (4 MHz-100 MHz).

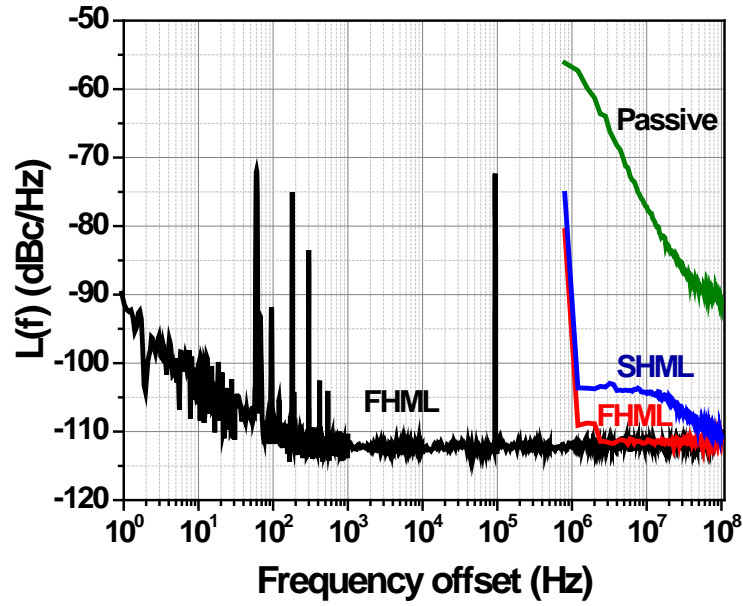


Figure 3-13. Single side band noise measured by RFSA for the device running under passive ML (green), SHML (blue) and FHML (red). Residual phase for the FHML (black) is also shown for reference (measured using the carrier noise test set)

Table 8. Integrated single sideband noise from 4 MHz to 100 MHz of the device running under different mode-locking scheme

Mode-locking mechanism	Integrated noise
<i>FHML</i>	270 fs
<i>SHML</i>	410 fs
<i>Passive ML</i>	7.32 ps

3.5. Conclusion

In this chapter we demonstrated a simple self-aligned wet etching process to fabricate AlGaInAs quantum well MLLs. This material system has shown distinct advantages compared to the conventional InGaAsP-InP system. Pulses of 860 fs were obtained at a high repetition rate of 22 GHz. By carefully designing the metal pads, and by having 1.3- μm -thick layer of BCB as the insulation layer, very effective RF modulation of the SA was made possible at the round-trip of the cavity. Low timing jitter of 280 fs (1 Hz-100 MHz) at the fundamental repetition rate was achieved. These results confirm the potential of the novel, simple and cost-effective laser design as a compact source of low noise high repetition rate optical pulses.

4. TRUE LINEARIZED INTENSITY MODULATOR FOR PULSED LIGHT

4.1. Introduction

Recently as described in section 1.6, a linearized optical intensity modulator has been reported [34]. The linearity of this modulator is inherent in its design and potentially could provide a much higher SFDR without the need for any linearization technique. It employs an injection-locked resonant cavity placed in one of the arms of the MZI. When the frequency of the input light (master laser) is inside the locking range of the resonant cavity (slave laser), its frequency locks to the master laser frequency. Based on Adler's equation [28] the induced phase response of the injection-locked slave laser is an arcsine function of the detuning between the resonance frequency of the slave laser and frequency of the master laser,

$$\varphi_L = \arcsin\left(\frac{\Delta\omega}{\Delta\omega_L}\right) \quad (4-1)$$

where $\Delta\omega$ is frequency detuning between master and slave laser and $\Delta\omega_L$ is half of the locking range of the slave laser. This equation is the steady state solution of the Adler's equation under weak injection-locking.

Previously this modulator concept was implemented using a vertical cavity surface emitting laser (VCSEL) and was shown to provide a very low V_π of 2.6 mV, possible gain, modulation bandwidth of 5 GHz and most importantly SFDR of 120 dB.Hz^{2/3} [34, 58]. However,

the above modulator design is limited to single frequency light and to adapt this technique to a pulsed light, a resonant cavity with multiple optical resonances is needed (Figure 4-1 (a)). This can be done by using a Fabry-Pérot laser (FPL) as the resonant cavity with multiple resonances and injection-locking them to the frequency comb of the master laser [59]. By modulating the slave laser and inducing an arcsine phase response on each of the injected seeds and by combining them with its unmodulated counterpart from the other arm of the MZI, a linearized intensity modulator for pulsed light can be realized (Figure 4-1 (a), (b)).

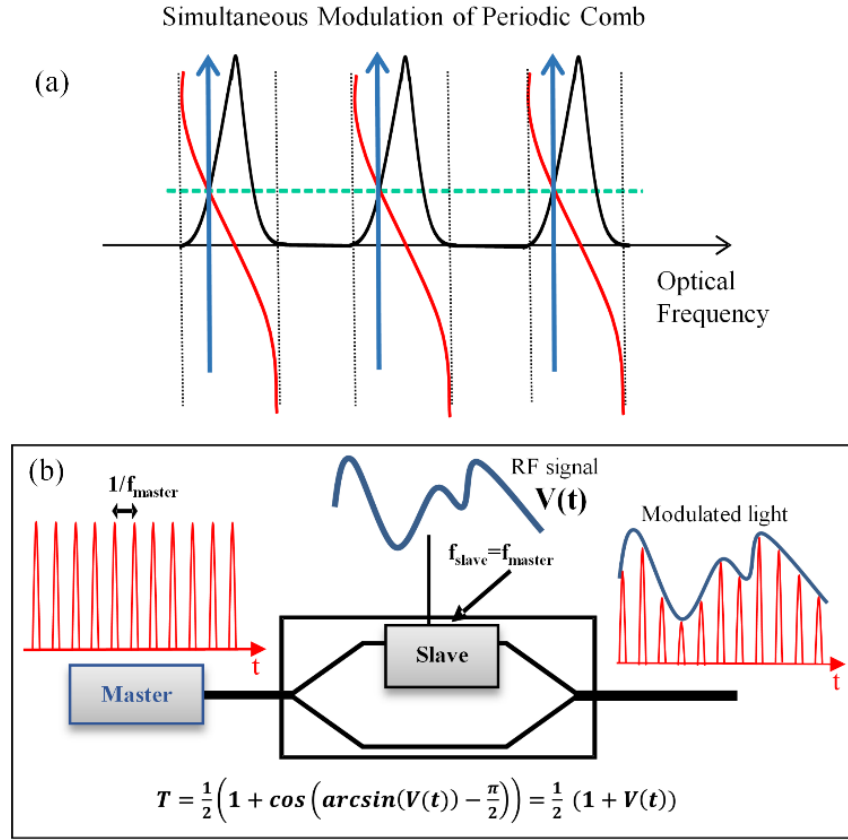


Figure 4-1. (a) Schematic showing the slave laser resonances (black), the corresponding phase response (red), injected comb lines from the MLL (blue) and the instantaneous imparted phase on each of the injected comb lines (green), (b) Schematic of the linear interferometric intensity modulator for pulsed light. f_{master} and f_{slave} denote the mode spacing of the master and slave laser, respectively.

For injection-locking, there should be an optical spectrum overlap between the lasers and also the free spectral range (FSR) of the FPL should match the pulse repetition rate of the MLL.

These conditions could possibly be satisfied if both the MLL laser and the FPL chips are fabricated using the same wafer with the same waveguide structure. However there are two main challenges: (1) two different physical lengths of the lasers are needed ($\sim 5\text{-}10\text{ }\mu\text{m}$ difference) to compensate for the slight difference in group indices of the FPL and MLL, requiring very accurate device cleaving; (2) because of the dispersion, the optical mode spacing of the FPL is not constant across the spectrum and this makes the injection-locking to all of the equally-spaced optical modes of the MLL more challenging [59]. This is highlighted in the optical spectra of the MLL (cavity length of $1912\text{ }\mu\text{m}$) and FPL (cavity length of $1950\text{ }\mu\text{m}$), shown in Figure 4-2 (a-c). The optical modes of the two lasers match well at one end of the spectrum (Figure 4-2 (b)) and start to walk off from each other on moving to the other side of the spectrum (Figure 4-2 (c)). This results in overall poor injection-locking and no induced phase response on the injection-locked resonant cavity.

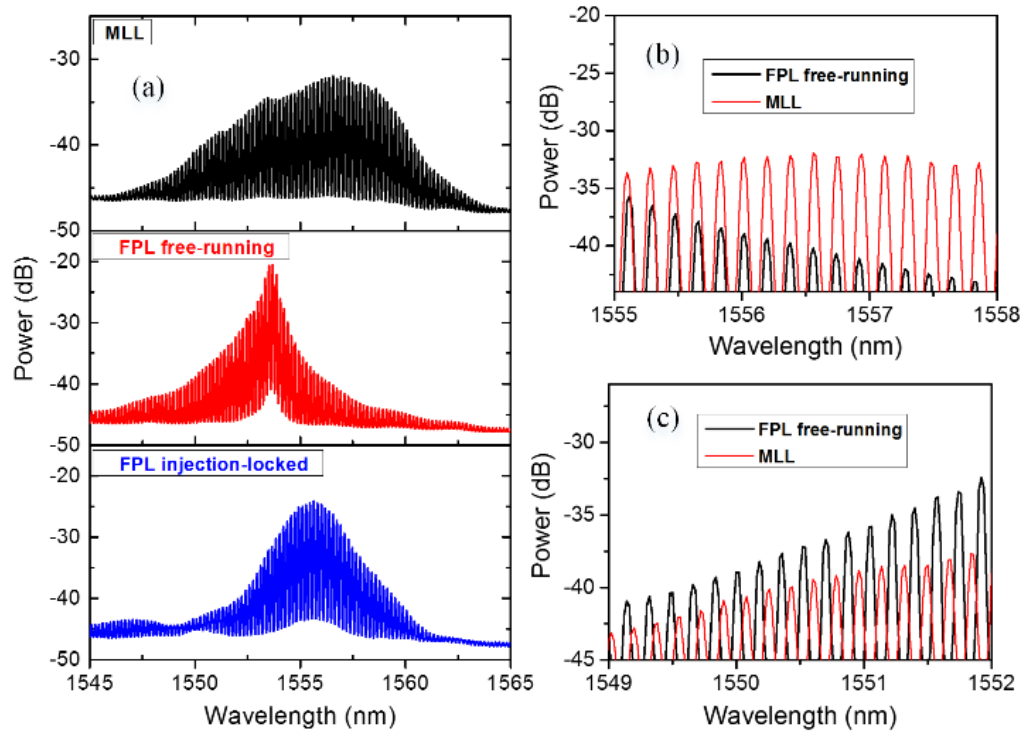


Figure 4-2. (a) Optical spectra of the passively MLL (black) and FPL as the resonant cavity before (red) and after (blue) injection-locking. Both the lasers are biased with different dc currents to match the frequency spacing between the modes which results in different spectrum widths. The injection-locked FPL spectrum is much narrower than the spectrum of the master MLL since the well-spaced modes of the MLL match at one end of the spectrum with the modes of the FPL as shown in (b) and start to walk off from each other on moving to the other side of the spectrum (c).

Figure 4-3 (a) also shows the RF spectrum of the hybridly mode-locked laser running at temperature of 17 °C and bias current of 145 mA and saturable absorber voltage of -2.8V. Figure 4-3 (b) shows the RF spectra of the FPL running at temperature of 23 °C and biased with

58 mA of current before (red) and after (blue) injection-locking. Autocorrelation trace of an isolated pulse from the FPL after injection-locking is also shown in Figure 4-3 (c). This is also another proof that the FPL is injection-locked to the MLL.

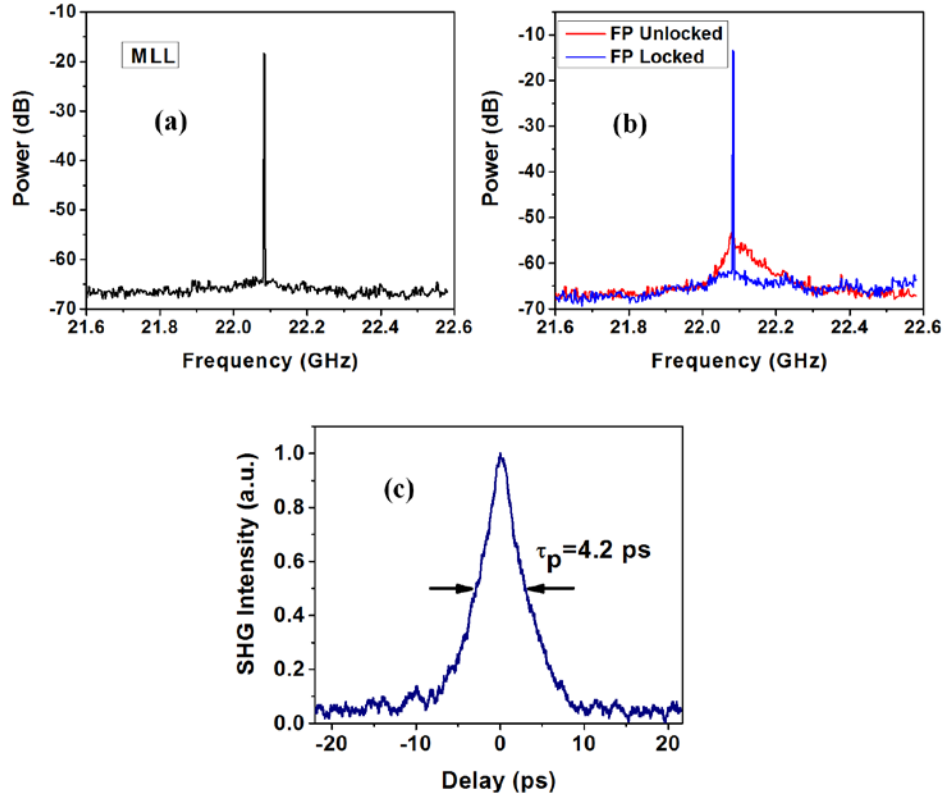


Figure 4-3. (a) RF spectrum of the hybridly MLL running at temperature of 17 °C, biased with 145 mA and $V_{SA} = -2.8$ V, (b) RF spectra of the FPL running at temperature of 23 °C and biased with 58 mA before (red) and after (blue) injection-locking and (c) autocorrelation trace of an isolated pulse from the FPL after injection-locking.

In this chapter, we propose and demonstrate the use of a MLL identical to the master laser as the resonant cavity inside the MZI [60]. This ensures the optical spectrum overlap and ideal matching of the spacing between the optical modes of the lasers. Experimental results of the injection-locking of this laser are presented here. The static phase response of the linearized modulator is presented for different injection power ratios. Instead of just modulating the current on the gain section of the FPL, the use of the MLL as the slave laser gives us two parameters to modulate: the saturable absorber voltage and the current on the gain section. Modulating the current of the gain section leads to carrier density modulation and hence an unwanted amplitude modulation is introduced. However we believe this could be reduced significantly by modulating the SA instead. Experimental results for the signal to intermodulation ratios are presented here and a much reduced third-order intermodulation tone is observed (for the same fundamental RF power) when modulating the SA compared to modulating the gain. Finally the SFDR of this modulator is measured for each of the two above cases.

4.2. Injection-locking of a passively MLL (slave) by a hybridly MLL (master)

A promising AlGaInAs-InP material system (as described in section 2.1) has been used to fabricate the MLL chips. The multiple quantum well structures have been grown on sulfur-doped InP substrate using metal organic vapor phase epitaxy (MOVPE). The active region consists of five compressively strained wells (6 nm thick) and six slightly tensile strained barriers (10 nm

thick). Single mode $2.5\text{ }\mu\text{m}$ waveguides are fabricated using standard UV positive lithography process. Fabrication process is the same as description given in section 2.4. The master and slave lasers are chosen to be the adjacent lasers on a laser bar and cleaved simultaneously to obtain the exact same lengths. The total length of the lasers is $1.868\text{ }\mu\text{m}$ with the SA length of $70\text{ }\mu\text{m}$. The ratio of the SA to gain section length is chosen in such a way that the relaxation oscillations are minimum and the mode-locking quality is the best possible. The facets are left uncoated and the devices are mounted p-side up on gold coated copper studs which themselves sit on top of thermoelectric coolers (TEC). The TEC currents are controlled using high precision proportional-integrated-differential (PID) controllers with a stability of 0.001°C . This is very critical for stable injection-locking since even a 0.001°C change results in a $\sim 15\text{ MHz}$ drift in the optical frequency and a subsequent change in the quadrature point of the MZI. Figure 4-4 shows the electrical and optical characteristics of the MLL when no voltage is applied to the SA. A top view picture of the device is also shown in the inset of Figure 4-4. A threshold current of 51 mA , device impedance of $3.7\text{ }\Omega$ and slope efficiency of 0.077 W/A are measured from these data.

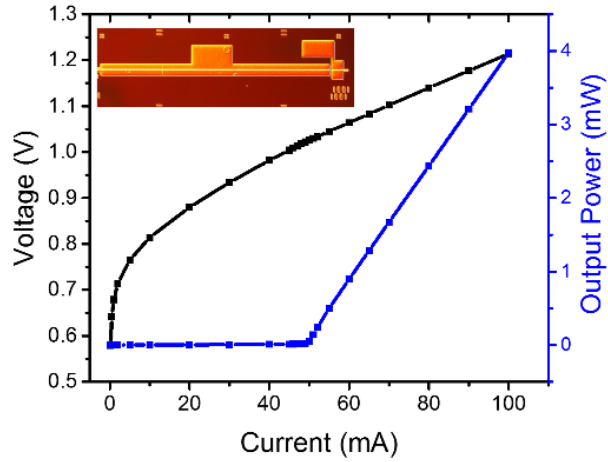


Figure 4-4. Typical output power-current (blue) and voltage-current (black) characteristics of the MLL operating at 20 °C. No voltage is applied to the SA. The device characteristics are: $I_{\text{threshold}}=51$ mA, $R=3.7$ Ω and slope efficiency of 0.077 W/A. Inset shows the top view of the actual fabricated MLL.

The master laser is hybridly mode-locked by forward biasing the gain section using a simple DC probe and modulating the reverse-biased SA section. A high speed bias-tee is used to combine the reverse bias voltage and the RF signal. The mixed signal is applied to the SA using a 40 GHz ground-signal (GS) microwave coplanar probe. The slave laser is passively mode-locked by forward biasing the gain section and reverse biasing the SA section. Bias-tees are used for gain and SA sections to be able to apply the AC signal and modulate them separately. Aspheric lenses are used to couple the light in and out of the lasers. The master laser beam is divided using a non-polarizing beam splitter (BS). An optical isolator with more than 35 dB isolation is used to avoid

any reflection being coupled back to the master laser. The injection power is adjusted using a neutral density filter (NDF) and monitored at the same time with the help of a pellicle beam splitter and an optical power meter. The injecting facet is the gain section facet of the slave laser. The output light from the slave is coupled to an SMF fiber and amplified using a semiconductor optical amplifier before going to diagnostics.

Figure 4-5 (a)-(c) show the optical spectra of the master and slave laser before and after injection-locking. Here the master laser is operating at 65 mA of bias current and a reverse bias voltage of -1.8 V and is maintained at a constant temperature of 20 °C. An RF power of 6 dBm at 22.998 GHz is applied to the SA to achieve hybrid mode-locking of the laser. The slave laser is passively mode-locked with 65 mA of bias current and a reverse bias voltage of -1.9 V and the operating temperature of 19.100 °C. Both lasers are running at the same bias currents and the same SA reverse bias voltages to achieve the same spectral width. SA voltages are carefully chosen to match the repetition rate frequencies and the operating temperature of the slave laser is carefully tuned for a precise overlap of its optical modes with that of the master laser. A high resolution optical spectrum analyzer is used to monitor the optical modes in more detail. The power injection ratio is -27.8 dB and is chosen to achieve the best injection-locking with the least amount of relaxation oscillations. The measured 3-dB optical bandwidth is about 2 nm for both lasers. Figure 4-5 (d) shows the corresponding RF spectra and confirms that the passively mode-locked slave laser follows the hybridly mode-locked master laser. The autocorrelation trace of the pulses from master laser are shown in Figure 4-5 (e). The pulse width is measured to be ~5 ps assuming a Gaussian shape and the pulses are 2.8 times transform limit. The autocorrelation trace of the slave laser is not shown here since it is almost identical to that of the master laser.

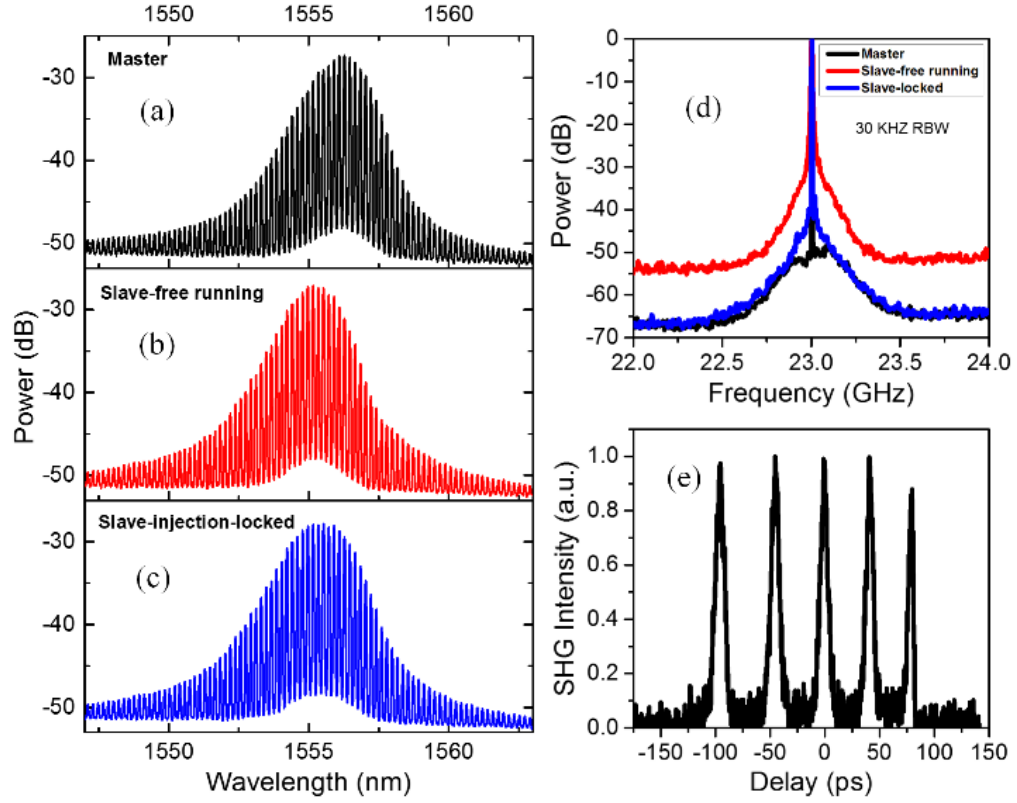


Figure 4-5. (a) Optical spectrum of the master laser (black) with $I_{\text{gain}}=65$ mA, $V_{\text{SA}}=-1.8$ V, $T=20$ °C and 6 dBm of RF power at 22.998 GHz (b) and (c) optical spectra of the slave laser before (red) and after (blue) injection-locking with $I_{\text{gain}}=65$ mA, $V_{\text{SA}}=-1.9$ V, $T=19.100$ °C and injection ratio of -27.8 dB. (d) Normalized RF spectra of the master laser and slave laser before and after injection-locking. (e) Autocorrelation trace of the master laser (slave laser trace is not shown since it is same as that of the master laser with similar pulse width)

4.3. Experimental setup of the linearized intensity modulator for pulsed light

A schematic of the experimental setup is shown in Figure 4-6. Free space optical delays are used in both the arms of the MZI to be able to match the path lengths to achieve same pulse overlap after splitting. PZT linear optical stage is used in one of the optical delays to fine-tune the path difference and bias the MZI at quadrature. Power is monitored at three places in the setup: the injected power to the slave laser, the free space power in each of the arms of the interferometer, and the optical power coupled to the fiber from each of the arms. The last two power meters and a neutral density filter placed in front of the slave laser are used to monitor and balance the optical power of each arms and help to increase the visibility of the MZI. With the help of half-wave plates, the polarization of each arm is adjusted to further increase the visibility to $\sim 68\%$. Normalized change of the output power (static phase shift response) of the modulator for the power injection ratio of -27.8 dB is obtained by deviating the current of the slave laser around the bias point and monitoring the output power of the MZI (Figure 4-7 (a)). Static phase shift of π is achieved when the bias current of the slave laser is changed by approximately 2.3 mA. This corresponds to a full locking-bandwidth of 665 MHz. The effective V_π is calculated to be 8.5 mV. The static phase shift response in the locking range deviates from the expected pure linear response because of the significant amount of PM-to-AM coupling created by modulating the current of the slave laser. The -27.8 dB power injection ratio is chosen to avoid relaxation oscillations which are

the byproducts of the injection-locking. Increasing the injection ratio, one could possibly increase the visibility of the interferometer, however this itself creates relaxation oscillations and compromises the visibility of the interferometer. Figure 4-7 (b) shows the static phase response of the modulator for three different injection ratios. An increase in the injection-locking bandwidth is expected as the injection ratio increases. However by further increasing the injection ratio (-16 dBm), relaxation oscillations become dominant and the injection-locking becomes unstable.

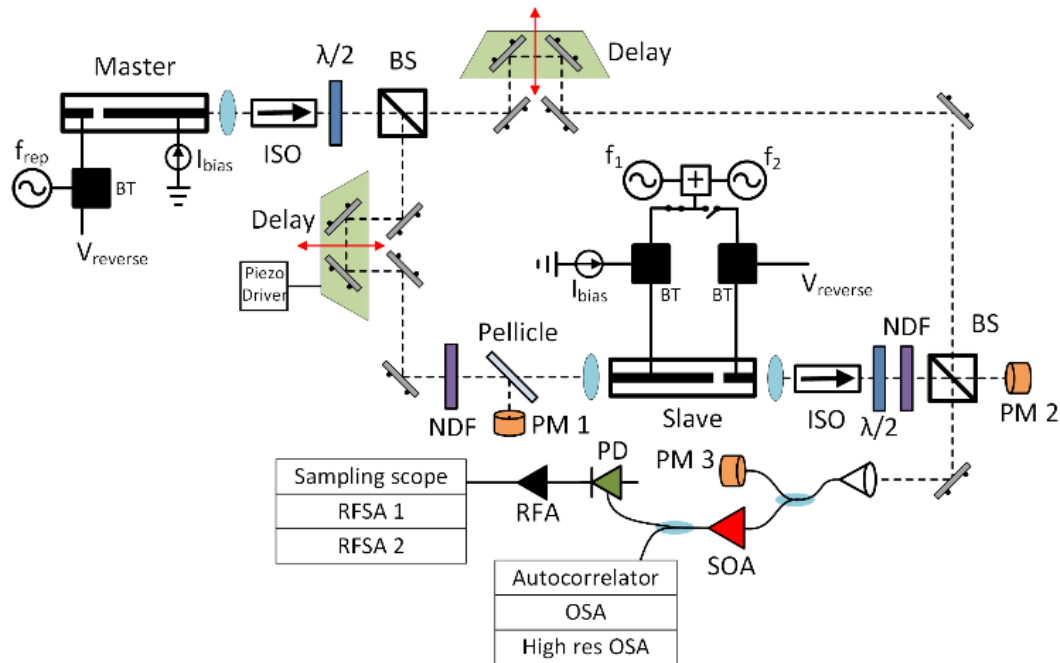


Figure 4-6. Experimental setup. ISO: Isolator; BS: Beam splitter; $\lambda/2$: Half-wave plate; NDF: Neutral density filter; BT: Bias-Tee; PM: Power meter; SOA: Semiconductor optical amplifier; PD: Photo-detector; RFA: Radio frequency amplifier; OSA: Optical spectrum analyzer; RFSA: Radio frequency spectrum analyzer

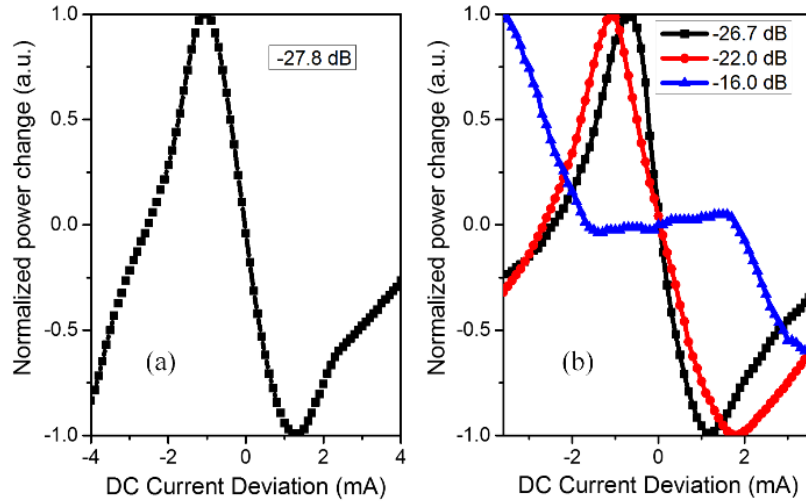


Figure 4-7. Normalized change of the output power of the MZI (static phase change) as a function of DC current deviation of the slave laser. Master laser is running with $I_{\text{gain}} = 65$ mA, $V_{\text{SA}} = -1.8$ V, $T = 20$ °C and 6 dBm of RF power at 22.998 GHz. Slave laser is running with $I_{\text{gain}} = 65$ mA, $V_{\text{SA}} = -1.9$ V and $T = 19.100$ °C. Here the power injection ratio was -27.8 dB, (b) Static phase response as a function of DC current deviation for different power injection ratios. The locking bandwidth increases as the injection ratio increases, however by further increasing it, the relaxation oscillations dominate and the injection-locking becomes unstable (-16 dB).

Figure 4-8 shows the high resolution optical spectra of the slave laser for different bias currents, where 1 μ W of optical power from the gain side of the master laser (equivalent to -27.8 dB of power injection ratio) is injected to the slave laser. Here the master laser bias current is kept constant at 65 mA. The injection seed from the master laser is at 1556.3688 nm and shown with a

solid black line. The slave follows the master in the approximate current range of ~ 64 mA to 66 mA. As shown in Figure 4-8 for the bias currents which are outside of the locking bandwidth, the injection-locking becomes unstable and both the slave and master laser outputs are seen inside the slave laser spectra.

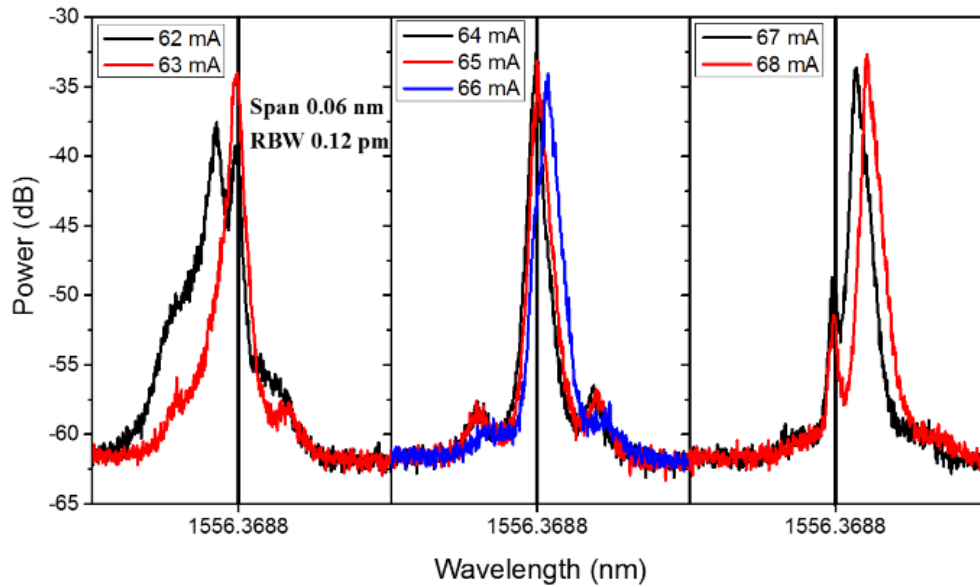


Figure 4-8. High resolution optical spectra of the slave laser for different bias currents. The slave remains locked for the bias currents between 64 mA to 66 mA and unlocks for currents outside of the locking range. The 1 μ W injection signal (-27.8 dB of injection ratio when slave is biased at 65 mA) from the master laser is coupled into the slave laser from the gain section facet. Master laser bias current is kept constant at 65 mA. The injection seed from the master laser is at 1556.3688 nm and shown with the vertical solid black line.

4.4. Two-tone intermodulation experiment

Two-tone intermodulation experiment results are presented in this section as a measure of the linearity of this modulator. The bias point of the modulator is critical since any deviation from the quadrature point would deteriorate the linearity of the modulator. The starting bias point could be off because of the asymmetric locking range of the resonant cavity. This is associated with any semiconductor laser with a non-zero α parameter [61]. This issue has been addressed by finding the center point of the static phase response curve and its corresponding bias current (here was 64.7 mA) and readjusting the bias current to this new value. The interferometer is again balanced accordingly.

In order to measure the signal to intermodulation ratio, the modulator (gain section current or saturable absorber voltage) is modulated with two RF signals with the frequencies of 300 MHz and 400 MHz simultaneously. As shown in Figure 4-6, the RF signals are combined using a 3-dB coupler and applied to the bias-tee of either gain section or SA section. The photo-detected RF signal of the modulated light is split into two and monitored with two radio frequency spectrum analyzers at the same time; one for fundamental frequencies with a larger frequency span and the other for third-order intermodulation tones at 200 MHz and 500 MHz with a span of 512 Hz. Figure 4-9 (a) shows the photo-detected RF power spectrum of the fundamental tones. To be able to compare the third-order intermodulation tone when modulating the gain with third-order intermodulation tone when modulating the SA, the input powers to the modulator are adjusted in such a way that the same fundamental powers are seen after photo-detection. The applied input RF power was -16 dBm when modulating the gain and -24 dBm when modulating the SA. Figure 4-9

(b) and (c) show the third-order intermodulation tones at 200 MHz and 500 MHz, respectively. The 500 MHz sideband is used for the calculations since it was the larger spur compared to the 200 MHz sideband. From this data, signal-to-intermodulation ratios of 50.8 dB and 55.3 dB are obtained when modulating the gain and SA, respectively. A ~ 4.5 dB improvement is achieved by modulating the voltage of the SA over the gain of the slave laser since modulating the SA would create less AM as opposed to modulating the gain (carrier density) of the slave laser.

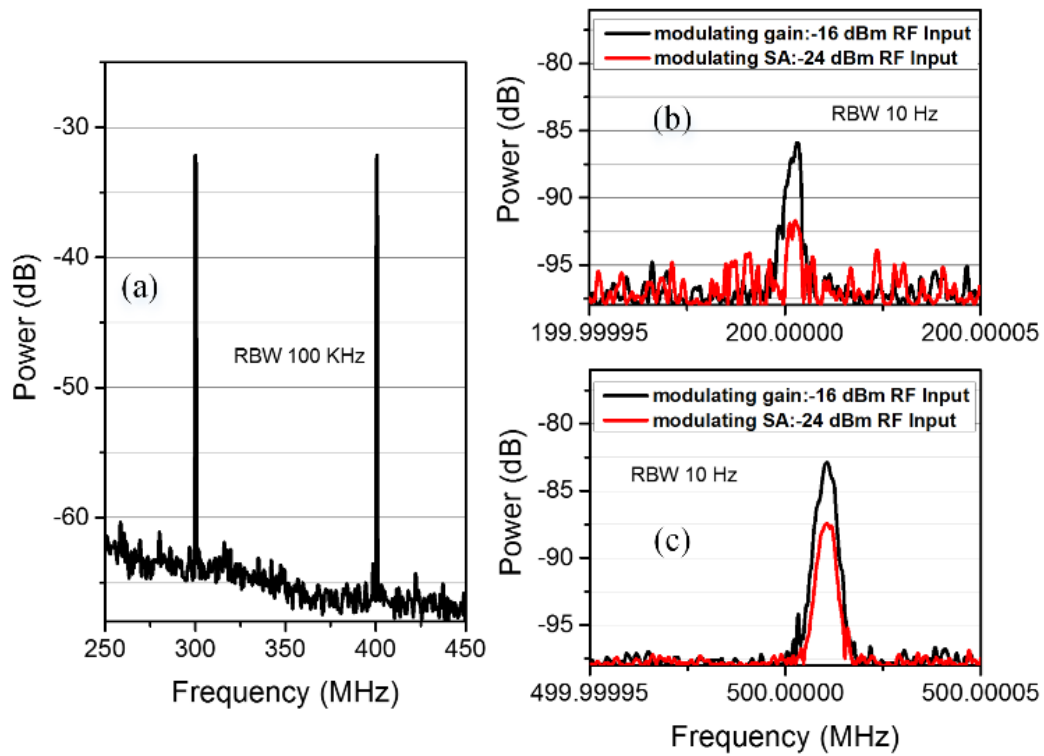


Figure 4-9. (a) Photo-detected RF power spectrum of fundamental frequencies for the input RF power of -16 dBm when modulating the gain and -24 dBm when modulating the SA (the input powers are adjusted to achieve the same fundamental powers for comparison), (b) detected RF power spectra of the third-order intermodulation tones at 200 MHz, (c) detected RF power spectra of the third-order intermodulation tones at 500 MHz. Intermodulation tone shown in black when modulating the gain section and shown in red when modulating the SA section.

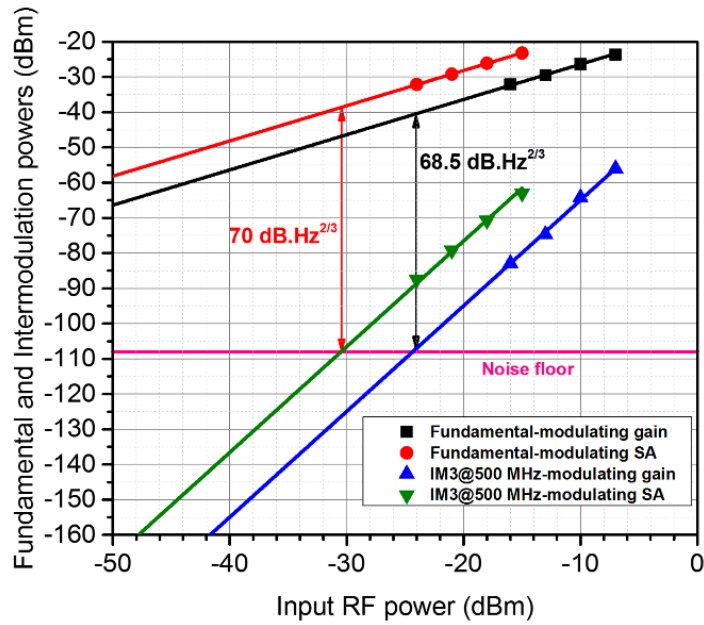


Figure 4-10. Fundamental and third-order intermodulation powers as a function of the input RF power to the modulator.

Figure 4-10 shows the fundamental and third-order intermodulation powers for different input RF powers for each of the gain and SA modulation cases. A linear fit of slope one and another linear fit of slope three are applied to the fundamental and intermodulation tones respectively. Spur-free dynamic range of $68.5 \text{ dB.Hz}^{2/3}$ and $70 \text{ dB.Hz}^{2/3}$ are obtained from modulating the gain and SA, respectively [60]. Here the SFDR measurement is limited by noise from beating between the relatively broad linewidth laser modes.

4.5. Discussion and conclusion

The modulation bandwidth of this modulator is limited by the steady state solution of Adler's equation which suggests that the modulation frequency should be much slower than the repetition rate of the MLL. Assuming a 5% ratio, this would give a modulation bandwidth of about 1.1 GHz for the MLLs used here. The modulator still would operate for higher frequencies, however the phase response would deviate from the arcsine. The bandwidth could be increased by having MLLs with higher repetition rates [62]. This can be realized by having shorter physical length and employing the colliding pulse MLL scheme. This type of modulator with a very high sampling rate could be used for oversampled sigma-delta ADC [1].

The frequency shifting of the slave laser necessary to induce the arcsine phase response is expected to be linear with respect to current of the gain section (or the voltage of SA section) within a small locking bandwidth. This is confirmed by measuring the optical frequency shift on a high resolution optical spectrum analyzer while tuning the current of the gain section (not shown here). Furthermore, the 120 dB.Hz^{2/3} SFDR obtained in [58] by utilizing a VCSEL as the resonant cavity suggests a highly linear response in the small locking range.

The SFDR measurement provided here is limited by noise from beating between the relatively broad linewidth laser modes. This noise extends to higher frequencies as the optical linewidth of the lasers get larger (here about ~200 MHz). This could be addressed by reducing the overall loss of the cavity such as improving the waveguide design and coating the facets. Also there have been many reports on narrow optical linewidth monolithic MLLs using different material system [63].

Currently available electronic ADCs with similar bandwidth may offer comparable or modestly better SFDR and ENOB to results reported here. However we believe our novel design has the potential for significantly higher bandwidth and linearity, ultimately providing a superior ENOB compared to electrical samplers of the same bandwidth.

Finally a novel linearized intensity modulator for pulsed light is presented in this chapter. This has been realized by introducing a passively MLL injection-locked to a hybridly MLL (which is the input to the MZI) into one of the arms of the MZI. By modulating the injection-locked laser, one can induce arcsine phase response on each of the injected longitudinal modes. A linear intensity modulator is obtained by interfering the modulated light with its unmodulated counterpart from the other arm in quadrature. A low V_π of 8.5 mV eliminates the need for a linear RF amplifier required for RF signal amplification in the case of LiNbO₃ modulator. The current of the gain section or voltage of the SA are used to modulate the slave laser. Modulating the SA provides a reduced AM and hence a reduced third-order intermodulation tone with respect to modulating the gain. A SFDR of 70 dB.Hz^{2/3} is obtained when modulating the SA. The reported SFDR is limited by the noise of the MLLs. Employing this novel linearized modulator in an analog optical link offers the potential to improve the resolution and the overall performance of the photonic sampled ADC.

5. HIGHLY LINEAR INTENSITY MODULATOR FOR PULSED LIGHT USING THREE-SECTION MLLS

5.1. Introduction

As discussed in chapter 4, the linearity of the linearized modulator is limited by the unwanted amplitude modulation produced when modulating the gain section or saturable absorber section. This can be addressed by decoupling the phase and amplitude responses. Here in this chapter, we propose the use of a three-section device which an additional passive section is introduced into the previous design. This section is transparent to the operating wavelength of the laser and hence does not absorb any light when its current (or voltage) being modulated well below the threshold current. Figure 5-1 shows the schematic of the proposed three-section device. It consists of gain, saturable absorber and phase sections [64].

In this chapter we will discuss the principle of operation of the three-section device and explain how the absolute position of the frequency combs changes when applying the modulation signal to the passive section. Also in order to make the passive section transparent at the operating wavelength of the laser, we have used the impurity free vacancy disordering method (IFVD) to selectively tune the bandgap of the passive section. Silicon nitride and silicon oxide dielectric layers have been used to promote and inhibit the intermixing process, respectively. Also additional fabrication steps needed for the three-section device has been explained and discussed. Finally the experimental setup for the highly linear interferometer has been built and the results are presented.

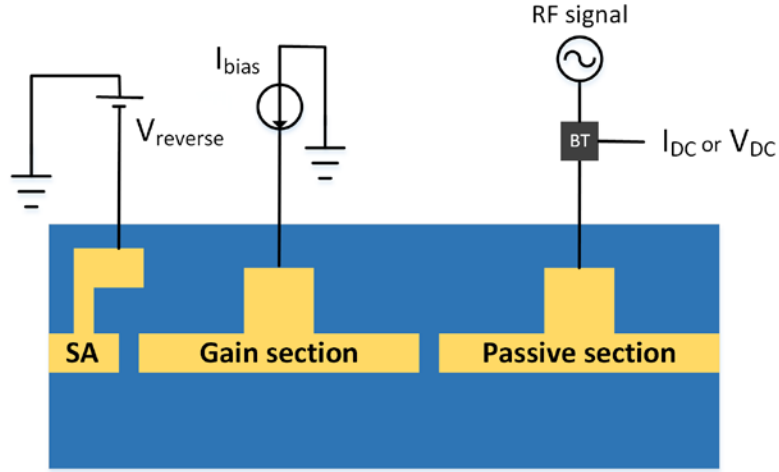


Figure 5-1. Schematic of the proposed three-section device including: gain section, saturable absorber section and the new passive (phase) section. The modulation signal can be now applied through the passive section.

5.2. Three-section MLL principle of operation

Changing the current of the gain section or the voltage of the saturable absorber section has been used previously to shift the absolute frequency of the comblines to be able to induce the arcsine phase response. However there are two main drawbacks in employing them for modulation. Modulating the gain or saturable absorber is associated with an unwanted amplitude modulation which deteriorates the overall linearity and performance of the modulator. It is needed to be mentioned here that the ideal case when modulating the slave laser comblines would be tuning all of the comblines positions together with minimal change of the frequency spacing between them.

We believe that the new design could make this possible. Here in the new design, by modulating the current of the passive section, one can induce refractive index change in that section and therefore can change the frequency spacing of the optical modes. To give an approximate example assuming a 1.877 mm long device with 20% passive section length and also with a refractive index change of about 10^{-4} , would create 0.127 MHz change in the frequency spacing of the comb lines. Since the fixed point for repetition rate change is near DC for a passively MLL [65-67], as shown in Figure 5-2, small change in frequency spacing accumulate from DC to the optical frequencies. Assuming the repetition rate (comb lines spacing) of 22.656 GHz would make the comb line at optical wavelength of 1550 nm, the 8542th comb line from the DC point. This makes the total shift at this comb line to about 1.08 GHz which is enough for inducing arcsine phase response in the locking bandwidth. So only small changes are needed to achieve a greatly magnified ($\times 8542$) shift at optical frequencies [64].

The amount of current needed in order to introduce 10^{-4} change in the refractive index through the plasma effect would be very small (in the order of 1 mA) and this is well below the lasing threshold current of that section. This promises a pure phase response with minimal amplitude modulation. This also could lead to a significant reduction of the V_{π} of the modulator.

$$n = \left(\frac{f_{1550nm} = 193.5 \text{ THz}}{f_{rep} = 22.656 \text{ GHz}} \right) \approx 8542$$

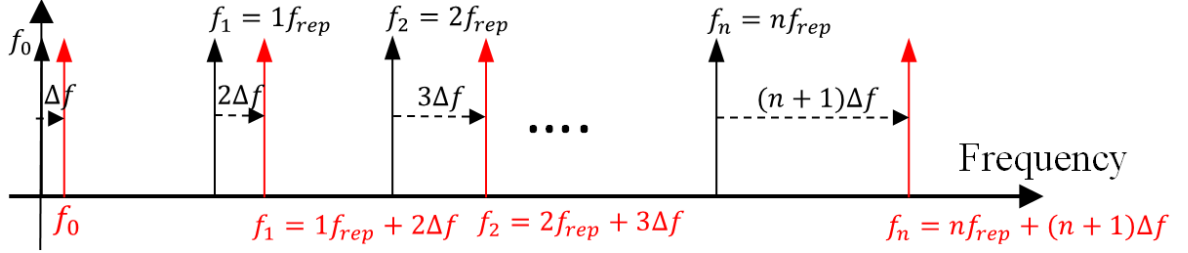


Figure 5-2. Visual representation of the frequency shift of the MLL when it is modulated through its passive section. Black and red shows the optical modes and their absolute location when the passive section is unbiased and biased, respectively.

5.3. Impurity free vacancy disordering

5.3.1. Introduction

Different bandgap of semiconductor active region is needed in order to achieve integration of optoelectronic devices, such as modulators, laser, detectors, and etc. in a common substrate platform. Selective bandgap tuning of semiconductor active region has been done in order to be able to introduce multiple functionalities. There have been numerous report on bandgap engineering of semiconductor materials and they all fall into two main categories: during growth or post growth. The former could be either through grow-etch-regrowth [68-70] or selective-area

epitaxial growth [71, 72]. It is possible to produce large and very controllable bandgaps differences with good spatial resolution on the wafer with these techniques, however they need multiple epitaxial growth steps and ultimately become very expensive. Also selective-area growth needs precise masking layers and accurately tailoring the growth conditions. Extensive studies have been done on the second method which is the post-growth bandgap tuning method since it provide a much simpler, less time consuming and most importantly less expensive method. This method is named quantum well intermixing (QWI) [73, 74] for quantum well materials.

The QWI process is a simple post-growth bandgap tuning method that modifies the bandgap energy of an existing quantum well system by intermixing the composition of well and barrier layers. The intermixing is achieved by introducing point defects in selected area while rapid thermal annealing (RTA) is used to promote the intermixing process. This method could deliver multiple bandgap wafers with less complexity and less cost compared to grow-etch-regrowth method. There are several approaches reported to achieve intermixing such as impurity induced disordering (IID) [75, 76], photo-absorption induced disordering (PAID) [77, 78], ion implantation induced intermixing [79, 80], plasma induced intermixing [81], and impurity free vacancy disordering (IFVD) [73, 82, 83]. Among these IFVD has received a great deal of attention because of simplicity, being cost effective, good spatial resolution and also conserving the electrical property of quantum well material. This method usually involves the deposition of dielectric layer followed by rapid thermal annealing (RTA). Several dielectric layers such as SiO_2 , Si_3N_4 , SrF_2 , and TiO_2 have been used to inhibit or promote the intermixing [84-86]. By properly choosing the dielectric capping layers and RTA conditions (time and temperature), one can induce atomic interdiffusion between the quantum well and barriers compositions. The constant flow of atoms

(from region with high concentration to low concentration) between the wells and barriers when annealing causes blurring of the previously sharp concentration gradient between the well and barriers. As shown in Figure 5-3, this blueshifts the emission properties of the quantum well material and also widens its optical bandgap.

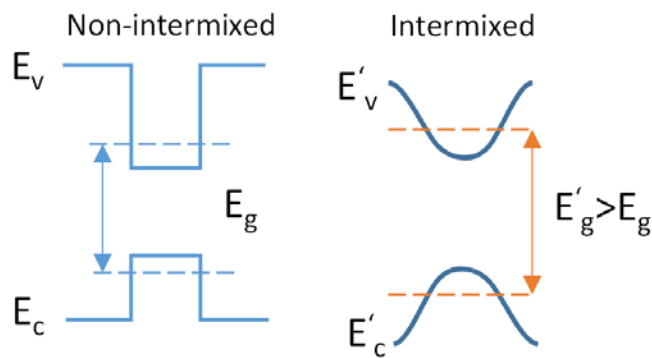


Figure 5-3. Schematic diagram of the energy levels and energy bandgap for intermixed and non-intermixed regions.

There have been reports on two approaches for intermixing of the AlGaInAs QW structures, one using the sputtered SiO_2 as the promoter [87, 88] and the other one suggesting the use of PECVD Si_3N_4 dielectric layer [89, 90]. The former method is based on the point defects created during SiO_2 sputtering and it is proven to work for different material systems such as GaAs-AlGaAs, InGaAs-InGaAsP, InGaAs-InAlGaAs, and AlGaInAs-AlGaInAs [88]. The point defects produced during the sputtering process, results in an increased rate of atomic interdiffusion during the annealing stage. This is a universal method since it works for the wide range of material

systems and there is no need for dielectric material characterization for each of the material systems. A thin layers of SiO₂ is sputtered using Ar: O₂ gas mixture with a self-DC bias of 1 kV and a processing pressure of 5×10^{-3} mbar. The sputtering is followed high temperature annealing (650 °C-750 °C). Figure 5-4 shows the measured PL for the InGaAsP and InAlGaAs material systems as a function of RTA temperature for the annealing time of 1 min. Bandgap shift is observed for InGaAsP samples capped with sputtered SiO₂ at temperatures as low as 550 °C. Meanwhile, the sample covered with PECVD SiO₂ serves as a good inhibitor until the 650 °C. For InAlGaAs material systems, bandgap shift are observed at around 650 °C for the sample capped with sputtered SiO₂ caps and it increase with increasing the annealing temperature, up to about 100 meV for 750 °C. The InAlGaAs samples covered with PECVD SiO₂ has shown no significant shift in the range of temperature shown in the figure. This makes the sputtered and PECVD SiO₂ layers ideal materials as the intermixing promoter and inhibitor for the InAlGaAs systems, respectively. Also temperature needed for enough bandgap shifting for this material system is low enough that the thermally induced intermixing are not expected to occur. This is very important and critical as the electrical properties of the material system preserves during the intermixing process. Also the areas that intermixing are needed to be inhibited remain unperturbed.

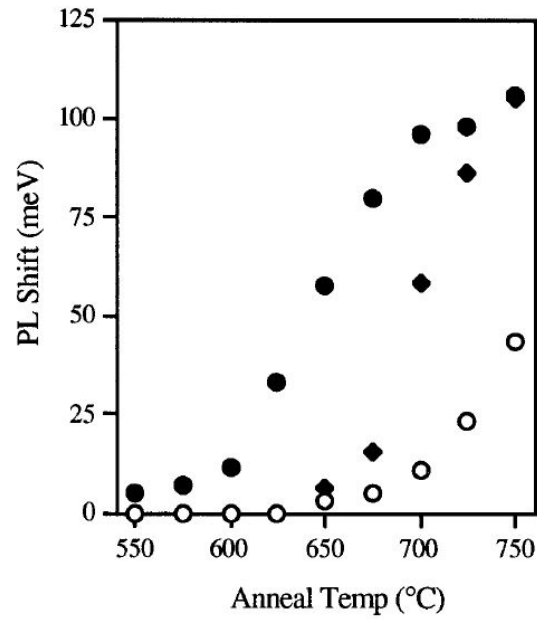


Figure 5-4. Measured PL shifts as a function of anneal temperature for InGaAsP with 200 nm sputtered (●) and PECVD (○) SiO₂ caps and AlInGaAs capped with 200 nm sputtered SiO₂ (◆) [87].

Another reported method for AlGaInAs quantum well intermixing is introduced in [89]. They have suggested the use of a 50 nm thick layer of Si₃N₄ as the intermixing promoter followed by annealing at high temperature of 720 °C for 2 min. The Si₃N₄ layer is deposited using a mixed frequency option of the PECVD machine. Depositing with the high frequency RF signal creates tensile films while depositing with low frequency RF signals provides compressive films. Therefore by carefully adjusting the low and high frequency intervals, one can possibly obtain an almost stress-free thin layer of Si₃N₄. Figure 5-5 shows the composition analysis of the intermixed

AlGaInAs quantum well structures using secondary ion mass spectrometry (SIMS) [90]. As it is shown the bandgap shift is mainly attributed to the interdiffusion of In and Ga between quantum wells and barriers. The In and Ga are interdiffused for the sample covered with Si_3N_4 when annealing at 720 °C for 2 min, however there is no interdiffusion for the uncapped sample.

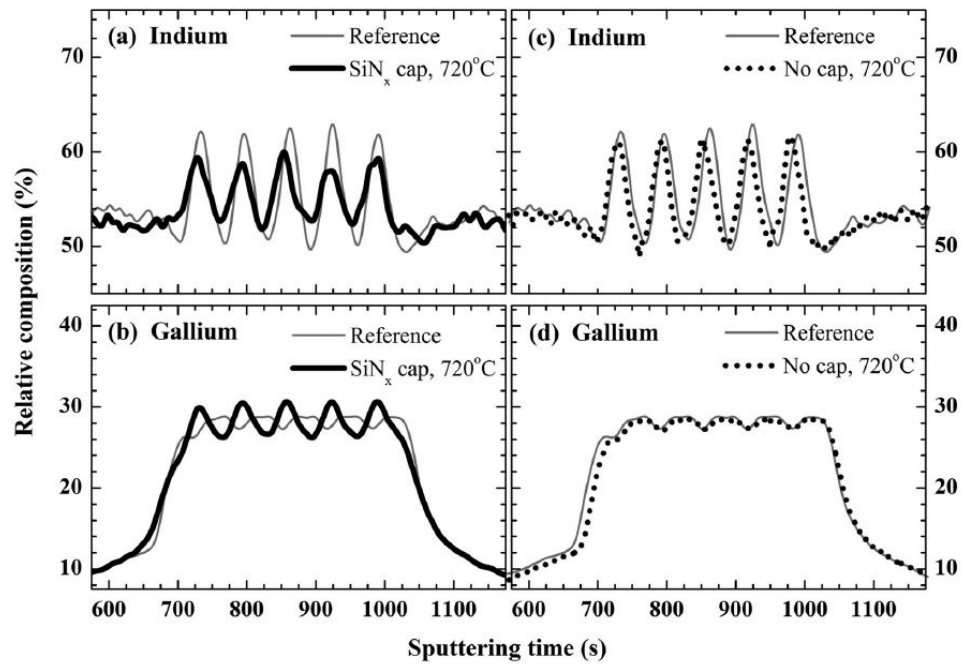


Figure 5-5. Compositions analysis of the AlGaInAs multiple quantum wells and barriers measured by SIMS for (a) In and (b) Ga atoms in the intermixed sample and for (c) In and (d) Ga atoms in the non-intermixed sample. Samples were annealed at 720 °C for 2 min and only the intermixed one was with a Si_3N_4 dielectric film capping layer. The data are compared to a reference (no annealing) sample [90].

In [89], 200 nm of PECVD SiO₂ is used to cover the whole sample (as the inhibitor and also to protect the sample surface) after selectively defining the intermixing regions with 50 nm of Si₃N₄. The sample then annealed at 720 °C for 2 min under nitrogen ambient. Figure 5-6 shows the optical spectra of the two 500-μm-long ridge lasers which on one intermixing is inhibited and the other intermixing is promoted. This data clearly shows more than 100 nm wavelength separation which is enough for active/passive integration purposes. This is a promising result in terms of bandgap shift and the relatively low temperature of 720 °C. However the required 2 min annealing time is long enough for the Zinc dopant (of the first two heavily-doped layers) to back-diffuse into separate confinement heterostructure layers and accumulating above the active region of the area where the intermixing has been promoted. This increase the optical loss due to intervalence band absorption and also sub-bandgap absorption [90]. This makes this technique unsuitable for electro-absorption modulator fabrication as it cannot tolerate high voltages (needed for modulation) because of zinc back-diffusion. This is the main drawback of this method and it can only be used where there is no need for applying high voltages to the device. However, it is needed to be mentioned that the first method described here in [88], allows applying high voltages to the device. This is mainly because of the lower annealing temperatures (<700 °C) and also shorter annealing times, as an increase in both of these parameters contribute to more Zinc back-diffusion.

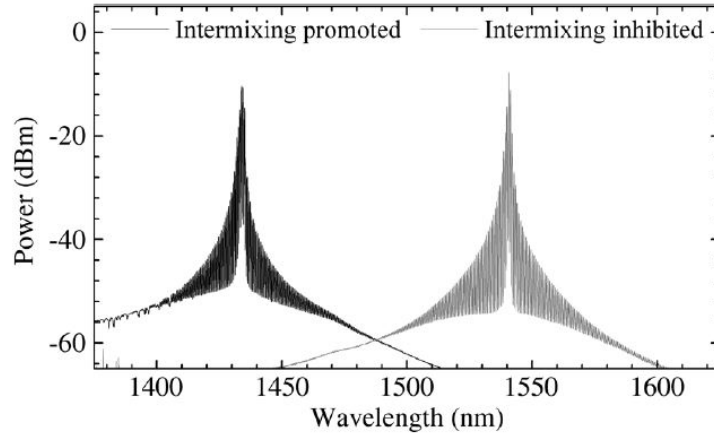


Figure 5-6. Optical spectra of 500- μm -long edge emitter lasers from the area that intermixing is promoted and inhibited [89]

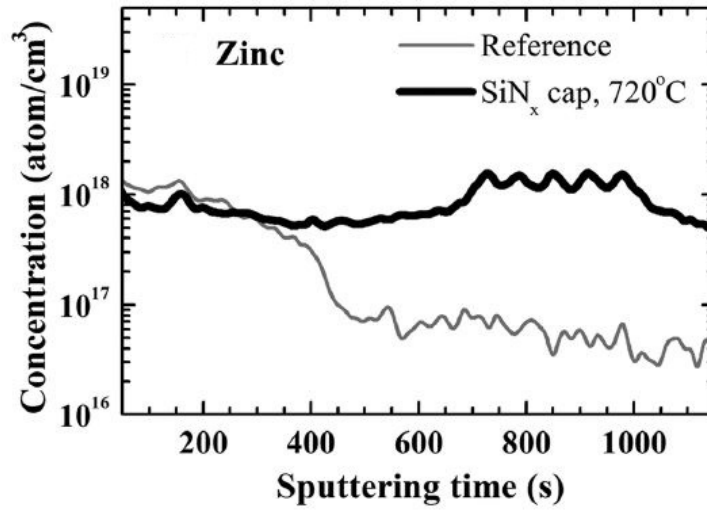


Figure 5-7. (a) Profile analysis of Zn concentration measured by SIMS in intermixed AlGaInAs multiple quantum wells and barriers as well as in top AlGaInAs SCH guiding layer. The data are compared to a reference (no annealing) sample [90].

5.3.2. Photoluminescence measurement setup

A fiber coupled semiconductor laser at 980 nm is used here as the excitation source. Figure 5-8 shows the experimental setup that being built for photoluminescence measurement. A WDM fiber coupler/divider has been used to selectively couple the each wavelength into different port. It is designed specifically for 980 nm and 1550 nm wavelengths. A lensed fiber has been used to illuminate the sample with 70 mW of 980 nm light and simultaneously couple back the 1550 nm emission from the sample. A XYZ stage also is used to control the positioning of the sample. The 1550 nm photoluminescence redirects to 1550 nm port and it is connected to an optical spectrum analyzer. The excitation source power plays a key role for this measurement as too much power will heat up the sample and shifts and widens the photoluminescence spectrum. The 70 mW power and the distance between the lensed fiber and the sample is always kept unchanged when measuring the PL for different samples.

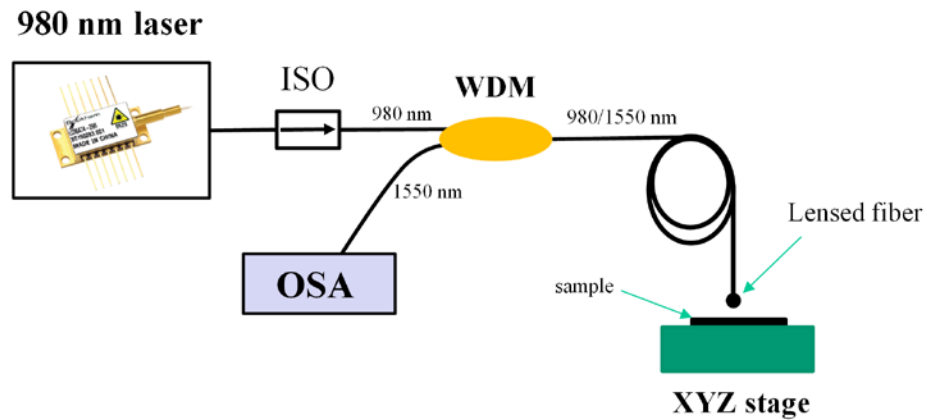


Figure 5-8. Experimental setup for photoluminescence measurements at room temperature.

5.3.3. Bandgap tuning experiment and results

In this thesis, the PECVD SiN_x approach has been chosen as the intermixing promoter over RF sputtered SiO_2 approach because of the equipment availability. In order to characterize the parameters needed for intermixing process, the samples are prepared by first depositing the PECVD SiN_x on the whole sample. Then half of the sample is covered by a clean mechanical wafer followed by dry etching of the SiN_x of the uncovered area. Finally the whole sample is covered with PECVD SiO_2 as the intermixing inhibitor and also in order to protect the surface of the sample. Figure 5-9 shows a schematic of the prepared sample with dielectrics defining the area that intermixing needed to be promoted (area beneath SiN_x layer) and the area that intermixing needed to be inhibited (area beneath SiO_2 layer).



Figure 5-9. Schematic of dielectrics deposited selectively on quantum well sample to be able to define the regions that intermixing is needed to be promoted (SiN_x capped) and inhibited (SiO_2 capped).

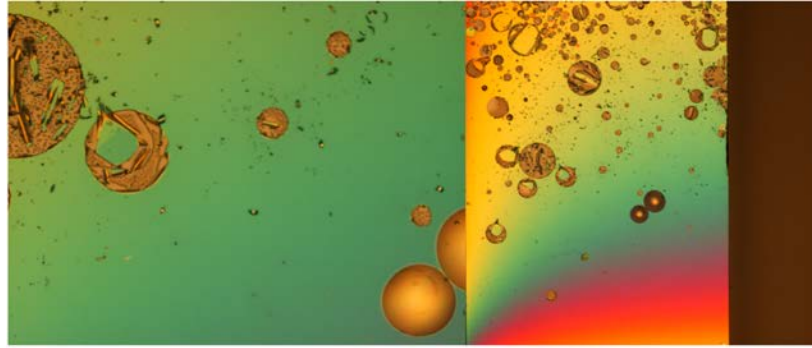


Figure 5-10. The cracks occurred on the sample upon annealing because of the different thermal expansion between the dielectrics. The SiO_2 layers is deposited first and then half of the sample is covered and the uncovered SiO_2 is etched away. Finally the whole sample is covered with SiN_x .

Another possible approach would be depositing the SiO_2 layer first and dry etching the uncovered area followed by depositing the SiN_x layer on the whole sample. However this has been experimented as it is shown in Figure 5-10. As it can be seen cracks are occurred after annealing the sample at high temperatures and basically destroys the sample surface and makes it unsuitable for reliable fabrication. This is mainly because of the different thermal expansion of the dielectric layers when deposited in this specific order.

Because of annealing at the very high temperature special attention has been made in this work to deposit low stress dielectric films. PECVD deposited SiO_2 usually has a small compressive stress which is independent of gas ratios and RF power used for deposition [91, 92]. However, PECVD deposited SiN_x films using standard gases of SiH_4 , NH_3 and N_2 and using single frequency

of 13.56 MHz are tensile in nature [93]. A common technique to control the stress of SiN_x films is the addition of low frequency power (380 KHz) which creates compressive SiN_x films. By controlling the intervals of high and low frequencies when depositing, one can adjust the stress of the films [93]. An alternative method is suggested when working with single frequency PECVD machines and that is the addition of He gas to the previously standard gases. This has been shown in the Figure 5-11 for SiN_x deposited at the temperature of 250 °C and for different RF powers. As it is shown the stress can be tuned from tensile region to the compressive region by increasing the amount of He gas.

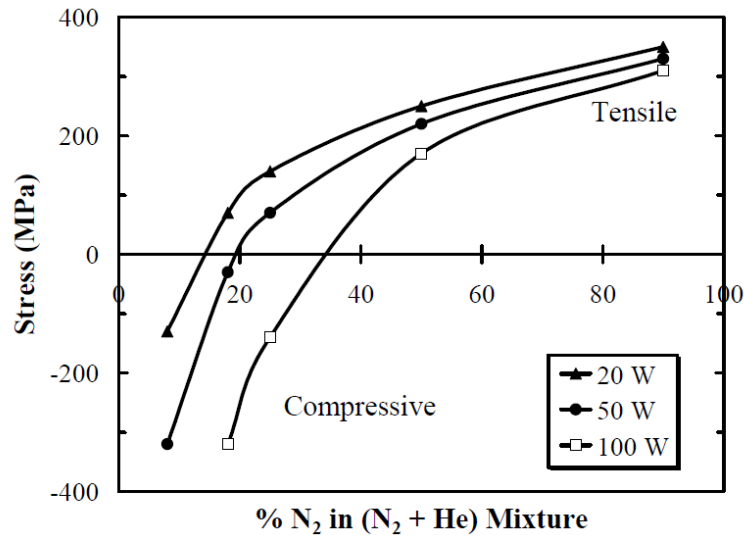


Figure 5-11. PECVD deposited SiN_x stress control by the He dilution method. Films are deposited at the temperature of 250 °C with different RF powers [93].

Different SiN_x recipes has been tried and their film quality when annealing and photoluminescence shift are examined in order to find the best conditions to deposit the SiN_x

dielectric layer. Some of the recipes are shown in Table 9. In all of these recipes, RF power, processing pressure and total N_2 are kept almost unchanged. A fixed 600 sccm of He is used in some of the recipes to reduce the stress. On those recipes the $N_2/(He+N_2)$ ratio are kept constant and only the NH_3 levels are changed. It is made sure to keep the mentioned ratio at 45% and the amount of N_2 the same. It is needed to be mentioned here that the changing the 2% diluted silane would cause a change in the total amount of N_2 .

All of the samples are prepared first by depositing 70 nm of SiN_x using recipes shown in Table 9, followed by covering half of the sample with mechanical wafer and dry etching the uncovered area. Finally the whole sample is covered with 185 nm of SiO_2 . The SiO_2 is deposited using the recipe shown in Table 10. The samples are annealed in the nitrogen ambient at the temperature of 800° C for 2 min. The peak of the PL spectrum of each of the samples are also shown in Table 9.

Table 9. Deposition parameters of the recipes used for SiN_x deposition. The flow unit for all of the gases is standard cubic centimeters per minute (sccm). The samples are annealed at the annealing temperature of 800 °C for 2 min. For the sake of consistency, SiN_x and SiO₂ dielectric layer thicknesses are kept the same (70nm±5nm and 185nm±10nm for SiN_x and SiO₂, respectively).

	LS-SIN2	LS-SIN6	LS-SIN5	SIN-DIFF
Pressure (mTorr)	940	940	940	900
N₂	200	200	200	400
He	600	600	600	-
SiH₄+N₂	300	300	300	120
Silane	6	6	6	2.4
NH₃	4.05	4.66	3.47	4.56
RF (W)	100	100	100	100
Total N₂	500	500	500	520
NH₃/SiH₄	0.675	0.775	0.575	1.9
N₂/(He+N₂)	45%	45%	45%	-
PL shifted to	1343 nm	1360 nm	1354 nm	1390 nm

Table 10. Deposition parameters of the recipe “depsio2” for SiO₂ deposition. The silane gas (SiH₄) used with this PECVD machine is 2% silane diluted in N₂.

Parameters	depsio2
SiH ₄ (sccm)	200
NO ₂ (sccm)	412
Temperature (°C)	246
Pressure (mTorr)	1050
RF power (W)	25
Deposition rate (nm/min)	48-52

The photoluminescence spectra of different samples with different SiN_x are shown in Figure 5-12. The highest blue shift is obtained for the SiN_x deposited using the LS-SIN2 recipe which is about 180 nm. This recipe has been used for SiN_x deposition for further characterization of the intermixing parameters such as ideal annealing time and temperature.

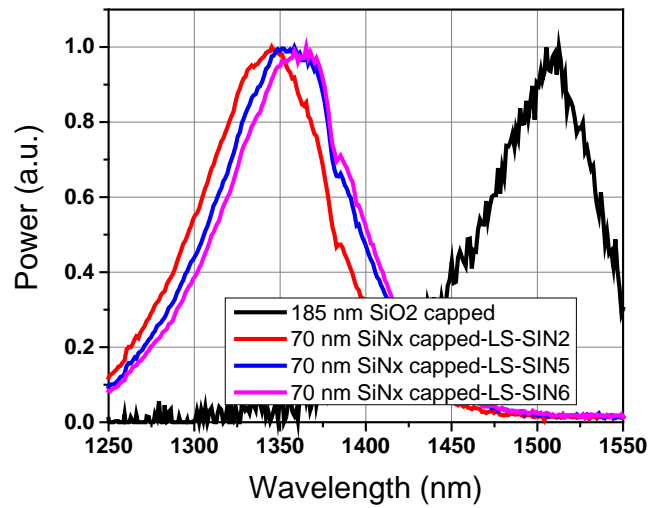


Figure 5-12. Photoluminescence spectra of different samples capped with 70 nm SiN_x layers deposited with different recipes annealed at 800 °C for 2 min.

In another experiment a sample is prepared by depositing ~ 70 nm of SiN_x using the LS-SIN2 recipe followed by covering half of the sample with mechanical wafer and dry etching the uncovered area. Finally the whole sample is covered with 185 nm of SiO₂. The sample is cleaved in smaller pieces and each are annealed for 2 min at different temperature. Figure 5-13 shows the PL blueshifts of the samples capped with SiN_x and SiO₂ as a function of annealing temperature. As it can be seen from Figure 5-13 a 130 nm differential blueshift is obtained between the SiN_x and SiO₂ capping area. This shift is large enough for active/passive integration purposes, however, the high annealing temperature and possibly long annealing time have caused the thermal intermixing in those region. Thermal intermixing happens because of the natural point defects formed when growing the active region. This will introduces more loss to the active region and degrades the performance of device.

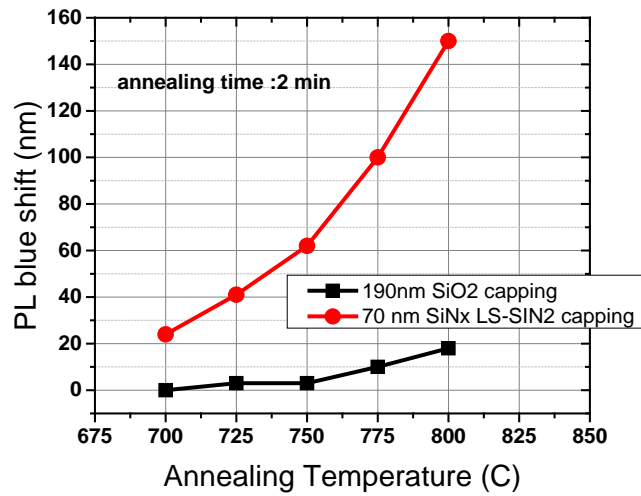


Figure 5-13. Photoluminescence blue shift of the sample capped with 70 nm SiN_x and capped with 190 nm of SiO₂ for different annealing temperature (annealing time was kept 2 min for all of the samples).

In order to find the approximate annealing time, another sample is prepared with 77 nm and 187 nm of SiN_x and SiO₂ capping area, respectively. Figure 5-14 shows the measured PL blueshifts of the SiN_x and SiO₂ capping areas as a function of annealing time for the annealing temperature of 800 °C. As it can be seen a blueshift of about 90 nm is obtained when annealing for 45 seconds. This is ideal since the active area (SiO₂ capping) is minimally perturbed and the blueshift is less than 5 nm compared to as grown PL spectrum. Also the 90 nm could be sufficient for the active/passive integration purposes. Also as it is shown in the Figure 5-14 more shift is obtained for the SiN_x capping area by annealing for a longer time, however, the thermal intermixing also starts to happen and this also blueshifts the PL spectra of the active region.

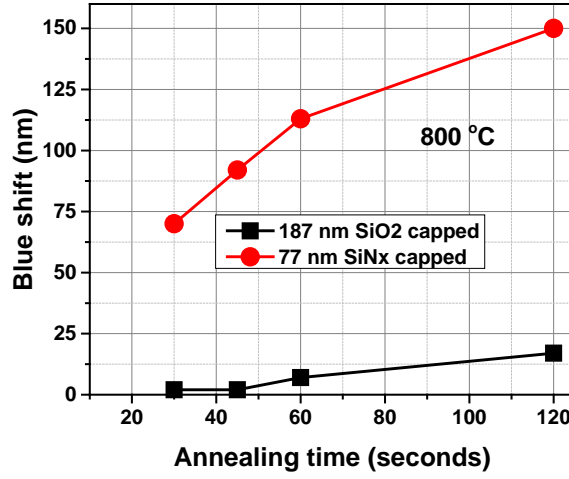


Figure 5-14. Variation of measured photoluminescence blue shift versus annealing time for SiO₂ and SiN_x dielectric capping layers (Annealing temperature remained unchanged at 800 °C).

5.4. Mask design and fabrication

Figure 5-15 shows a captured image from the L-Edit software of the design layout of a ~ 1.9 mm three-section mode-locked laser. The 3 μ m waveguide is shown in blue and it is overlapped intentionally with metal pads (in green). Cleaving marks are put in the design to be able to cleave the saturable absorber with desired length. Different cleaving marks are introduced into the design to achieve different length ratios between the gain and SA section (1% to 5%). The passive section length is designed to be 20% of the total length. The area shown in red is a level in the mask design that is needed for defining the area that needed to be intermixed. Other features are serving as

alignment and cleaving marks. Additional contact pads are introduced in the design so they can be used for high speed probe application.

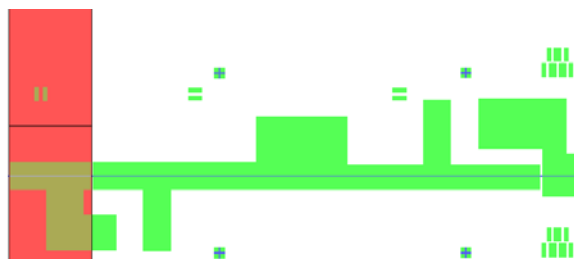


Figure 5-15. Image of the three-section mode-locked laser design from L-Edit software showing waveguides and alignment marks in blue and metal pads, alignment marks and cleaving marks in green. The red region (passive section) shows the area that needed to be intermixed.

Fabrication of the three-section mode-locked lasers are started by cleaving and cleaning a sample similar as described in sections 2.4.1 and 2.4.2. The cleaning is followed by deposition of 75 nm of SiN_x using the LS-SIN2 recipe. It is made sure that the deposition chamber of the PECVD machine is thoroughly cleaned before deposition. The SiN_x deposition is followed by UV positive lithography and SiN_x etching to define the regions that needed to be intermixed selectively. The steps are summarized below:

1. Spin-coat the PR1805 @ 3500 rpm for 40 seconds
2. Pre-bake @ 120 °C for 4 min
3. UV Exposure @ 12 mW for 5.5 seconds
4. Develop in AZ351 and DI water (ratio of 1:7) for ~25 seconds
5. Post-bake @ 120 °C for 4 min

6. Run recipe “Descum” on PECVD for 2 min
7. Run recipe “etchsin1” on PECVD for 1 min and 15 seconds
8. Photoresist removal. Dip the sample in acetone @ 80 °C for 5 min then rinse with acetone, methanol and isopropanol and dry with N₂
9. Run recipe “prremove” on PECVD for 7 minutes.

The “prremove” is a critical step since the remaining photoresist has to be removed using the PECVD machine otherwise it reduces the amount of blueshift occurred in the SiN_x capping area. The above steps are immediately followed by deposition of 190 nm SiO₂ using the “depsio2” recipe. The sample then annealed using a RTP-600S system at the temperature of 800°C for 30 seconds using the recipe shown in Table 13.

Figure 5-16 shows the measured photoluminescence spectra of the SiN_x capping area (blue) and SiO₂ capping area (red). A differential blueshift of 73 nm is obtained between the active and passive area and more importantly the blueshift in the SiO₂ capping area (active area) is limited to below 10 nm. This is critical since it is ideal to have the optical and electrical properties of the active area unchanged.

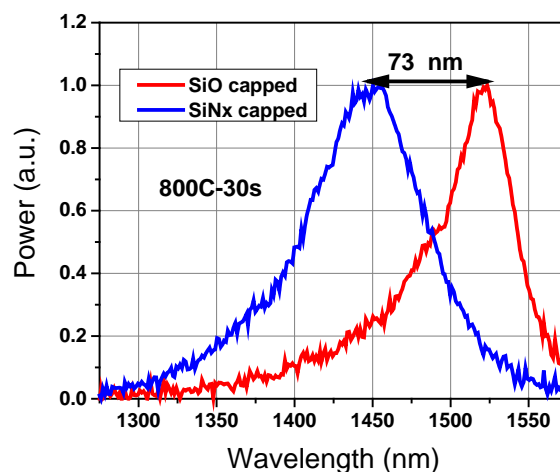


Figure 5-16. Measured photoluminescence spectra of the area capped with SiN_x (passive section) and the area capped with SiO₂ (gain and SA sections) annealed at 800 °C for 30 seconds.

In order to have a reference (after removing the dielectric layers) to align the waveguides with respect to the intermixed and non-intermixed regions, alignment marks are designed on the original mask layout. The alignment marks are etched through the first layer in order to have the exact location of the active/passive regions. Negative lithography and wet etching steps needed to do this are summarized below:

1. Spin-coat the NR9-1000P @ 4000 rpm for 40 seconds
2. Pre-bake @ 150 °C for 1 min
3. UV Exposure @ 10 mW for 2 seconds
4. Post-bake @ 100 °C for 1 min
5. Develop in RD6 for ~ 20 seconds

6. Post-bake @ 100 °C for 1 min
7. Run recipe “Descum.prc” on PECVD for 2 min. This is to remove any remaining thin layer of photoresists.
8. Run the “etchsio2” recipe (shown in Table 11) for 4 min to etch the SiO₂ layer.
9. Run the “etchsin1” recipe for 2 min to etch the SiN_x layer.
10. Use the H₃PO₄:H₂O₂:H₂O (1:1:30) to etch the first layer for 2 min and 30 seconds
11. Photoresist removal. Dip the sample in acetone @ 80 °C for 5 min then rinse with acetone, methanol and isopropanol and dry with N₂
12. Run the “etchsio2” recipe for about 4 min to remove the SiO₂ layer.
13. Run the “etchsin1” recipe for about 1 min and 30 seconds to remove the SiN_x layer.

The above steps are followed by a fresh deposition of 200 nm SiN_x using the “SIN-DIFF” recipe. The remaining steps of fabrication are similar to what explained in sections 2.4.4 to section 2.4.12.

Table 11. Reactive Ion Etching (RIE) parameters for SiO₂ etching. Etching has been done in the room temperature.

Parameters	etchsio2.prc
O ₂ (sccm)	5
CF ₄ (sccm)	45
Pressure (mTorr)	75
RF power (W)	175
Etching rate (nm/min)	56

Figure 5-17 shows an image taken using a microscope from a 2 mm three-section mode-locked laser after annealing contacts.



Figure 5-17. Top view image of the fabricated 1.9 mm three-section mode-locked laser

In order to characterize each of the intermixed and non-intermixed regions separately, short length ($\sim 360 \mu\text{m}$) laser are cleaved from each sections. They are individually mounted on the copper stud and their optical and electrical characteristics are examined. Figure 5-18 shows the

output power versus current characteristics of these two lasers operating at 20 °C. From the Figure 5-18 (a) a threshold current of 15 mA and a slope efficiency 0.156 W/A are obtained for the non-intermixed sample. These values are very close to the values provided by the wafer's vendor company suggesting that the active area is minimally perturbed. Figure 5-18 (b) also shows the characteristics of the intermixed area. From this figure threshold current and slope efficiency of 25 mA and 0.112 W/A are obtained, respectively. It is clear that this area exhibit more loss as expected, however this is not critical for our purposes which is the a slight change of the refractive index of the passive section by applying very small current. Figure 5-19 also show the optical spectra of the two lasers when biased with 80 mA of current and operating at 20 °C.

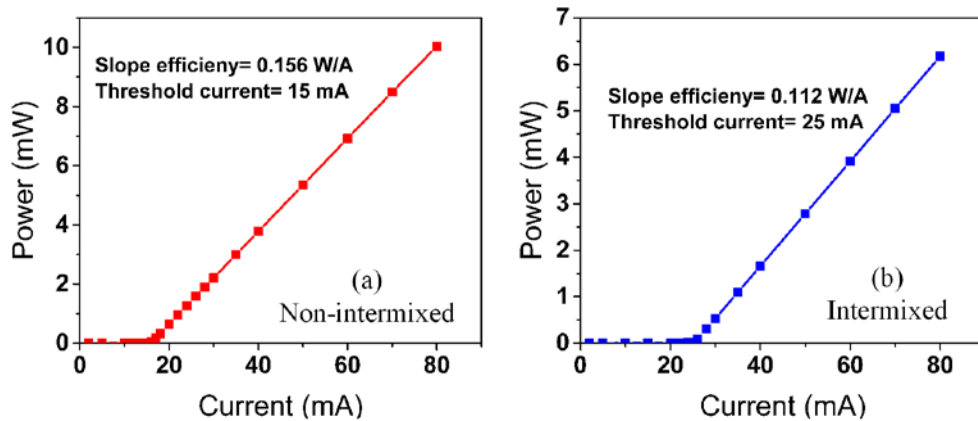


Figure 5-18. Typical current vs output power characteristics of the two 360 μm -long Fabry-Perot lasers, (a) device is cleaved from the area that intermixing inhibited and (b) is cleaved from the area that intermixing promoted.

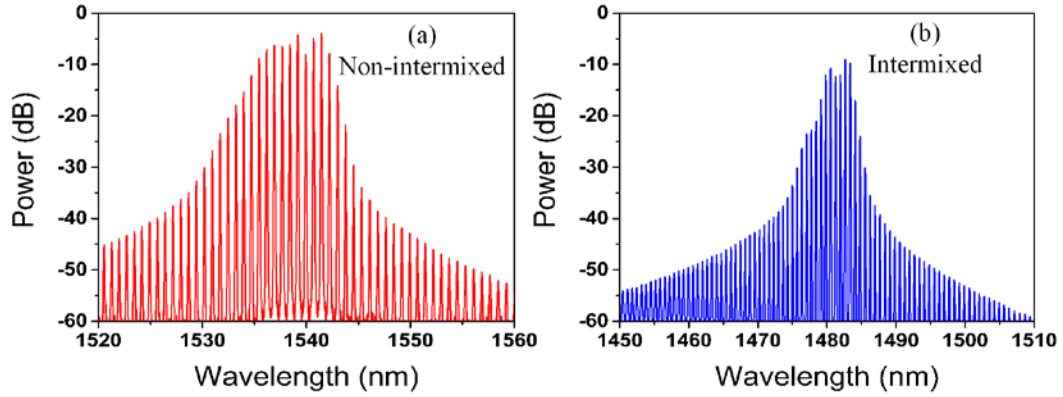


Figure 5-19. Optical spectra of the two different 360 μm -long Fabry-Perot lasers, (a) device is cleaved from the area that intermixing inhibited and (b) is cleaved from the area that intermixing promoted. (Both the laser are biased with 80 mA of current and operating at 20 $^{\circ}\text{C}$).

5.5. Device Characteristics

The three-section MLL cleaved with a total length of 1877 μm with a saturable absorber length of 30 μm and passive section length of 365 μm . The laser is mounted p-side up on the copper stud and its temperature is controlled using a TEC and a PID controller. Figure 5-20 shows the electrical and optical characteristics of the three-section MLL at operating temperature of 20 $^{\circ}\text{C}$ when no voltage is applied to the SA and passive sections. A threshold current of 44 mA, device impedance of 3.3 Ω and slope efficiency of 0.06 W/A is measured from these data.

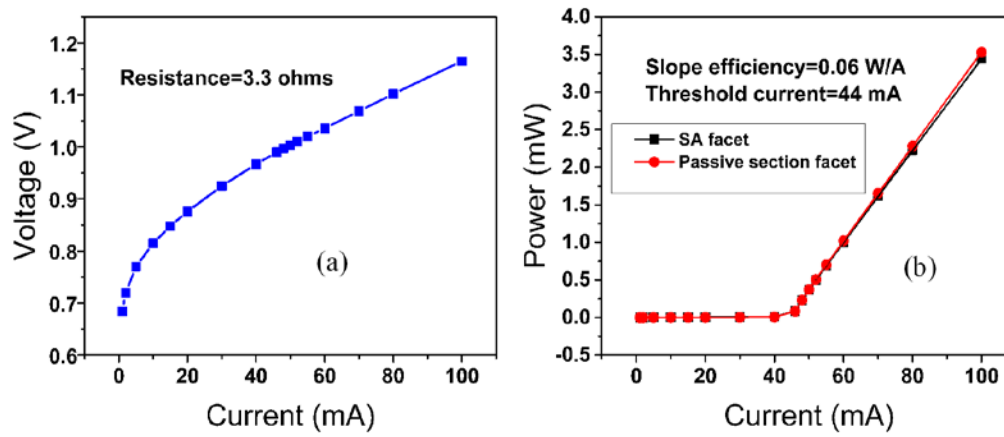


Figure 5-20. Typical voltage-current (left) and output power-current (right) characteristics of the MLL operating at 20 °C. No voltage is applied to the SA or passive section. The device characteristics are: $I_{\text{threshold}}=44$ mA, $R=3.3$ Ω and slope efficiency of 0.06 W/A.

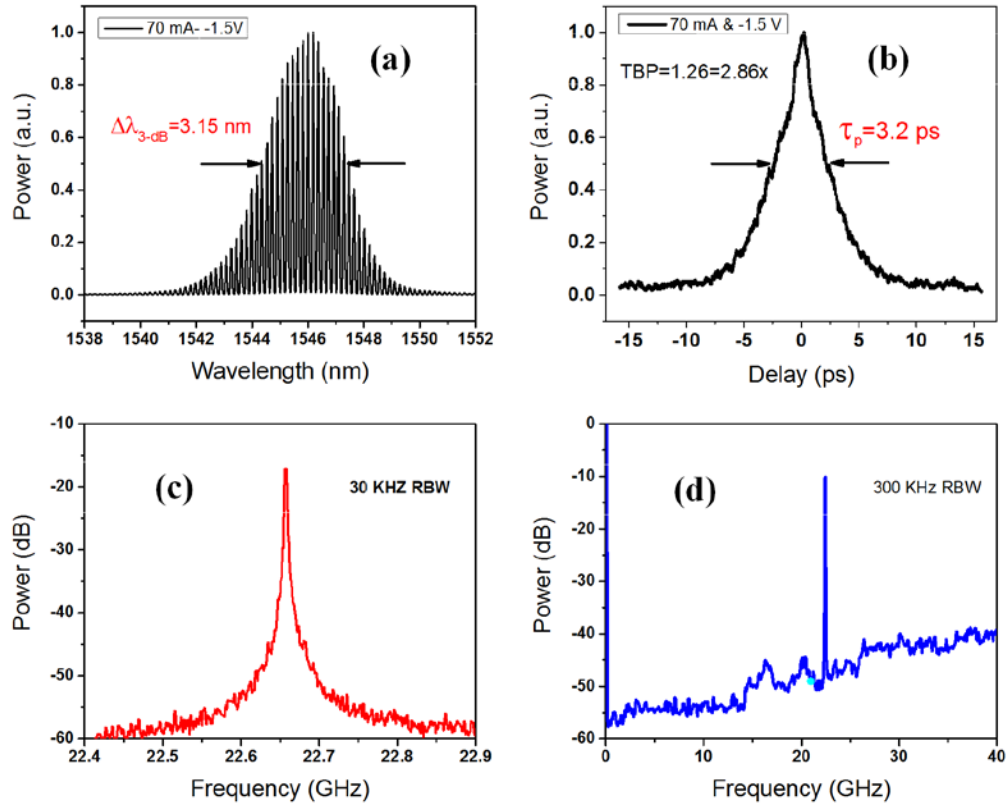


Figure 5-21. Optical spectrum of the three-section mode-locked laser with at $I_{\text{gain}} = 70 \text{ mA}$, $V_{\text{abs}} = -1.5 \text{ V}$, and unbiased passive section, (b) autocorrelation trace of an isolated pulse with deconvolved width of 3.2 ps (2.86 times transform-limited), (c) the corresponding RF spectrum, and (d) full span RF spectrum

Passive mode-locking has been achieved by forward biasing the gain section and reverse biasing the SA section using simple DC probes. Figure 5-21 (a) shows a stable mode-locking optical spectrum when the gain section is biased with 70 mA of current and SA section is reverse

biased with 1.5 V. An optical 3-dB bandwidth of 3.15 nm is achieved from this spectrum. An autocorrelation trace of an isolated pulse is shown in Figure 5-21 (b). From this graph a deconvolved pulse duration of 3.2 ps is calculated assuming a Gaussian shape for the optical spectrum. The pulses are chirped and 2.86 times transform-limit and they can be compressed to narrower pulse widths. The optical signal is photodetected using a 33 GHz PIN photodiode and Figure 5-21 (c) and (d) also show the radio frequency spectrum of the mode-locked laser.

A high resolution spectrum analyzer has been used to capture and analyze the absolute values of the frequency combs. Figure 5-22 shows the high resolution optical spectrum of three individual comb lines of the mode-locked laser when the gain section is biased with 70 mA of current and the SA is reverse biased with 1.5 V. The comb lines with the black color are when the passive section is not biased. As discussed in section 5.2, by applying a small current to the passive section one can induce a small change in the refractive index (2×10^{-4}) and subsequently a small change in the repetition rate of the mode-locked laser. This shifts the absolute frequency of each optical mode by the change in mode spacing times the comb line number. For the mode spacing in this MLL, the laser spectrum is centered on the 8542th comb line. Since the fixed point for repetition rate change is near DC for a passively MLL, only small changes are needed to achieve a greatly magnified ($\times 8542$) shift at optical frequencies. This is demonstrated with the comb lines in the red color in Figure 5-22. A 5.9 mA of current is needed to apply to the passive section to be able to shift the comb lines by half of the repetition rate of the laser (22.656 GHz).

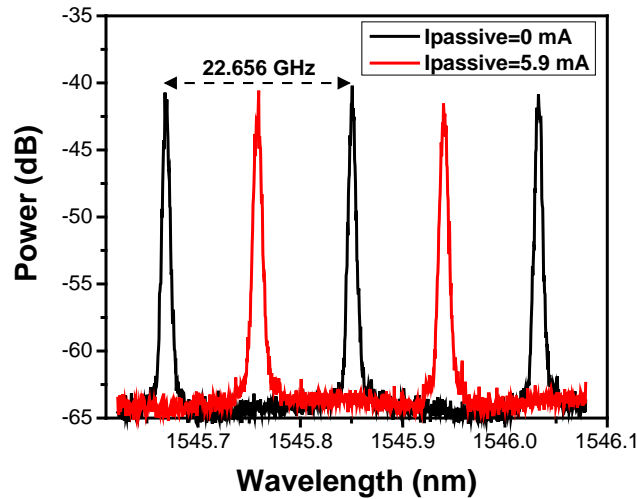


Figure 5-22. High resolution optical spectrum of the three optical modes. Black is when the passive section is unbiased and red is when the passive section is biased with 5.9 mA.

Modulating the comblines through the passive section has another advantage compared to modulating the gain section and that is the decoupling the AM and PM responses. Modulating the passive section basically should have the minimum amplitude modulation since the passive section is transparent at the operating wavelength of the mode-locked laser. Also very small amount of current is needed (only 1 mA of current is needed to shift the combs by 1.92 GHz) and these values are well below the threshold lasing values of the passive section. Figure 5-23 shows the optical output power change of the mode-locked laser as a function of passive section current. This is limited to only about 2% change for 10 mA of current applied to the passive section. This is basically the added ASE from the blueshifted bandgap energy of the passive section when it is forward biased.

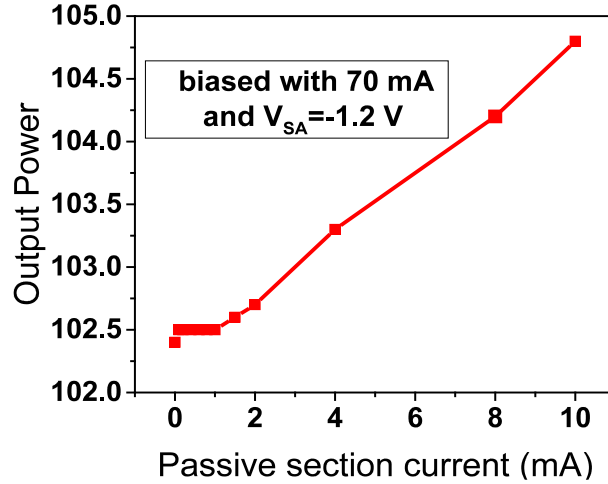


Figure 5-23. Output power change of the mode-locked laser as a function of passive section bias current

5.6. Experimental setup of the ultra linear intensity modulator

A schematic of the experimental setup is shown in Figure 5-24. Free space optical delays are used in both the arms of the MZI to be able to match the path lengths to achieve same pulse overlap after splitting. PZT linear optical stage is used in one of the optical delays to fine-tune the path difference and bias the MZI at quadrature. Power is monitored at three points of the setup: the injected power to the slave laser, the free space power in each of the arms of the interferometer, and the optical power coupled to the fiber from each of the arms. The last two power meters and a neutral density filter placed in front of the slave laser are used to monitor and balance the optical

power of each arms and help to increase the visibility of the MZI. With the help of half-wave plates, the polarization of each arm is adjusted to further increase the visibility.

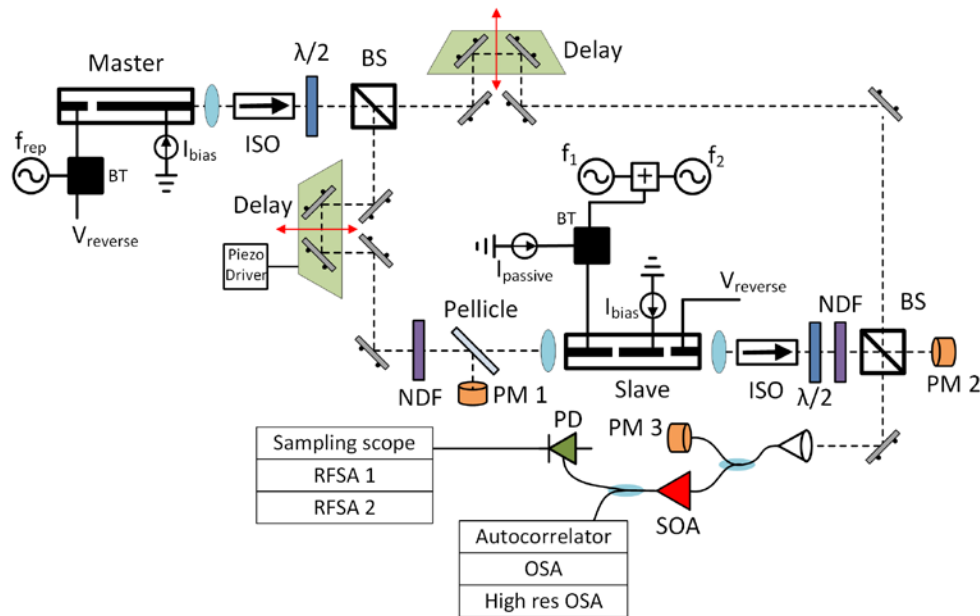


Figure 5-24. Experimental setup. ISO: Isolator; BS: Beam splitter; $\lambda/2$: Half-wave plate; NDF: Neutral density filter; BT: Bias-Tee; PM: Power meter; SOA: Semiconductor optical amplifier; PD: Photo-detector; RFA: Radio frequency amplifier; OSA: Optical spectrum analyzer; RFSA: Radio frequency spectrum analyzer

5.7. Experimental Results

Figure 5-25 shows the optical spectra of the master and slave laser before and after injection-locking. Here the master laser is a two-section device operating with 75 mA of bias current and a reverse bias voltage of 1.4 V and is maintained at a constant temperature of 17.35 °C. An RF power of 6 dBm at 22.712 GHz is applied to the SA to achieve hybrid mode-locking of the laser. The slave laser (three-section device) is passively mode-locked with 55 mA of bias current and a reverse bias voltage of 1.2 V and the operating temperature of 20 °C. SA voltages are carefully chosen to match the repetition rate frequencies and the operating temperature of the slave laser is carefully tuned for a precise overlap of its optical modes with that of the master laser. A high resolution optical spectrum analyzer is used to monitor the optical modes in more detail. Figure 5-26 (a) shows the corresponding RF spectra and confirms that the passively mode-locked slave laser follows the hybridly mode-locked master laser. The autocorrelation trace of the pulses from master and slave lasers are also shown in Figure 5-26 (b).

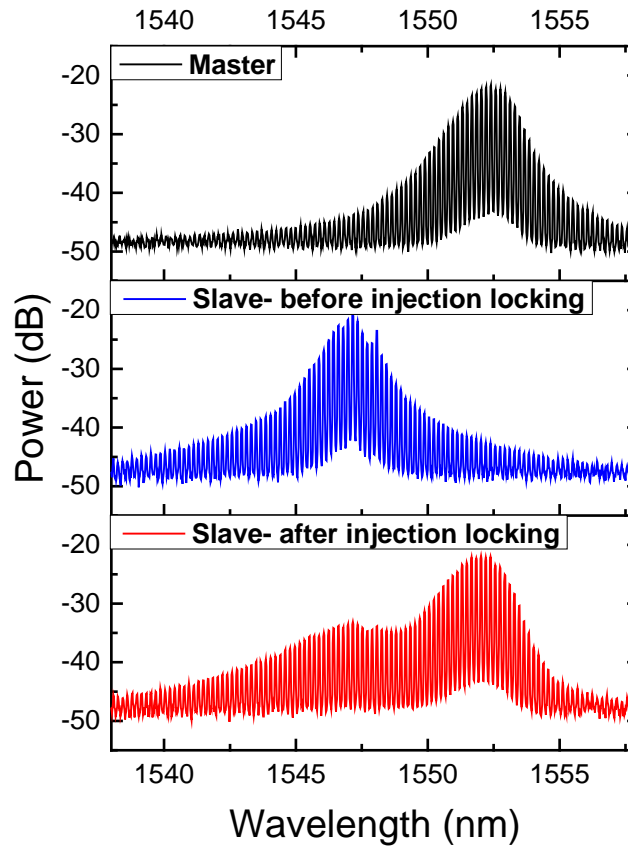


Figure 5-25. Optical spectrum of the two-section hybridly mode-locked master laser (black) with $I_{\text{gain}}=75$ mA, $V_{\text{SA}}=-1.4$ V, $T=17.35$ °C and 6 dBm of RF power at 22.712 GHz and optical spectra of the three-section passively mode-locked slave laser before (blue) and after (red) injection-locking with $I_{\text{gain}}=55$ mA, $V_{\text{SA}}=-1.2$ V, $T=20$ °C.

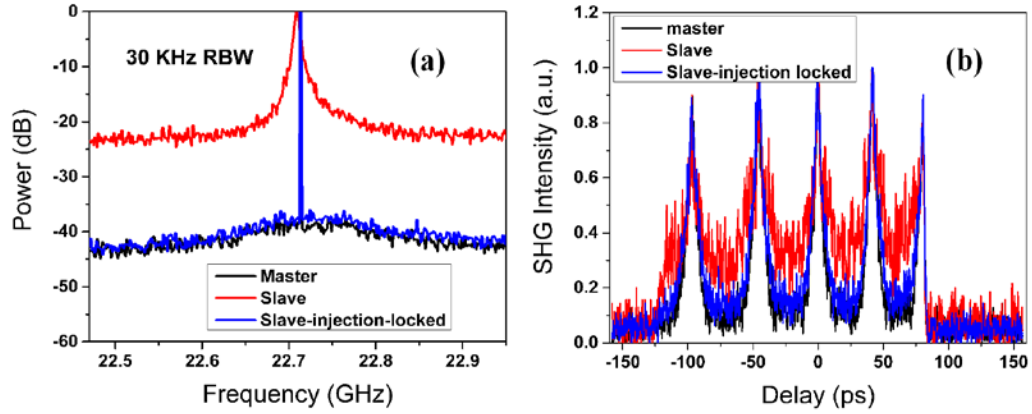


Figure 5-26. (a) Normalized radio frequency spectrum of the master laser (black) and also the slave laser before (red) and after injection-locking and (b) their corresponding autocorrelation traces. It is clear that the slave laser follows the master after injection-locking.

5.7.1. Two-tone intermodulation experiment

Two-tone intermodulation experiment results are presented in this section as a measure of the linearity of this modulator. In order to measure the signal to intermodulation ratio, the modulator is modulated through the passive section with two RF signals with the frequencies of 1000 MHz and 1100 MHz, simultaneously. As shown in Figure 5-24, the RF signals are combined using a 3-dB coupler and applied to the bias-tee of the passive section. The photo-detected RF signal of the modulated light is split into two and monitored with two radio frequency spectrum analyzers at the same time; one for fundamental frequencies with a larger frequency span and the other for third-order intermodulation tones at 900 MHz and 1200 MHz with a span of 200 Hz.

Figure 5-27 (a) shows the photo-detected RF power spectrum of the fundamental tones. The input powers to the modulator at the two frequencies are adjusted in such a way that the same fundamental powers are seen after photo-detection. Figure 5-27 (b) and (c) show the third-order intermodulation tones at 900 MHz and 1200 MHz, respectively. The 1200 MHz sideband is used for the calculations since it was the larger spur compared to the 900 MHz sideband. From this data, signal-to-intermodulation ratio of 63.1 dB is obtained when modulating the passive section.

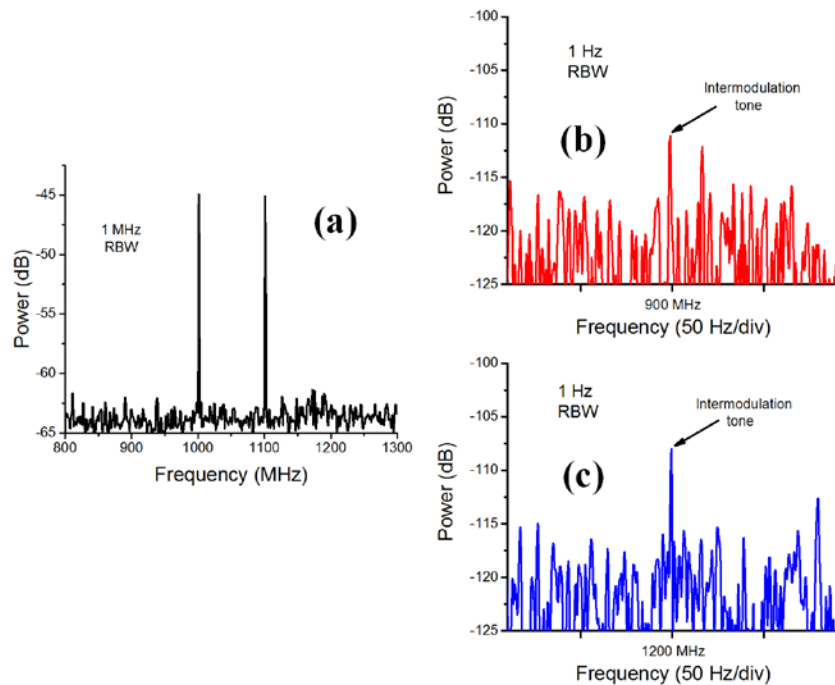


Figure 5-27. (a) Photo-detected RF power spectrum of fundamental frequencies (1 GHz and 1.1 GHz) (the input powers are adjusted to achieve the same fundamental powers), (b) detected RF power spectra of the third-order intermodulation tones at 900 MHz, (c) detected RF power spectra of the third-order intermodulation tones at 1200 MHz.

Figure 5-28 shows the fundamental and third-order intermodulation powers for different input RF powers. A linear fit of slope one and another linear fit of slope three are applied to the fundamental and intermodulation tones, respectively. Spur-free dynamic range of $75 \text{ dB.Hz}^{2/3}$ is obtained from modulating the passive section. Here the SFDR measurement is limited by noise from beating between the relatively broad linewidth laser modes.

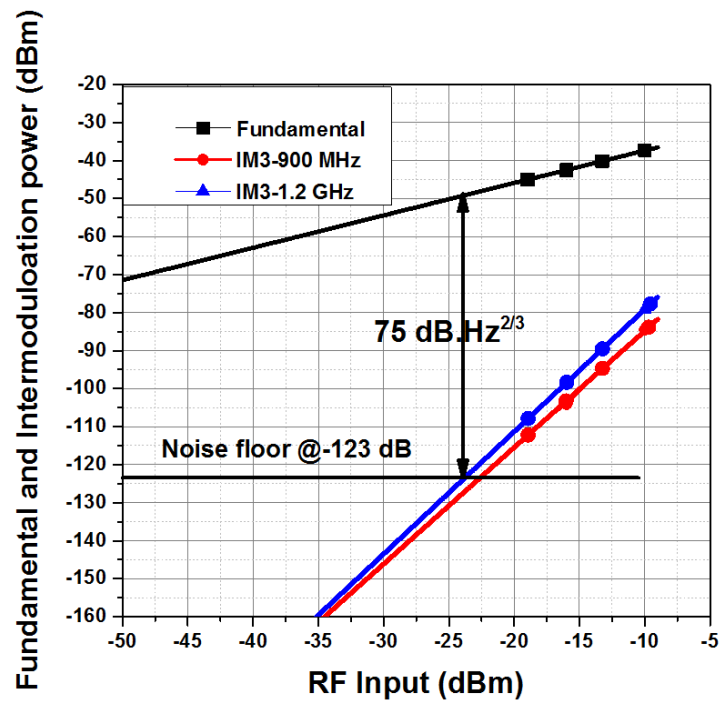


Figure 5-28. Fundamental and third-order intermodulation powers as a function of the input RF power to the modulator.

5.8. Conclusion

A novel highly linearized intensity modulator for pulsed light is presented in this chapter. This has been realized by introducing a three-section passively MLL injection-locked to a hybridly two-section MLL (which is the input to the MZI) into one of the arms of the MZI. By modulating the injection-locked laser, one can induce arcsine phase response on each of the injected longitudinal modes. A linear intensity modulator is obtained by interfering the modulated light with its unmodulated counterpart from the other arm in quadrature. By introducing the passive section into the previous laser design and modulating this section instead of gain section current or the voltage on the SA section, one can eliminate any unwanted amplitude modulation. This modulator has provided a six-fold reduction in the V_π and also 5 dB improvement of SFDR compared to the prior design for high performance and high resolution photonic ADC applications.

APPENDIX A: THERMAL ANNEALING PROFILES

Table 12. Thermal annealing recipe used for annealing contact at the temperature of 430 °C for
30 seconds

Step	Step Function	Time (Sec)	Temp °C	Gas 1 N ₂	Gas 1 N ₂
1	Idle	600	0	10	0
2	Idle	20	0	0	0
3	Ramp	8	430	0	3
4	Hold	30	430	0	3
5	Idle	15	0	0	3
6	Idle	600	0	10	0
7	Stop	0	0	0	0

Table 13. Thermal annealing recipe used for intermixing at the temperature of 800 °C for 30 seconds

Step	Step Function	Time (Sec)	Temp °C	Gas 1 N ₂	Gas 1 N ₂
1	Idle	1800	0	10	0
2	Idle	20	0	0	0
3	Ramp	15	800	0	3
4	Hold	30	800	0	3
5	Idle	15	0	0	3
6	Idle	1200	0	15	0
7	Stop	0	0	0	0

REFERENCES

1. Shoop, B.L., *Photonic Analog-to-Digital Conversion*. New York: Springer-Verlag, 2000.
2. Valley, G.C., *Photonic analog-to-digital converters*. Optics Express, 2007. **15**(5): p. 1955-1982.
3. Cox, C.H., *Analog Optical Links*. Cambridge UK, Cambridge University Press, 2004.
4. Juodawlkis, P.W., J.C. Twichell, G.E. Betts, J.J. Hargreaves, R.D. Younger, J.L. Wasserman, F.J. O'Donnell, K.G. Ray, and R.C. Williamson, *Optically sampled analog-to-digital converters*. Ieee Transactions on Microwave Theory and Techniques, 2001. **49**(10): p. 1840-1853.
5. Agrawal, G.P., *Fiber-Optic Communication Systems*. Wiley, New York, 1997: p. 336-343.
6. Taylor, H.F., M.J. Taylor, and P.W. Bauer, *Electro-Optic Analog-to-Digital Conversion Using Channel Waveguide Modulators*. Applied Physics Letters, 1978. **32**(9): p. 559-563.
7. Li, G.L. and P.K.L. Yu, *Optical intensity modulators for digital and analog applications*. Journal of Lightwave Technology, 2003. **21**(9): p. 2010-2030.
8. Sadhwani, R. and B. Jalali, *Adaptive CMOS predistortion linearizer for fiber-optic links*. Journal of Lightwave Technology, 2003. **21**(12): p. 3180-3193.
9. Myslinski, P., C. Szubert, A.P. Freundorfer, P. Shearing, J. Sitch, M. Davies, and J. Lee, *Over 20 GHz MMIC pre/postdistortion circuit for improved dynamic range broadband analog fiber optic link*. Microwave and Optical Technology Letters, 1999. **20**(2): p. 85-88.
10. W. Ng, D.P., D. Yap, S. Morton, C. Fields, and J. Jensen, *Ultra-high speed photonic analog-to-digital conversion techniques*. International Conference on Contemporary Photonics, Tokyo, Japan, 2002.

11. R. C. Williamson, R.D.Y., P. W. Juodawlkis, J. J. Hargreaves, and J. C. Twichell, *Precision calibration of an optically sampled analog-to-digital converter*. Digest of IEEE LEOS Summer Topical Meeting on Photonic Time/Frequency Measurement and Control, 2003: p. 22-23.
12. Rolland, C., G. Mak, K.L. Prosyk, C.M. Maritan, and N. Puetz, *High-Speed and Low-Loss, Bulk Electroabsorption Wave-Guide Modulators at 1.3 μ m*. Ieee Photonics Technology Letters, 1991. **3**(10): p. 894-896.
13. Miller, D.A.B., D.S. Chemla, T.C. Damen, A.C. Gossard, W. Wiegmann, T.H. Wood, and C.A. Burrus, *Band-Edge Electroabsorption in Quantum Well Structures - the Quantum-Confined Stark-Effect*. Physical Review Letters, 1984. **53**(22): p. 2173-2176.
14. Yariv, P.Y.a.A., *Photonics*. Oxford University Press, 2005.
15. Liu, B., J. Shim, Y.J. Chiu, A. Keating, J. Piprek, and J.E. Bowers, *Analog characterization of low-voltage MQW traveling-wave electroabsorption modulators*. Journal of Lightwave Technology, 2003. **21**(12): p. 3011-3019.
16. Chiu, Y.J., H.F. Chou, V. Kaman, P. Abraham, and J.E. Bowers, *High extinction ratio and saturation power traveling-wave electroabsorption modulator*. Ieee Photonics Technology Letters, 2002. **14**(6): p. 792-794.
17. Yariv, A., *Optical electronics*. Oxford University Press, 1996.
18. Noguchi, K., O. Mitomi, and H. Miyazawa, *Millimeter-wave Ti : LiNbO₃ optical modulators*. Journal of Lightwave Technology, 1998. **16**(4): p. 615-619.
19. Betts, G.E., L.M. Johnson, and C.H. Cox, *High-Sensitivity Lumped-Element Bandpass Modulators in Linbo₃*. Journal of Lightwave Technology, 1989. **7**(12): p. 2078-2083.

20. McKinney, J.D., K. Colladay, and K.J. Williams, *Linearization of Phase-Modulated Analog Optical Links Employing Interferometric Demodulation*. Journal of Lightwave Technology, 2009. **27**(9): p. 1212-1220.
21. Wilson, G.C., T.H. Wood, M. Gans, J.L. Zyskind, J.W. Sulhoff, J.E. Johnson, T. TanbunEk, and P.A. Morton, *Predistortion of electroabsorption modulators for analog CATV systems at 1.55 μ m*. Journal of Lightwave Technology, 1997. **15**(9): p. 1654-1662.
22. Laliew, C., S.W. Lovseth, X.B. Zhang, and A. Gopinath, *A linearized optical directional-coupler modulator at 1.3 μ m*. Journal of Lightwave Technology, 2000. **18**(9): p. 1244-1249.
23. Sabido, D.J.M., M. Tabara, T.K. Fong, C.L. Lu, and L.G. Kazovsky, *Improving the Dynamic-Range of a Coherent Am Analog Optical Link Using a Cascaded Linearized Modulator*. Ieee Photonics Technology Letters, 1995. **7**(7): p. 813-815.
24. Nazarathy, M., J. Berger, A.J. Ley, I.M. Levi, and Y. Kagan, *Progress in Externally Modulated Am Catv Transmission-Systems*. Journal of Lightwave Technology, 1993. **11**(1): p. 82-105.
25. Brooks, J.L., G.S. Maurer, and R.A. Becker, *Implementation and Evaluation of a Dual Parallel Linearization System for Am Scm Video Transmission*. Journal of Lightwave Technology, 1993. **11**(1): p. 34-41.
26. Huygens, C., *Horologium oscillatorium sive de motu pendularium*. 1675.
27. Steier, W.H. and H.L. Stover, *Locking of Laser Oscillators by Light Injection*. Ieee Journal of Quantum Electronics, 1966. **Qe 2**(4): p. R23-&.
28. Adler, R., *Study of Locking Phenomena in Oscillators*. Proceedings of the Ieee, 1973. **61**(10): p. 1380-1385.

29. Kobayashi, S. and T. Kimura, *Injection Locking Characteristics of an Algaas Semiconductor-Laser*. Ieee Journal of Quantum Electronics, 1980. **16**(9): p. 915-917.
30. Siegman, A.E., *Lasers*. 1986: p. 1129-1170.
31. Hoghooghi, N., *Injection-locked semiconductor laser for realization of novel RF Photonics Components*. University of Central Florida, Orlando, FL, 2012.
32. Hoghooghi, N. and P.J. Delfyett, *Theoretical and Experimental Study of a Semiconductor Resonant Cavity Linear Interferometric Intensity Modulator*. Journal of Lightwave Technology, 2011. **29**(22): p. 3421-3427.
33. Kobayashi, S. and T. Kimura, *Optical-Phase Modulation in an Injection Locked Algaas Semiconductor-Laser*. Ieee Journal of Quantum Electronics, 1982. **18**(10): p. 1662-1669.
34. Hoghooghi, N., I. Ozdur, M. Akbulut, J. Davila-Rodriguez, and P.J. Delfyett, *Resonant cavity linear interferometric intensity modulator*. Optics Letters, 2010. **35**(8): p. 1218-1220.
35. Karin, J.R., R.J. Helkey, D.J. Derickson, R. Nagarajan, D.S. Allin, J.E. Bowers, and R.L. Thornton, *Ultrafast Dynamics in Field-Enhanced Saturable Absorbers*. Applied Physics Letters, 1994. **64**(6): p. 676-678.
36. *BeamPROPTM*, RSoft Design Group, Inc.
37. Hasegawa, O.W.a.H., *InP-Based Materials and Devices," Wiley Series in Microwave and Optical Engineering*. John Wiley and Sons Inc., 1999.
38. Hjort, K., *Sacrificial etching of III-V compounds for micromechanical devices*. Journal of Micromechanics and Microengineering, 1996. **6**(4): p. 370-375.

39. Coldren, L.A., K. Furuya, and B.I. Miller, *On the Formation of Planar-Etched Facets in Gainasp Inp Double Heterostructures*. Journal of the Electrochemical Society, 1983. **130**(9): p. 1918-1926.
40. *LEditTM*, Tanner Research Inc.
41. Elias, P., I. Kostic, J. Soltys, and S. Hasenohrl, *Wet-etch bulk micromachining of (100) InP substrates*. Journal of Micromechanics and Microengineering, 2004. **14**(8): p. 1205-1214.
42. Madou, M.J., *Fundamentals of Microfabrication: The Science of Miniaturization*. CRC Press, Second Edition, 2002.
43. Williams, R., *Modern GaAs Processing methods*. Artech House, 1990.
44. NELSON, R.J., P.D. Wright, P.A. Barnes, R.L. Brown, T. Cella, and R.G. Sobers, *High-outputpower InGaAsP (1.3 mm) Stripe-buried Heterostructure Lasers*. Appl. Phys. Lett., 1980. **36**(5): p. 358-360.
45. NG, W., C.S. Hong, H. Mansevit, and P.D. Dapkus, *Low Threshold 1.3 mm GaInAsP/InP Heterostructure Lasers by LPE and MOCVD*. Appl. Phys. Lett., 1981. **39**(3): p. 188-189.
46. Adachi, S. and H. Kawaguchi, *Chemical Etching Characteristics of (001)Inp*. Journal of the Electrochemical Society, 1981. **128**(6): p. 1342-1349.
47. Ikossianastasiou, K., S.C. Binari, G. Kelner, J.B. Boos, C.S. Kyono, J. Mittereder, and G.L. Griffin, *Wet Chemical Etching with Lactic-Acid Solutions for Inp-Based Semiconductor-Devices*. Journal of the Electrochemical Society, 1995. **142**(10): p. 3558-3564.
48. Dambkes, H., U. Konig, and B. Schwaderer, *Ingaas/Inp Heterobipolar Transistors for Integration on Semi-Insulating Inp Substrates*. Electronics Letters, 1984. **20**(23): p. 955-957.

49. Dupuis, R.D., D.G. Deppe, C.J. Pinzone, N.D. Gerrard, S. Singh, G.J. Zydzik, J.P. Vanderziel, and C.A. Green, *In_{0.47}Ga_{0.53}As-Inp Heterostructures for Vertical Cavity Surface Emitting Lasers at 1.65 μ m Wavelength*. Journal of Crystal Growth, 1991. **107**(1-4): p. 790-795.
50. Bhushan, A.S., F. Coppinger, and B. Jalali, *Time-stretched analogue-to-digital conversion*. Electronics Letters, 1998. **34**(11): p. 1081-1083.
51. Chou, J., Y. Han, and B. Jalali, *Adaptive RF-photonic arbitrary waveform generator*. Ieice Transactions on Electronics, 2003. **E86c**(7): p. 1226-1229.
52. Delfyett, P.J., I. Ozdur, N. Hoghooghi, M. Akbulut, J. Davila-Rodriguez, and S. Bhooplapur, *Advanced Ultrafast Technologies Based on Optical Frequency Combs*. Ieee Journal of Selected Topics in Quantum Electronics, 2012. **18**(1): p. 258-274.
53. Ji, C., N. Chubun, R.G. Broeke, J. Cao, Y. Du, P. Bjeletich, and S.J.B. Yoo, *Electrical subharmonic hybrid mode locking of a colliding pulse mode-locked laser at 28 GHz*. Ieee Photonics Technology Letters, 2005. **17**(7): p. 1381-1383.
54. Lee, H.K., V. Loyo-Maldonado, B.C. Qiu, K.L. Lee, C. Shu, S. Pinches, I.G. Thayne, A.C. Bryce, and J.H. Marsh, *Efficient direct locking of colliding pulse mode-locked lasers on semi-insulating substrate at 1.5 μ m*. Ieee Photonics Technology Letters, 2002. **14**(8): p. 1049-1051.
55. Kurita, H., T. Shimizu, and H. Yokoyama, *Experimental investigations of harmonic synchronization conditions and mechanisms of mode-locked laser diodes induced by optical-pulse injection*. Ieee Journal of Selected Topics in Quantum Electronics, 1996. **2**(3): p. 508-513.
56. Hou, L.P., P. Stolarz, J. Javaloyes, R.P. Green, C.N. Ironside, M. Sorel, and A.C. Bryce, *Subpicosecond Pulse Generation at Quasi-40-GHz Using a Passively Mode-Locked*

- AlGaInAs-InP 1.55- μ m Strained Quantum-Well Laser*. Ieee Photonics Technology Letters, 2009. **21**(23): p. 1731-1733.
57. Sarailou, E., A. Ardey, and P.J. Delfyett, *Low Noise Ultrashort Pulse Generation by Direct RF Modulation at 22 GHz from an AlGaInAs Multiple Quantum-Well Laser at 1.55 μ m*. Ieee Photonics Technology Letters, 2012. **24**(17): p. 1561-1563.
 58. N. Hoghooghi, J. Davila-Rodriguez, S. Bhooaplapur, and P.J. Delfyett. *120 dB. $\text{Hz}^{2/3}$ spur free dynamic range from a resonant cavity interferometric linear intensity modulator,*” . in *Conf. Lasers Electro-Opt., San Jose, CA, USA*. May 2012.
 59. E. Sarailou, A.A., N. Hoghooghi, and P. Delfyett, *Towards linear interferometric intensity modulator for photonic ADCs using an injection locked AlInGaAs quantum well Fabry–Perot laser*. in *Proc. Conf. Lasers Electro-Opt.*, May 2012(1-2).
 60. Sarailou, E., A. Ardey, and P.J. Delfyett, *A Linearized Intensity Modulator for Photonic Analog-to-Digital Conversion Using an Injection-Locked Mode-Locked Laser*. Journal of Lightwave Technology, 2014. **32**(21): p. 4042-4047.
 61. Mogensen, F., H. Olesen, and G. Jacobsen, *Locking Conditions and Stability Properties for a Semiconductor-Laser with External Light Injection*. Ieee Journal of Quantum Electronics, 1985. **21**(7): p. 784-793.
 62. Chen, Y.K., M.C. Wu, T. Tanbunek, R.A. Logan, and M.A. Chin, *Subpicosecond Monolithic Colliding-Pulse Mode-Locked Multiple Quantum-Well Lasers*. Applied Physics Letters, 1991. **58**(12): p. 1253-1255.
 63. Ardey, A., J. Kim, E. Sarailou, and P.J. Delfyett, *Optical and RF stability transfer in a monolithic coupled-cavity colliding pulse mode-locked quantum dot laser*. Optics Letters, 2012. **37**(17): p. 3480-3482.

64. E. Sarailou and P. Delfyett, *Towards Highly Linear Intensity Modulator for High Resolution Photonic ADCs Using a Three-Section Mode-Locked Laser*. CLEO: Science and Innovations, May 2015.
65. Kaoru Yamanouchi, K.M., *Progress in Ultrafast Intense Laser Science, Volume 9*. Springer Series in Chemical Physics, 2013.
66. Paschotta, R., A. Schlatter, S.C. Zeller, H.R. Telle, and U. Keller, *Optical phase noise and carrier-envelope offset noise of mode-locked lasers*. Applied Physics B-Lasers and Optics, 2006. **82**(2): p. 265-273.
67. Telle, H.R., G. Steinmeyer, A.E. Dunlop, J. Stenger, D.H. Sutter, and U. Keller, *Carrier-envelope offset phase control: A novel concept for absolute optical frequency measurement and ultrashort pulse generation*. Applied Physics B-Lasers and Optics, 1999. **69**(4): p. 327-332.
68. Talneau, A., D. Rondi, M. Krakowski, and R. Blondeau, *Very Low Threshold Operation of 1.52-Mu-M Galnasp/Inp Dfb Buried Ridge Structure Laser-Diodes Entirely Grown by Mocvd*. Electronics Letters, 1988. **24**(10): p. 609-611.
69. Williams, P.J., P.M. Charles, I. Griffith, L. Considine, and A.C. Carter, *High-Performance Buried Ridge Dfb Lasers Monolithically Integrated with Butt Coupled Strip Loaded Passive Wave-Guides for Oeic*. Electronics Letters, 1990. **26**(2): p. 142-143.
70. Verschuren, C.A., P.J. Harmsma, Y.S. Oei, M.R. Leys, H. Vonk, and J.H. Wolter, *Butt-coupling loss of 0.1dB/interface in InP/InGaAs multiple-quantum-well waveguide-waveguide structures grown by selective area chemical beam epitaxy*. Semiconductor Science and Technology, 1998. **13**(8A): p. A169-A172.
71. Gibbon, M., J.P. Stagg, C.G. Cureton, E.J. Thrush, C.J. Jones, R.E. Mallard, R.E. Pritchard, N. Collis, and A. Chew, *Selective-Area Low-Pressure Mocvd of Gainasp and Related*

- Materials on Planar Inp Substrates*. Semiconductor Science and Technology, 1993. **8**(6): p. 998-1010.
72. Coleman, J.J., R.M. Lammert, M.L. Osowski, and A.M. Jones, *Progress in InGaAs-GaAs selective-area MOCVD toward photonic integrated circuits*. Ieee Journal of Selected Topics in Quantum Electronics, 1997. **3**(3): p. 874-884.
 73. Marsh, J.H., *Quantum-Well Intermixing*. Semiconductor Science and Technology, 1993. **8**(6): p. 1136-1155.
 74. Li, H., *Semiconductor Quantum Wells Intermixing*. Gordon and Breach Science Publishers, 2000.
 75. Laidig, W.D., N. Holonyak, M.D. Camras, K. Hess, J.J. Coleman, P.D. Dapkus, and J. Bardeen, *Disorder of an Alas-Gaas Super-Lattice by Impurity Diffusion*. Applied Physics Letters, 1981. **38**(10): p. 776-778.
 76. Pape, I.J., P.L.K. Wa, J.P.R. David, P.A. Claxton, and P.N. Robson, *Diffusion-Induced Disorder of Ga_{0.47}In_{0.53}as/Inp Multiple Quantum Wells with Zinc*. Electronics Letters, 1988. **24**(15): p. 910-911.
 77. Mclean, C.J., J.H. Marsh, R.M. Delarue, A.C. Bryce, B. Garrett, and R.W. Glew, *Layer Selective Disorder by Photoabsorption-Induced Thermal-Diffusion in Ingaas/Inp Based Multiquantum Well Structures*. Electronics Letters, 1992. **28**(12): p. 1117-1119.
 78. Sudoh, T.K., M. Kumano, Y. Nakano, and K. Tada, *Wavelength trimming by photoabsorption-induced disordering for multiple-wavelength distributed-feedback laser arrays*. Ieee Photonics Technology Letters, 1997. **9**(7): p. 887-888.
 79. Aimez, V., J. Beauvais, J. Beerens, D. Morris, H.S. Lim, and B.S. Ooi, *Low-energy ion-implantation-induced quantum-well intermixing*. Ieee Journal of Selected Topics in Quantum Electronics, 2002. **8**(4): p. 870-879.

80. Du, S.C., L. Fu, H.H. Tan, and C. Jagadish, *Investigation of ion implantation induced intermixing in InP based quaternary quantum wells*. Journal of Physics D-Applied Physics, 2011. **44**(47).
81. Djie, H.S. and T. Mei, *Plasma-induced quantum well intermixing for monolithic photonic integration*. Ieee Journal of Selected Topics in Quantum Electronics, 2005. **11**(2): p. 373-382.
82. Helmy, A.S., N.P. Johnson, M.L. Ke, A.C. Bryce, J.S. Aitchison, J.H. Marsh, I. Gontijo, G.S. Buller, J. Davidson, and P. Dawson, *A study of impurity-free vacancy disordering in GaAs-AlGaAs for improved modeling*. Ieee Journal of Selected Topics in Quantum Electronics, 1998. **4**(4): p. 661-668.
83. Sudo, S., H. Onishi, Y. Nakano, Y. Shimogaki, K. Tada, M.J. Mondry, and L.A. Coldren, *Impurity-free disordering of InGaAs/InGaAlAs quantum wells on InP by dielectric thin cap films and characterization of its in-plane spatial resolution*. Japanese Journal of Applied Physics Part 1-Regular Papers Short Notes & Review Papers, 1996. **35**(2B): p. 1276-1279.
84. Yu, J.S. and K.S. Chung, *Effect of the property of dielectric capping layers on impurity-free vacancy diffusion in InGaAs/InGaAsP MQW structures*. Semiconductor Science and Technology, 2007. **22**(8): p. 919-924.
85. Beauvais, J., J.H. Marsh, A.H. Kean, A.C. Bryce, and C. Button, *Suppression of Bandgap Shifts in GaAs/AlGaAs Quantum-Wells Using Strontium Fluoride Caps*. Electronics Letters, 1992. **28**(17): p. 1670-1672.
86. Fu, L., P. Lever, H.H. Tan, C. Jagadish, P. Reece, and M. Gal, *Suppression of interdiffusion in InGaAs/GaAs quantum dots using dielectric layer of titanium dioxide*. Applied Physics Letters, 2003. **82**(16): p. 2613-2615.

87. Kowalski, O.P., C.J. Hamilton, S.D. McDougall, J.H. Marsh, A.C. Bryce, R.M. De la Rue, B. Vogelee, C.R. Stanley, C.C. Button, and J.S. Roberts, *A universal damage induced technique for quantum well intermixing*. Applied Physics Letters, 1998. **72**(5): p. 581-583.
88. McDougall, S.D., O.P. Kowalski, C.J. Hamilton, F. Camacho, B.C. Qiu, M.L. Ke, R.M. De La Rue, A.C. Bryce, and J.H. Marsh, *Monolithic integration via a universal damage enhanced quantum-well intermixing technique*. Ieee Journal of Selected Topics in Quantum Electronics, 1998. **4**(4): p. 636-646.
89. Lee, K.H., B. Roycroft, J. O'Callaghan, C.L.L.M. Daunt, H. Yang, J.H. Song, F.H. Peters, and B. Corbett, *Integration of AlInGaAs-MQW Fabry-Perot Lasers With Emission at Two Wavelength Ranges via Quantum-Well Intermixing*. Ieee Photonics Technology Letters, 2011. **23**(1): p. 27-29.
90. Lee, K.H., K. Thomas, A. Gocalinska, M. Manganaro, E. Pelucchi, F.H. Peters, and B. Corbett, *SiNx-induced intermixing in AlInGaAs/InP quantum well through interdiffusion of group III atoms*. Journal of Applied Physics, 2012. **112**(9).
91. Adams, A.C., F.B. Alexander, C.D. Capio, and T.E. Smith, *Characterization of Plasma-Deposited Silicon Dioxide*. Journal of the Electrochemical Society, 1981. **128**(7): p. 1545-1551.
92. Chen, K.S., J.Y. Chen, and S.Y. Lin, *Fracture analysis of thick plasma-enhanced chemical vapor deposited oxide films for improving the structural integrity of power MEMS*. Journal of Micromechanics and Microengineering, 2002. **12**(5): p. 714-722.
93. K. D. Mackenzie, D. J. Johnson, M. W. DeVre, a. R. J. Westerman, and B.H. Reelfs, *Stress control of Si-Based PECVD dielectrics*. Electrochemical Society Meeting, Quebec City Canada, May 2005.